

UNIVERSITÀ DEGLI STUDI DI MILANO
Facoltà di Scienze Matematiche, Fisiche e Naturali
Corso di Laurea in Fisica

Performance study of the ATLAS electromagnetic End-Cap calorimeter

RELATORE: Prof. Luciano Mandelli
CORRELATORE: Dott. Daniele Pedrini
RELATORE ESTERNO: Prof. Bertrand Laforge

Tesi di Laurea di
Pietro G. Cavalleri
Matr. 618146
Codice PACS 29.90.

ANNO ACCADEMICO 2004-2005

Contents

Ringraziamenti	v
Introduction	vii
1 The Standard Model	1
1.1 The elements of the Standard Model	2
1.2 The Quantum Electro-Dynamics	3
1.3 The weak interactions	4
1.3.1 CKM matrix	8
1.4 The Strong Interactions (QCD)	9
1.5 Successes and failures of the SM and future scenarios	9
2 The ATLAS experiment at LHC	11
2.1 Proton-Proton interaction and Higgs boson production.	12
2.2 The ATLAS detector	15
2.2.1 Inner Detector	16
2.2.2 The central solenoid.	18
2.2.3 Calorimeters.	18
2.2.4 Muon spectrometer.	25
2.2.5 Data acquisition and trigger system.	27
2.3 The electromagnetic End Cap calorimeter (EMEC)	28
2.3.1 Absorbers and electrodes	30
2.3.2 Energy measurement.	31
2.3.3 Granularity	33
2.4 Test Beam	33
2.4.1 Test Beam Setup	33
2.4.2 Trigger System	35
2.4.3 Read Out Electronics	36
2.4.4 Electronic calibration	37

3	HV-Energy curve and Signal Shape	39
3.1	HV-Energy Curve	39
3.1.1	Determination of the electron energy peak	39
3.1.2	Cleaning of the beam	41
3.1.3	Fitting the HV-Energy curve	44
3.2	Signal shapes	47
4	Noise	51
4.1	Noise measurement	51
4.2	Search for a low frequency noise.	54
4.3	Correlation between EMEC cells.	55
4.4	Comparison between Test Beam 2004 and other Tests Beam.	58
5	HV corrections	61
5.1	Energy- η corrections	61
5.1.1	Results of Scans Performed	64
5.1.2	First corrections	65
5.1.3	Cluster level correction	76
5.2	Summary and conclusions for Energy- η response.	81
6	Spatial Resolution	83
6.1	Global ϕ -resolution	84
6.1.1	Global ϕ -resolution Vs. η	85
6.1.2	Global ϕ -resolution Vs. Beam Energy	87
6.1.3	Intrinsic BPC resolution	89
6.1.4	Multiple Scattering contribution	90
6.2	Global η -resolution	91
6.2.1	η -resolution vs η	93
6.2.2	η -resolution at different energies	94
6.3	Summary and conclusions for spatial resolution.	95
A	Two methods for the signal reconstruction.	99
A.1	Parabola Method	99
A.2	Optimal Filtering	100
B	Riassunto	103
B.1	Il Modello Standard	103
B.2	L'esperimento ATLAS all'LHC	105
B.2.1	Il rivelatore ATLAS	105
B.2.2	Calorimetro Elettromagnetico	106
B.3	Test Beam	109

B.3.1	Elettronica di lettura e calibrazione	109
B.4	Curva HV-Energia e forma del segnale	110
B.4.1	Fit della curva HV-Energia	111
B.4.2	Forma del Segnale	111
B.5	Rumore	112
B.6	Correzioni di Alta Tensione	113
B.6.1	Correzioni a livello di celle	114
B.6.2	Calcolo di α e β	115
B.6.3	Correzioni a livello di cluster	115
B.7	Risoluzione Spaziale	116
B.7.1	Risoluzione in ϕ	116
B.7.2	Risoluzione intrinseca delle BPC e contributi di Multiple Scattering.	117
B.7.3	Risoluzione in η	118

Ringraziamenti

Trovare le parole giuste per ringraziare tutte le persone che hanno contribuito direttamente o indirettamente allo sviluppo di questa tesi non è per niente facile. La fine della redazione di una tesi rappresenta anche la fine di un periodo della propria vita.

Per prima cosa vorrei ringraziare il prof. Mandelli, per avermi concesso l'opportunità di svolgere una tesi su un esperimento affascinante come ATLAS, e i dott. Fanti e Tartarelli: l'entusiasmo che ho trovato in loro è stato un fattore determinante nella scelta dell'esperimento.

In seguito sono grato al dott. Daniele Pedrini per l'appoggio e il sostegno all'idea di svolgere questa tesi all'estero.

Cette thèse a été entièrement réalisée au le Laboratoire de Physique Nucleaire et des Haute Énergies (LPNHE) de Paris. À ce titre je voudrais remercier tous le membres du groupe ATLAS de ce Laboratoire, pour m'avoir accueilli, pour la patience qu'ils ont eue quand je ne comprenais rien à ce qu'ils m'expliquaient et pour toutes les question *à la con* que j'ai posées. Ce travail a été possible grâce à Bertrand Laforge et surtout grâce à Philippe Schwemling, qui m'a fait mûrir comme physicien ansi qu'en tant qu'homme, en corrigeant toutes mes fautes et mes erreurs, en me donnant beaucoup d'enthousiasme et en me jetant dans la bagarre.

Un grand merci à tous les thésards du LPNHE (Guillaume, Delphine, Bruno, Sébastien, Claire, Rui, Julie, Stephan, Florent...), à Diego, Luz et Emmanuel Hornero pour leur l'aide avec l'informatique, à Emmanuel Busato pour ne pas m'avoir cassé la tête quand je lui posait les questions le plus bêtes, à Stefania pour les trois mois passés à ses côtés dans le bureau, à Marc pour l'énergie et l'envie de vivre qu'il te donne et à Gian Piero pour son aide dans les corrections et son amitié.

L'année que j'ai passée à Paris a aussi été formidable grâce à des gens qui n'ont rien à voir avec la physique.

Tout d'abord mes colocataires: quelqu'un avec qui je n'ai vécu que deux mois, et d'autre avec qui j'ai vécu plus longtemps: Ivan de Vinaros, Laura de Valencia, Elsa de Gotemborg, Marta de Barcelona et, *last but not least*, Kévin

de Metz et le *Picon power*. Ils ont toléré mon désordre et mes conneries, ils m'ont été toujours proches surtout dans les moments de tristesse.

Viennent ensuite Marcello (il sait pourquoi) et ceux qui, pour quelques mois, ont formé ma famille parisienne: les trois *chicas catalanas*, Aina *Femme Fatale*, Nuria *morbidissima* et Marta (avec la *montre volée à Caravaggio*), Carlos de Malaga (et sa vie dans la cinquième dimension) et Daniela de Bergamo.

Enfin, merci à Kurro (et sa *peña madridista*) et Andres, pour toutes les soirées passées ensemble et l'énergie qu'ils m'ont toujours transmise.

Et je ne peux pas oublier *la ville lumière*, ses endroits magiques et ses contradictions... Notre Dame, les Jardins du Luxembourg, la Tour Eiffel, le 132 Rue d'Assas, le Pantheon, le 9 Rue Boussingault, Saint Étienne du Monde et les keufs, les soirées surrealistes chez moi, le 210 Rue Fbg. St. Martin et ses toilettes, le Louvre, le métro de la station de Palais Royal, la tour 33, Port Royal, le café Danton (crash...), les variables à placer, le quai de Jussieu (CRASH!!!...), Gibert Jeune, le Pantalon, le sandwich grec, le Pont des Arts, le plombier polonais, le 29 Mai, le Père Lachaise, le hockey, le Martini rouge au Sénat, la brasserie des Deux Ponts (les souvenirs ne sont pas toujours beaux), l'Amour de Jeux, le 14 Juillet, la République, *the Clash of Civilisation*, la racaille, le Nord Transmet le Message, le bruit et l'odeur...

L'anno parigino non mi ha fatto dimenticare gli amici italiani, anzi, la lontananza ha reso ancora piú forti certi legami.

I compagni della facoltà di fisica, con cui ho condiviso momenti e anche viaggi indimenticabili, e che troppe volte m'hanno salvato alla vigilia degli esami: Fabio, Manuel, Tome, Telespalla, il Geometra, Michele, Federica, Pietro, Simone, Marco, Ivan, Luca, lo Slavo, Claudia, Giulia e tanti altri...

E ovviamente gli amici di Bergamo, quelli che, nonostante tutto, ci sono: AnnaMarilySissiDeleCortiAleFeffePezzoGottiNellaMasseIodyZenValerio.

Ovviamente un pensiero a mio zio Ermanno (e il gioco della morra) e alla sua famiglia. Un grazie di cuore a mia nonna, per l'aiuto e il sostegno costante (dai che ce l'ho fatta...).

Infine alla mia famiglia, a Giacomo e Marta e ai miei genitori. Questo lavoro lo devo a loro.

Introduction

This Diploma Thesis has been developed inside the ATLAS group of the Laboratory of High Energy Physics of Paris (LPNHE). The ATLAS detector will begin its data taking in 2007 in the Large Hadron Collider of the CERN, in Geneva; it has been built mainly for the search of the Higgs boson (the only particle of the Standard Model not yet observed) and new physics, like the search of Super Symmetric particles, but also for very precise measures on the Standard Model physics (quark top physics, CP violation...).

ATLAS is a multi-scope detector that has a cylindrical symmetry with the axis parallel to the beam pipe. From the axis of symmetry moving in the radial direction we find the inner detector, the central solenoid, the calorimeters and the muon spectrometer.

The analysis of the performances of the End-Cap inner wheel, located close to the beam axis, of the ATLAS electromagnetic calorimeter is the main goal of this thesis. Test Beam data of 2004 from electron beams have been used.

Before getting to the study of its performances in energy and position reconstruction, we will develop some preliminary analysis. The first concerns the High Voltage versus Energy curve, that is, how energy changes varying the potential applied to the electrodes of the calorimeter. This study is needed for the case where the nominal value of the potential could not be applied: if we know the shape of the Energy versus High Voltage curve we will be able to perform the necessary corrections.

Then we will briefly analyze the signal shape and the noise, to quantify its influence on the energy measurement of physical events.

The central part of this thesis will be dedicated to the High Voltage corrections that have to be implemented in order to obtain an uniform energy response. In fact in the End-Cap the liquid argon gap is not constant in the η direction so to have an uniform response we should apply to the electrodes a continuously varying potential. Actually, the potential is set by steps (two in the EMEC inner wheel), so remains a non-uniformity for each High Voltage sector that has to be taken in account. Finding the corrections that give the

most uniform response represents the main task of this work.

In the last chapter we will study the spatial resolution of the EMEC inner wheel. The guideline in the construction of the inner wheel was not that to give it a good spatial resolution, because its main goal is the measurement of the missing energy; anyway a precise measurement of spatial resolution (especially the resolution on the ϕ coordinate) will give orders of magnitude useful for a simulation on the measurement of the luminosity using a channel in which a pair of electrons is produced at a ϕ -angle of 180 in the high- η region.

Chapter 1

The Standard Model

The modern particle physics describes the world in terms of particles: the matter is composed by elementary particles and even the interactions between them are interpreted as exchanges of another kind of them called *field* particles. The theory that describes these interactions and whose results are very well confirmed by experiments so far is called Standard Model and it was formulated by Weinberg, Glashow and Salam.

The interactions mediated by the field particles are the following:

- **electromagnetic:** the field particle is the photon, a massless and spin 1 particle. The electromagnetic interaction concerns all the particles that have an electric charge.
- **weak:** it is the force that causes the β decays. It is mediated by three massive vector bosons: W^+ , W^- and Z^0 .
- **strong:** it is the force that keeps the constituents of the nuclei together. The field particles are 8 massless vector bosons called *gluons*.
- **gravitation:** it is the force that acts between all particles with mass. Its field particles have not been yet directly observed. They should be spin 2 particles called *gravitons*.

In fact the Standard Model describes only 3 of these interactions: it has unified the three first interactions but it cannot describe the gravitation. The unification of the Standard Model with a Quantum theory of the gravitation is maybe the most fascinating theoretical challenge.

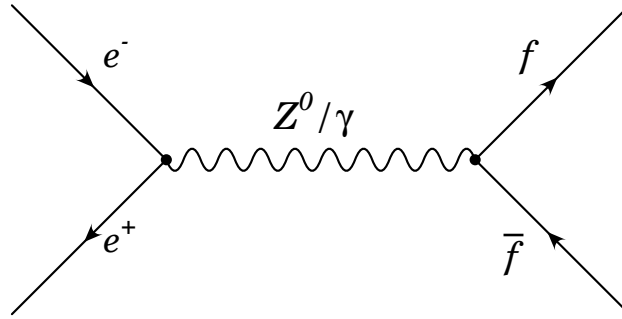


Figure 1.1: Feynman diagram for lepton pair production mediated by the photon or by the Z bosons. The latter is possible even at energies smaller than the Z mass.

1.1 The elements of the Standard Model

The matter particles are called *fermions* because they obey the Fermi-Dirac statistics. They have half-integer spin and they can further on be divided in leptons and quarks and they are grouped in three different families. The quarks are the particles that compose the mesons (as π^0 , π^+ , π^- , J/Ψ) and the baryons (the proton, the neutron etc...). We have to add that each fermion has an antiparticle, that is, a particle of the same mass, spin but with an opposite electric charge.

The field particles (the photon, the W^+ , W^- , Z^0 and the gluons) are integer spin particles called bosons that obey the Bose-Einstein statistics. When they mediate the interactions, they are *virtual* particles: that is, if we consider the four-momentum $E = (m, 0, 0, p_z)$ and the Minkowsky metric $(1, 0, 0, -1)$, for them the relation

$$E^2 = m^2 + p^2 \quad (1.1)$$

does not occur. These particles are created and then annihilated in a time interval shorter than $\Delta E/\hbar$ (from the Heisenberg uncertainty relations), so that mass conservation is preserved. For this reason we can have the process of Figure 1.1 even at energies smaller than the Z mass.

The Standard Model is a Quantum Field Theory based on the gauge invariance under the groups $SU(2)_L \times U(1)_Y$ for the electroweak domain and under the group $SU(3)_C$ for the sector of strong interaction. So we have to use a Lagrangian that is invariant under these transformations. We consider for the time being only the electroweak sector.

The modern approach to a Quantum Field Theory is to take as basic requirement the invariance with respect to local phase transformation of the

Fam.	Leptons			Quarks		
	Part.	Charge	Mass	Part.	Charge	Mass
1	e	-1	511 keV/c^2	u	2/3	1 MeV/c^2
	ν_e	0	< $1eV/c^2$	d	-1/3	3-9 MeV/c^2
2	μ^-	-1	105.6 MeV/c^2	c	2/3	1.15 GeV/c^2
	ν_μ	0	< $0.19MeV/c^2$	s	-1/3	75-170 MeV/c^2
3	τ^-	-1	1.777 GeV/c^2	t	2/3	178 GeV/c^2
	ν_τ	0	< $18.2 MeV/c^2$	b	-1/3	4.0-4.4 GeV/c^2

Table 1.1: The matter particles of the Standard Model.

matter fields: then we are naturally led to introduce a gauge field coupled to the matter field through the replacement of the ordinary derivative with a covariant one.

1.2 The Quantum Electro-Dynamics

Let us consider the free lagrangian density of the QED [1]

$$\mathcal{L} = \bar{\psi}(x)(i\gamma^\mu\partial_\mu - m)\psi(x) \quad (1.2)$$

and the following local phase transformations

$$\left. \begin{aligned} \psi(x) &\rightarrow \psi'(x) = \psi(x)e^{-iqf(x)} \\ \bar{\psi}(x) &\rightarrow \bar{\psi}'(x) = \bar{\psi}(x)e^{+iqf(x)} \end{aligned} \right\} \quad (1.3)$$

Under these transformation, the QED lagrangian density is not invariant, it becomes

$$\mathcal{L} \rightarrow \mathcal{L}'_0 = \mathcal{L} + q\bar{\psi}(x)\gamma^\mu\psi(x)\partial_\mu f(x) \quad (1.4)$$

Invariance in the theory can be restored if we augment \mathcal{L}_0 by a term \mathcal{L}_I such that the new lagrangian density $\mathcal{L} = \mathcal{L}_0 + \mathcal{L}_I$ is invariant. This can be achieved by associating with the matter field $\psi(x)$ a gauge field $A_\mu(x)$ which transforms according to the gauge transformation

$$A_\mu(x) \rightarrow A'_\mu = A_\mu(x) + \partial_\mu f(x) \quad (1.5)$$

The interaction between matter and gauge field is then specified by replacing the ordinary derivative ∂_μ by the covariant derivative

$$D_\mu\psi(x) = [\partial_\mu + iqA_\mu(x)]\psi(x) \quad (1.6)$$

Under the coupled gauge transformations (1.3) and (1.5) the covariant derivative transforms in the same way as the field $\psi(x)$ itself.

1.3 The weak interactions

At the beginning we assume that all leptons are massless, so that the free-lepton lagrangian density is

$$\mathcal{L}_l = i[\bar{\psi}_l(x)\gamma^\mu\partial_\mu] \quad (1.7)$$

We know that weak interactions involve only the left handed lepton fields, so it is better to write them as

$$\left. \begin{aligned} \psi^L(x) &= P_L\psi(x) \\ \psi^R(x) &= P_R\psi(x) \end{aligned} \right\} \equiv \frac{1}{2}(1 \mp \gamma_5)\psi(x) \quad (1.8)$$

If we combine the ψ_l^L and the $\psi_{\nu_l}^L$ in a two-component field of the form

$$\Psi_l^L(x) = \begin{pmatrix} \psi_{\nu_l}^L(x) \\ \psi_l^L(x) \end{pmatrix} \quad (1.9)$$

we get

$$\mathcal{L}_0 = i[\bar{\Psi}_l^L(x)\partial_\mu\gamma^\mu\Psi_l^L(x) + \bar{\psi}_l^R(x)\partial_\mu\gamma^\mu\psi_l^R(x) + \bar{\psi}_{\nu_l}^R(x)\partial_\mu\gamma^\mu\psi_{\nu_l}^R(x)] \quad (1.10)$$

For the two-component left handed field the possibility arises of two-dimensional transformations that leave bilinear forms $\bar{\Psi}_l^L(x)\dots\Psi_l^L(x)$ invariant. For this purpose we introduce three Hermitian matrices

$$\tau_1 = \begin{pmatrix} 0 & 1 \\ 1 & 0 \end{pmatrix}, \quad \tau_2 = \begin{pmatrix} 0 & -i \\ i & 0 \end{pmatrix}, \quad \tau_3 = \begin{pmatrix} 1 & 0 \\ 0 & -1 \end{pmatrix} \quad (1.11)$$

which satisfy the commutation relations

$$[\tau_i, \tau_j] = 2i\epsilon_{ijk}\tau_k \quad (1.12)$$

The operator $U(\alpha) \equiv \exp(i\alpha_j\tau_j/2)$ is unitary for any three real numbers $\alpha = (\alpha_1, \alpha_2, \alpha_3)$, and the set of transformations

$$\left. \begin{aligned} \Psi_l^L(x) \rightarrow \Psi_l'^L(x) &= U(\alpha)\Psi_l^L(x) \equiv \exp(i\alpha_j\tau_j/2)\Psi_l^L(x) \\ \bar{\Psi}_l^L(x) \rightarrow \bar{\Psi}_l'^L(x) &= \bar{\Psi}_l^L(x)U^\dagger(\alpha) \equiv \bar{\Psi}_l^L(x)\exp(-i\alpha_j\tau_j/2) \end{aligned} \right\} \quad (1.13)$$

leaves bilinear terms like those in (1.10) invariant. The operators $U(\alpha)$ are 2×2 unitary matrices with the property that $\det U(\alpha) = +1$ and they are called $SU(2)$ transformations. Then we define each right-handed lepton field to be invariant under $SU(2)$ transformations. However, these are global transformations while we are interested in local phase transformations; we

will see that if we want to generalize (1.13) to local transformations, we have to introduce some gauge fields to preserve the invariance. These local phase transformations are

$$\left. \begin{aligned} \Psi_l^L(x) &\rightarrow \Psi_l'^L = \exp[ig\tau_j\omega_j(x)/2]\Psi_l^L(x) \\ \bar{\Psi}_l^L(x) &\rightarrow \bar{\Psi}_l'^L = \bar{\Psi}_l^L(x)\exp[-ig\tau_j\omega_j(x)/2] \\ \psi_{l,\nu_l}^R &\rightarrow \psi_{l,\nu_l}'^R(x) = \psi_{l,\nu_l}^R \\ \bar{\psi}_{l,\nu_l}^R &\rightarrow \bar{\psi}_{l,\nu_l}'^R(x) = \bar{\psi}_{l,\nu_l}^R \end{aligned} \right\} \quad (1.14)$$

where $\omega_j(x)$, $j = 1, 2, 3$ are three arbitrary differentiable functions of x and g is a real constant that will play the role of a coupling constant. If we apply them to (1.10) we note that the lagrangian is not invariant but transforms as

$$\mathcal{L}_0 \rightarrow \mathcal{L}'_0 \equiv \mathcal{L}_0 - \frac{1}{2}g\bar{\Psi}_l^L(x)\tau_j\gamma^\mu\partial_\mu\omega_j(x)\Psi_l^L(x) \quad (1.15)$$

We obtain an invariant Lagrangian density if we replace the ordinary derivative by the covariant one:

$$\partial^\mu\Psi_l^L(x) \rightarrow D^\mu\Psi_l^L(x) = [\partial^\mu + ig\tau_jW_l^\mu(x)/2]\Psi_l^L(x) \quad (1.16)$$

In (1.16) we were forced to introduce three real gauge fields. To have covariant derivatives that transform as the matter fields, such gauge fields have to transform as follows

$$W_i^\mu \rightarrow W_i'^\mu(X) = W_i^\mu - \partial^{mu}\omega_i(x) - g\epsilon_{ijk}\omega_j(x)W_k^\mu(x) \quad (1.17)$$

We consider now U(1) local phase transformations for the weak-interaction lagrangian:

$$\left. \begin{aligned} \psi(x) &\rightarrow \psi'(x) = \exp[ig'Yf(x)]\psi(x) \\ \bar{\psi}(x) &\rightarrow \bar{\psi}'(x) = \bar{\psi}(x)\exp[-ig'Yf(x)] \end{aligned} \right\} \quad (1.18)$$

g' is a real number, $f(x)$ an arbitrary function and $Y = -1/2, -1, 0$ is the weak hypercharge associated respectively with the fields $\Psi_l^L(x)$, $\psi_l^R(x)$, $\psi_{\nu_l}^R$. As in the QED, the lagrangian is invariant replacing the ordinary derivative by the covariant one, with the gauge field transforming in the usual way.

$$\left. \begin{aligned} \partial^\mu\psi(x) &\rightarrow D^\mu\psi(x) = [\partial^\mu + ig'YB^\mu(x)]\psi(x) \\ B^\mu(x) &\rightarrow B'^\mu(x) = B^\mu(x) - \partial^\mu f(x) \end{aligned} \right\} \quad (1.19)$$

We now define the fields $W_i^\mu(x)$ to be invariant under U(1) gauge transformations and B^μ under SU(2) ones. So the lagrangian density is said to be $SU(2) \times U(1)$ invariant and the interaction part of the lagrangian is

$$\mathcal{L}_I = -gJ_i^\mu(x)W_{i\mu}(x) - g'J_Y^\mu(x)B_\mu(x) \quad (1.20)$$

We introduce the following non-Hermitian gauge field:

$$W_\mu(x) = \frac{1}{\sqrt{2}}[W_{1\mu}(x) - iW_{2\mu}(x)] \quad (1.21)$$

and this linear combination of the Hermitian fields A_μ and Z_μ

$$\left. \begin{aligned} W_{3\mu}(x) &= \cos\theta_W Z_\mu(x) + \sin\theta_W A_\mu(x) \\ B_\mu(x) &= -\sin\theta_W Z_\mu(x) + \cos\theta_W A_\mu(x) \end{aligned} \right\} \quad (1.22)$$

where θ_W is the weak mixing angle. If we require that the electromagnetic field is coupled to electric charge in the usual way (by the term $-s^\mu(x)A_\mu(x)$) we have to put $g\sin\theta_W = g'\cos\theta_W = e$, and with some calculations we arrive to:

$$\begin{aligned} \mathcal{L}_I &= -s^\mu(x)A_\mu(x) - \frac{g}{2\sqrt{2}}[J^{\mu\dagger}(x)W_\mu(x) + J^\mu(x)W_\mu^\dagger(x)] \\ &\quad - \frac{g}{\cos\theta_W}[J_3^\mu(x) - \sin^2\theta_W s^\mu(x)/e]Z_\mu(x). \end{aligned} \quad (1.23)$$

J_1^μ, J_2^μ are the weak isospin currents, while the terms that multiply the Z_μ represent a neutral current (s_μ is the electromagnetic current). Finally, we have to add terms that describe the gauge bosons when no leptons are present. For the moment we will consider these bosons massless. These terms are

$$\mathcal{L}^B = -\frac{1}{4}B_{\mu\nu}(x)B^{\mu\nu}(x) - \frac{1}{4}G_{i\mu\nu}(x)G_i^{\mu\nu}(x) \quad (1.24)$$

with

$$\begin{aligned} B^{\mu\nu}(x) &\equiv \partial^\nu B^\mu(x) - \partial^\mu B^\nu(x) \\ G_i^{\mu\nu} &\equiv \partial^\nu W_i^\mu(x) - \partial^\mu W_i^\nu(x) + g\epsilon_{ijk}W_j^\mu(x)W_k^\nu(x) \end{aligned} \quad (1.25)$$

We have to observe that our Lagrangian does not have any mass term. The only fermionic term that is invariant under U(1) transformations is

$$m\bar{\psi}_f\psi_f = m(\bar{\psi}_f^L\psi_f^R + \bar{\psi}_f^R\psi_f^L) \quad (1.26)$$

where ψ_f^L are the isospin doublets for leptons (l, ν) and quarks (q_u, q_d) and ψ_f^R are the singlets. But this term mixes up the left and right components: it is not invariant under the $SU(2)_L$ transformations (the weak interaction concerns only the left components of the fermion doublets). We have to introduce the mass terms with a mechanism which retains the gauge invariance.

The method currently used to give the particles a mass is called *Higgs mechanism*: we introduce a complex scalar field that spontaneously breaks

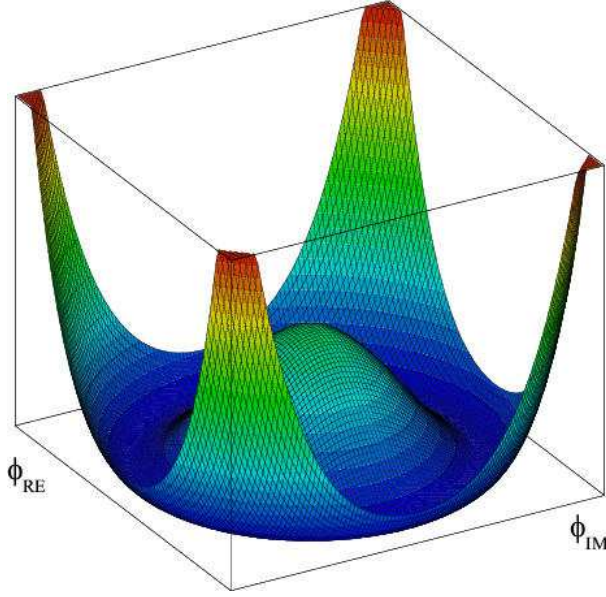


Figure 1.2: Potential used for the Higgs mechanism

the symmetry of the Lagrangian when we give it a non vanishing vacuum expectation value. One possible way is to choose the following potential

$$V(\phi) = \mu^2|\phi|^2 + \lambda|\phi|^4 \quad \text{with } \mu^2 < 0 \text{ and } \lambda > 0 \quad (1.27)$$

using these conditions we have a minimum of the potential (in the case of a complex scalar field we have a circumference of minimum) for field value different from zero. When we choose one minimum we break the symmetry. The Higgs Lagrangian is then

$$L_{Higgs} = (D_\mu\phi)(D^\mu\phi)^\dagger - V(\phi) \quad (1.28)$$

with the covariant derivative of the form

$$D_\mu = \partial_\mu - ig\frac{Y}{2}B^\mu - ig'\frac{\sigma_a}{2}W^{a\mu} \quad (1.29)$$

With the potential described above, we are led to

$$|\langle 0|\phi|0\rangle| = \sqrt{\frac{-\mu^2}{2\lambda}} \equiv \frac{v}{\sqrt{2}} \quad (1.30)$$

where v is the v.e.v, that is, the value of the Higgs field in the vacuum. So we can rewrite the Higgs potential using

$$\phi(x) = \exp[i\frac{\vec{f}}{2} \cdot \vec{\theta}(x)] \frac{1}{\sqrt{2}} \begin{pmatrix} 0 \\ v + \sigma(x) \end{pmatrix} \quad (1.31)$$

The fields $\theta(x)$ are massless fields called *Goldstone bosons*; they are not physical and they can be eliminated by the rotation

$$\phi(x) \rightarrow \exp\left[-i\frac{\vec{f}}{2} \cdot \vec{\theta}(x)\right]\phi(x) \quad (1.32)$$

Using this gauge, the kinetic term becomes

$$(D_\mu\phi)(D_\mu\phi)^\dagger = \frac{1}{2}\partial_\mu\sigma\partial^\mu\sigma + \frac{g^2}{4}(v + \sigma)^2[W_\mu^\dagger W^\mu + \frac{1}{s\cos^2\theta_W}Z_\mu Z^\mu] \quad (1.33)$$

We see that the mass term for the bosons W and Z appear, while the photon remains massless

$$\left. \begin{aligned} M_W &= \frac{1}{2}vg \\ M_Z &= \frac{1}{2\cos\theta_W}vg = \frac{M_W}{\cos\theta_W} \end{aligned} \right\} \quad (1.34)$$

The Higgs mechanism can be applied also to give mass to the fermions. One has to introduce in the Lagrangian some terms called *Yukawa terms*

$$\begin{aligned} L_{Yukawa} = (\bar{q}_u, \bar{q}_d) \left[c^{(d)} \begin{pmatrix} \phi^{(+)} \\ \phi^{(0)} \end{pmatrix} (q_d)_R + c^{(u)} \begin{pmatrix} \phi^{(0)\dagger} \\ -\phi^{(+)\dagger} \end{pmatrix} (q_u)_R \right] \\ + (\bar{l}, \bar{\nu}_l) c^{(l)} \begin{pmatrix} \phi^{(+)} \\ \phi^{(0)} \end{pmatrix} (l)_R + h.c \end{aligned} \quad (1.35)$$

and after the spontaneous symmetry breaking we get

$$L_{Yukawa} = -(1 + \frac{H}{v})(m_{q_d}\bar{q}_d q_d + m_{q_u}\bar{q}_u q_u + m_l\bar{l}l) \quad (1.36)$$

with

$$(m_{q_d}, m_{q_u}, m_l) = -\frac{v}{2}(c^{(d)}, c^{(l)}) \quad (1.37)$$

1.3.1 CKM matrix

We have to precise that the fermions mass eigenvalues written in Table 1.1 differ from the eigenstates of the weak interaction. To go from one base to the other we have a 3×3 matrix called the Cabibbo - Kobayashi- Maskawa matrix (CKM). This matrix has to be applied to the quarks of charge $-1/3$:

$$\begin{pmatrix} d' \\ s' \\ b' \end{pmatrix} = \begin{pmatrix} V_{ud} & V_{us} & V_{ub} \\ V_{cd} & V_{cs} & V_{cb} \\ V_{td} & V_{ts} & V_{tb} \end{pmatrix} \begin{pmatrix} d \\ s \\ b \end{pmatrix} \quad (1.38)$$

A parametrisation of this matrix has been performed by Wolfenstein [2]

$$V_{CKM} = \begin{pmatrix} 1 - \frac{\lambda^2}{2} & \lambda & A\lambda^3(\rho - i\eta) \\ -\lambda & 1 - \frac{\lambda^2}{2} & A\lambda^2 \\ A\lambda^3(1 - \rho - i\eta) & -A\lambda^2 & 1 \end{pmatrix} \quad (1.39)$$

with $\lambda \sim 0.22$. We actually see that the couplings between quarks of the same family are preferred.

1.4 The Strong Interactions (QCD)

As for the electro-weak interactions, we try to formulate a Lagrangian that will be invariant under a specific transformation group. In this case the group is the $SU(3)_C$ one, where C is the color quantum number [3]. There are 8 gluons described by this gauge group. The QCD Lagrangian can be written as:

$$\begin{aligned} L_{QCD} &= L_{Bosons} + L_{Fermions} \\ &= -\frac{1}{4}F_{\mu\nu}^a F^{a\mu\nu} + i\sum_q (\overline{\psi}_q^i \gamma_\mu (D^\mu)_{ij} \psi_q^j - m_q \overline{\psi}_q^i \psi_q^j) \end{aligned} \quad (1.40)$$

with

$$\begin{aligned} F_{\mu\nu}^a &= \partial_\mu G_\nu^a - \partial_\nu G_\mu^a - g_s f_{abc} G_\mu^b G_\nu^c \\ (D_\mu)_{ij} &= \delta_{ij} \partial_\mu - ig_s \sum_a \frac{\lambda_{ij}^a}{2} G_\mu^a \end{aligned} \quad (1.41)$$

For a detailed discussion on QCD and, in general, on non-Abelian theories, see [3]

1.5 Successes and failures of the SM and future scenarios

The Standard Model has had several successes:

- It is a Quantum Field Theory that is renormalizable and that unifies electromagnetic, weak and strong interactions.
- It resolves the problem of giving a mass to the vector bosons and to the fermions.
- The standard Model has been deeply tested in the electro-weak sector and all its predictions differ from the experimental data by less than 0.1%

However, the Standard Model presents some problems.

- The Higgs boson has not been observed yet. Its search is the main goal of the LHC.
- if we consider a Great Unification Theory (GUT), the electroweak scale (~ 200 GeV) is very small if compared to the great unification scale (energy to which electroweak and strong interactions converge).
- In a GUT, the running coupling constants of the electromagnetic, weak and strong interactions do not converge.
- The Standard Model is based upon 19 parameters: it is a great number and there is no explanation of the fact that the parameters number should actually be 19.
- It does not explain the neutrino masses.

All these things make us think that the Standard Model is “only” an approximation of a more fundamental theory.

There are lots of theories that are trying to resolve the failures of the Standard Model. The most promising one is the Super Symmetric Standard Model: the supersymmetry is an extension of the Poincaré group. The basic idea is the association of a fermion (respectively a boson) to each boson (respectively fermion) in a gauge supermultiplet. The particles in the same supermultiplet have the same quantum numbers with the exception of the spin number that differs of $1/2$ in \hbar units. These particles allow the cancellation of the radiative corrections that in the S.M. make the Higgs mass divergent. Moreover, using these supersymmetric particles, the three coupling constants converge to the same value to the same energy scale. The supersymmetric partners of the fermions are called *sfermions* (squark, sleptons...) while the bosons' partners have names that end up with *-ino* (Winos, photinos...).

However there is a problem with this model: if the Supersymmetry exists at the electroweak energy scale, we should have already observed the supersymmetric partners because they have the same mass as the ordinary particles, but none of such particles has been detected. So we are led to think that the supersymmetry is spontaneously broken, giving origin to very massive (at least 100 GeV) supersymmetric partners [4], [5].

A detailed description of Super Symmetric Theories are beyond the scope of this thesis. We only say that Super Symmetric Theories have a lot of application in other physical fields as cosmology, where the lightest supersymmetric particles can be at the responsible of the Dark Matter problem.

Chapter 2

The ATLAS experiment at LHC

The LHC hadronic collider will be a machine for high energy physics research where particles will collide at center of mass energies never reached before. There will be collisions between proton-proton packets with a center of mass (CM) energy of 14 TeV with a luminosity of $10^{34} \text{cm}^{-2} \text{sec}^{-1}$. The main goal of this machine is the discovery of the Higgs boson, the only particle of the Standard Model not yet observed, but at LHC there will be also searches for supersymmetric particles, for heavy intermediate vector bosons (W' Z'), study of CP violation and even heavy ions will be accelerated to study the matter behaviour at high density.

The LHC collider is being built in the same tunnel as LEP (the previous electron-positron collider), so it has a length of 27 km. The proton packets will circulate in opposite direction and there will be 4 interaction points where the following detectors will be placed:

- ATLAS (A Toroidal Lhc ApparatuS): designed for the studies of processes with high momentum transfer and photons, leptons and hadronic jets identification.
- CMS (Compact Muon Spectrometer): same potentiality as ATLAS.
- LHCb, for the study of quark b physics, important for CP violation.
- ALICE (A Large Ion Collider Experiment), it will study the interactions between heavy ions.

A proton-proton collider has been chosen, instead of another electron-positron one, especially because of the synchrotron radiation. In fact charged particles, when they are accelerated, emit radiation. In a circular machine

the radiation is a continuous spectrum one, called synchrotron radiation and this causes loss of energy. In time unit this is

$$\frac{dE}{dt} \propto \frac{\gamma^4}{R} \quad (2.1)$$

where

$$\gamma = \frac{1}{\sqrt{1-\beta^2}} = \frac{E}{m} \text{ with } \beta = \frac{v}{c} \quad (2.2)$$

We can see that at the same energy, heavier particles have smaller γ values and so a smaller loss of energy by synchrotron radiation.

2.1 Proton-Proton interaction and Higgs boson production.

The proton-proton interactions are more complicated than the ones we had at LEP, because the protons are not elementary particles and their description is based on simplified models as the parton model. This model describes a baryon as composed by elementary particles (quarks and gluons) that can move freely inside the proton (*asymptotic freedom* [3]) but that do not exist as isolated particles. The phenomenon of the asymptotic freedom brings an uncertainty on the CM energy value in a parton-parton interaction, because we do not know exactly which fraction of the hadron momentum is carried by a single gluon or quark, we know only the energy of the two hadron systems. For inclusive processes, the energy and the momentum of a particle can be written as

$$E = m_T \cosh y, \quad p_x, p_y, p_z = m_T \sinh y \quad (2.3)$$

where m_T is the transverse mass defined as $m_T = m^2 + p_x^2 + p_y^2$ and y is the rapidity:

$$y = \frac{1}{2} \log \left(\frac{E + p_z}{E - p_z} \right) = \log \left(\frac{E + p_z}{m_T} \right) = \tanh^{-1} \left(\frac{p_z}{E} \right) \quad (2.4)$$

Under a Lorentz boost in the z direction, the rapidity changes as $y \rightarrow y - \tanh^{-1}(\beta)$ and so it is invariant under a Lorentz transformation. Hence it is useful to use the rapidity as a coordinate because in this way we'll get a Lorentz invariant cross section. Introducing the the 4-momentum p in polar coordinates $p = (E, p_x, p_y, p_z) = E(1, \beta \sin\theta \cos\phi, \beta \sin\theta \sin\phi, \beta \cos\theta)$ we get:

$$y = -\frac{1}{2} \log \frac{1 - \beta \cos\theta}{1 + \beta \cos\theta} \quad (2.5)$$

and because for particles that travel at the speed of light $\beta \rightarrow 1$ it is useful to use

$$\eta = -\log\left(\tan\frac{\theta}{2}\right) \quad (2.6)$$

where the quantity η is called *pseudorapidity* and can be measured in any case, even when the mass and the momentum of the particle are unknown. For this reason in hadronic colliders the events are described using the coordinates η , ϕ and z .

We now briefly describe the Standard Model Higgs production and decay channels to which the greatest attention will be given at LHC.

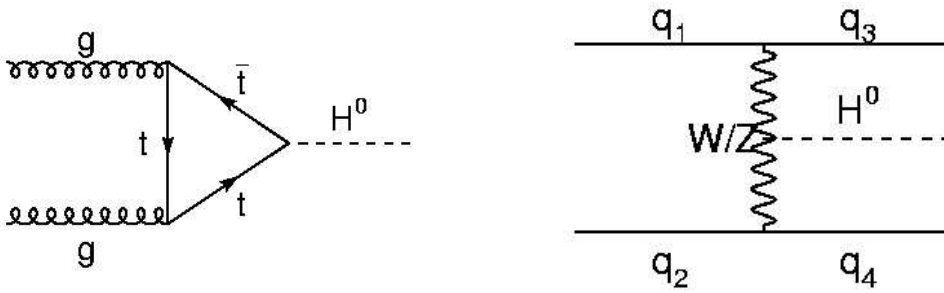


Figure 2.1: *Left*: Higgs production by the gluon fusion channel *Right*: Higgs production by the vector boson fusion

Higgs production.

- gluon fusion dominates for low higgs mass values but also for values of 1 TeV. Its contribution to the cross section is 50%. It is even possible to have a $g\bar{g} \rightarrow t\bar{t}, H$.
- vector boson fusion $q\bar{q} \rightarrow q\bar{q}V^*V^* \rightarrow q\bar{q}H^0$ important for masses of the order of Tev.
- *Higgsstrahlung* $q\bar{q} \rightarrow V \rightarrow V H^0$ but it is more important in electron-positron colliders as LEP.

Higgs decay. Even the decay processes cross sections vary with the Higgs mass.

- $80 < M_H < 130 \text{ GeV}$. The most important channels are $H \rightarrow \gamma\gamma$ and $H \rightarrow 4e$. In this region the process with the highest cross section is the decay in $b\bar{b}$ but the QCD background is too high and it is very difficult to distinguish jets due to b decays from other jets.

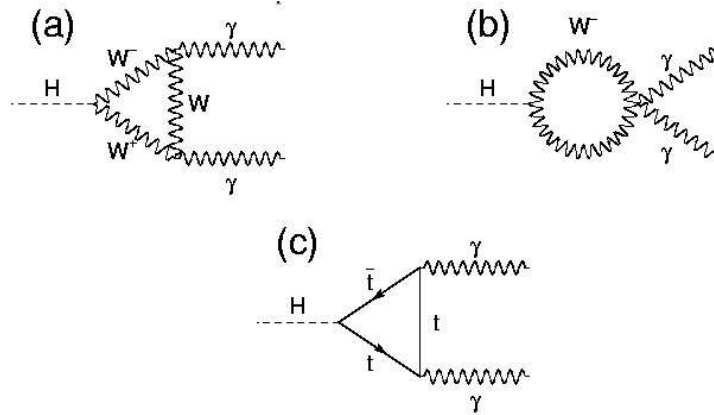


Figure 2.2: Three channels of the Higgs decay into two photons.

- $130 < M_H < 600$ $H \rightarrow ZZ \rightarrow 4l$. The reconstruction of events with lepton pairs allows us to get the Higgs mass from the value of their invariant mass.
- $M_H > 600$ GeV . The most interesting decays are $H \rightarrow ZZ \rightarrow l^-l^+ \nu\bar{\nu}$ and $H^0 \rightarrow W^+W^- \rightarrow l\nu_l + 2jet$. The first requires a very high precision in the missing p_T determination due to the impossibility to detect neutrinos, the second great capacity to detect the two jets among those of the background and to reconstruct their invariant mass.

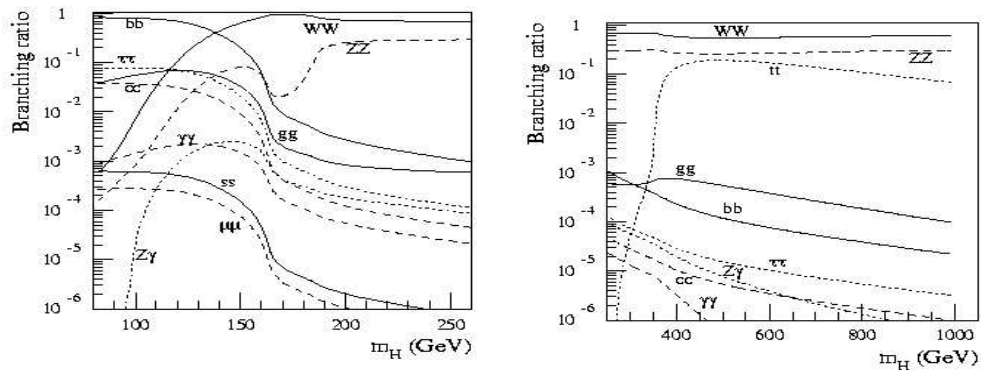


Figure 2.3: How the cross sections for Higgs production change with the Higgs mass.

In Figure 2.4 the significance for the expected signal of the Higgs boson for various channels is given. The significance is defined by the relation:

$$\mathcal{S} = \frac{S}{\sqrt{B}} \quad (2.7)$$

where S is the number of events what we can attribute to Higgs production and B is the number of background events. Standard significance value for discovery is $S > 5\sigma$.

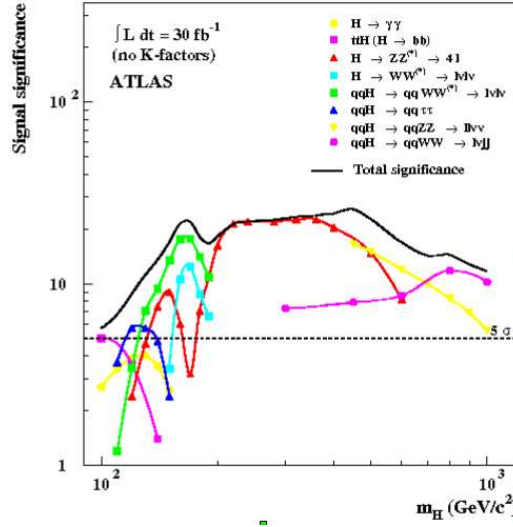


Figure 2.4: Significance for the Higgs boson discovery for various channel for an integrated luminosity of 10^5 pb.

2.2 The ATLAS detector

ATLAS is a multiscopes detector, that is an ensemble of many subdetectors, all of them with a very specific task. The ATLAS detector has a cylindrical symmetry with the axis parallel to the beam. From the center upstream to the radial coordinate we find different components. Briefly:

Inner Detector, whose goal is the reconstruction of tracks of charged particles in the interaction point closest region.

Central Solenoid, that produces the magnetic field necessary to bend the charged particles tracks and to determine their electric charges and their

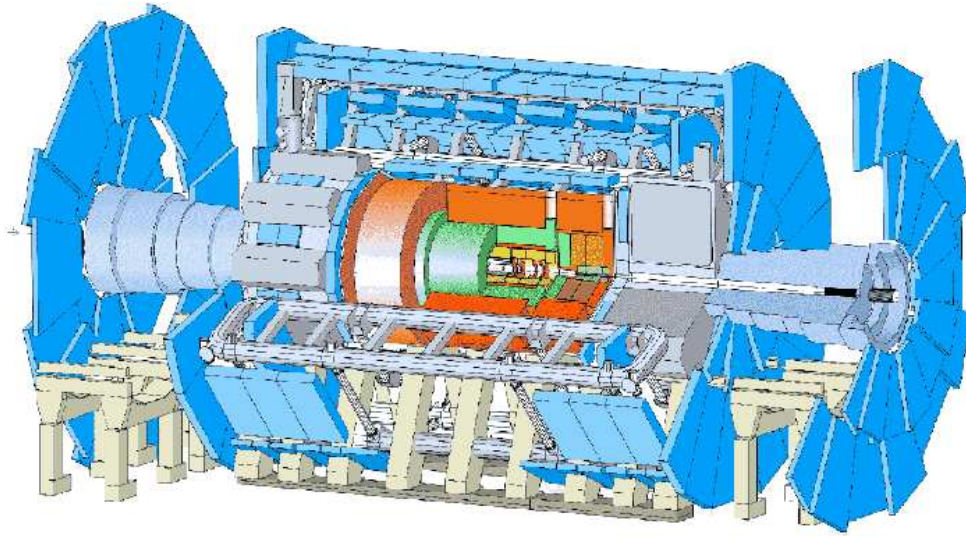


Figure 2.5: Detector general picture: Atlas is 42 metres long and 22 metres high

transverse momentum.

Electromagnetic calorimeter, whose task is position and charged particle deposited energy determination.

Hadronic calorimeter, for the measurements of the energy and the position of hadrons and hadrons jets.

Forward calorimeter, that measures energy and position of charged particles created in region with $\eta > 3.2$ up to $\eta = 4.9$.

Toroidal magnets, to deflect muons trajectory, because they cross easily the calorimeters. The goal is to measure their transverse momentum and energy by the *muon spectrometer*.

We now examine in a more detailed way the different components.

2.2.1 Inner Detector

The Inner Detector (ID) is the subdetector closest to the beam pipe and is composed of three principal components [6]:

- *Pixel vertex detector.* The pixel structure has been studied to ensure a high resolution in tracks and a good reconstruction of production and decay vertex (it will be fundamental especially for processes that involve the study of the kinematics of b quarks and τ decays). Because of its closeness to the center of the interactions, it will be subjected to a very high radiation dose to which it will have to resist for at least ten years (about 300 kGy) so, very important will be also its radiation resistance.
- *Semiconductor trackers.* Made up of 8 silicon microstrips layers, with the task to measure in 8 points the R , ϕ and z coordinates of the events. The spatial resolution achievable is of $16 \mu m$ in R and ϕ and $580 \mu m$ in z .
- *Transition radiation trackers.* Composed by straw detectors each one with a $4 mm$ diameter and with a golden wire of $30 \mu m$ of diameter in the middle. The channels for the signal read out are 420000 and each one provides the drift time measurement with a spatial resolution of $170 \mu m$.

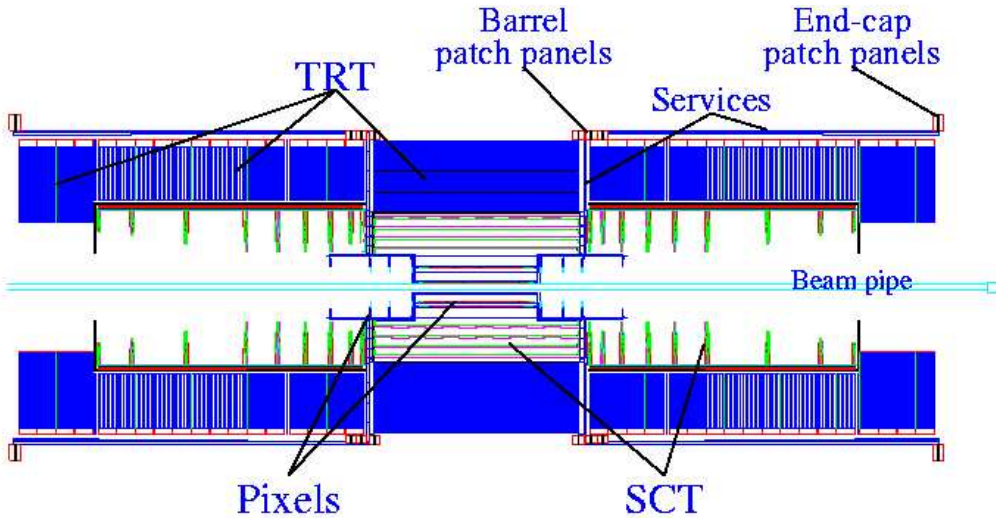


Figure 2.6: The inner detector and its components.

As we said the inner detector task is the determination of the trajectory of charged particles that have origin in the interaction points of the proton packets. This has to occur in a way that causes the minimum energy absorption, because their energy will be measured by the calorimeters. Then the

presence of material causes the phenomenon of bremsstrahlung, pair production that increase the background noise and generate false signals. Moreover, the presence of pair production increases the showers dimension, making the reconstruction of their direction worse. So is of critical importance the compromise on the material quantity, that should not be too much in order not to attenuate the signal and not too little in order not to worsen the capacity of trajectory reconstruction.

2.2.2 The central solenoid.

The central solenoid produces a magnetic field of 2 Tesla that encloses the inner detector. Liquid helium temperatures are needed to put in superconductive state the material that constitute the spires of the solenoid. Keeping these temperatures is one of the numerous technological challenges required by an optimal behaviour of ATLAS.

2.2.3 Calorimeters.

The calorimeters will play a crucial role in LHC because while the intrinsic resolution of all the other sub-detectors decreases when the energy grows, their relative resolution gets better with the energy [7]. In the search of the Higgs boson, for energy from 80 GeV up to the limit of 1 TeV imposed by theory, the physicists will rely heavily on the informations given by the calorimeters, because the preferential channels will be $H \rightarrow \gamma\gamma$ and $H \rightarrow ZZ \rightarrow 4l$ and so the final state reconstructions will come from EM calorimeters (with the exception of $H \rightarrow ZZ \rightarrow 4\mu$, see section 2.2.4).

The tasks of the calorimeters present in all hadrons colliders are the following ones:

- energy and position measurements of photons and electrons.
- energy and direction of jet and transverse momentum for each event.
- particle identification.
- event selection.

At LHC these goals represent an enormous technological challenge because the high center of mass energy requires an excellent energy resolution from the GeV up to the TeV and the luminosity gives origin to 20 soft collisions on average at a luminosity of 10^{34} at each bunch crossing (that is, every 25 nsec), with lots of problems of pile-up. Of course is also required a high radiation resistance for at least 10 years to guarantee the operativity of the detector.

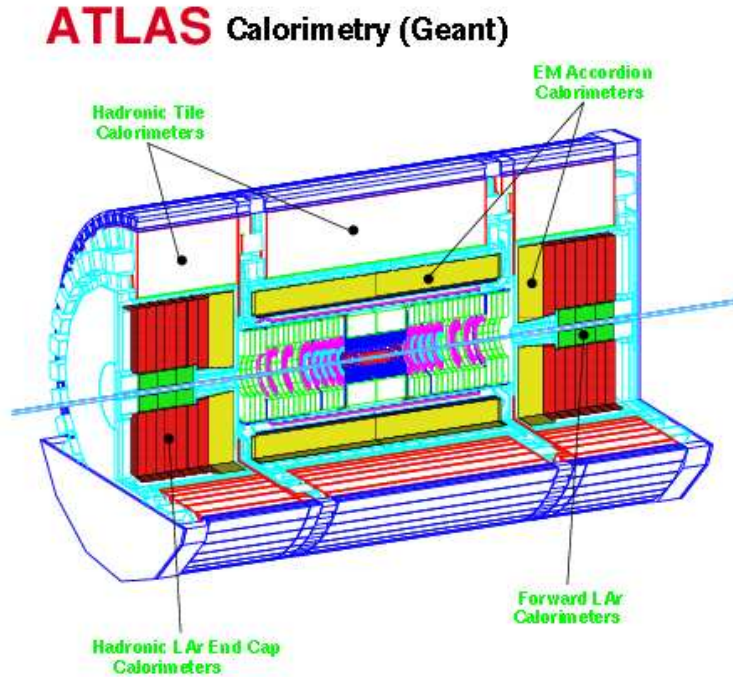


Figure 2.7: Sketch of the EM calorimeters.

Although the EM calorimeters will be employed in lots of operations, the greatest part of the studies will be devoted to the two channels for the Higgs bosons and to the search for supersymmetric particles.

Fundamental physical requirements.

- rapidity coverage: the largest acceptance in pseudorapidity values is needed to observe processes as $H \rightarrow \gamma\gamma$ or $H \rightarrow 4e$.
- electron reconstruction: is necessary for the tagging of semi-leptonic decay of quarks b , because reconstruction and identification of these electrons will improve by 10% the ATLAS b -tagging efficiency. This will be important for the decay $H \rightarrow b\bar{b}$, for b quark physics and for supersymmetric particle searches.
- excellent energetic resolution between 10 and 3000 GeV: for the two fundamental channels for the Higgs boson search, the maximal resolution on the Higgs mass has to be of the order of 1%. Generally, for a

calorimeter, the energy resolution is defined by the following relation:

$$\frac{\Delta E}{E} = \frac{b}{E} \oplus \frac{a}{\sqrt{E}} \oplus c \quad (2.8)$$

where b is the noise term (of the order of 400 MeV/E in ATLAS) due to electronic noise of the signal extraction chain, a is the sampling term due to the fluctuations of the energy deposited from the shower in the calorimeter and has to be smaller than $10\%/\sqrt{E}$. The $1/\sqrt{E}$ behaviour can be explained reminding that the deposited energy in the active medium is proportional to the number N of the produced secondary particles. The statistical error in this number, ΔN , can be assumed to be its square root: so

$$\left(\frac{\Delta E}{E} \right)_{\text{sampling}} \sim \frac{\Delta N}{N} = \frac{1}{\sqrt{N}} \sim \frac{1}{\sqrt{E}}. \quad (2.9)$$

Finally, c is a constant term generated by construction non-uniformities. This one is expected to be of the order of 0.7%. Multiplying the expression for the energy we can see that at high energies the dominant term is the constant one

$$\Delta E = b \oplus a\sqrt{E} \oplus cE \quad (2.10)$$

and it is for this reason that it has to be kept very small, while the noise contribution gets smaller at high energy.

- Thickness of at least $24 X_0$ to contain high energy showers in order to prevent that the resolution will get worse at high energy.
- shower direction measurements in θ with a $(50 \text{ mrad})/\sqrt{E}$ (E in GeV) resolution and excellent electron-jet and photon-jet separation, very important for background reduction in $H \rightarrow \gamma\gamma$ channel and in the $H \rightarrow 4e$ one.
- noise: the phenomena that contribute to the noise are the pile-up and the electronic noise of the read out chain. To minimize the pile up a fast response from the detector is needed and very fast electronics while for the electronic noise we need a high granularity.

Barrel and End-Cap calorimeters

The EM calorimeter is divided into a barrel part with $|\eta| < 1.45$, divided in two identical half barrels separated by a small gap of 6mm, and two end

caps $1.35 < |\eta| < 3.2$ composed by two coaxial wheels, the outer that covers the region of $1.35 < |\eta| < 2.5$ and the inner covering the $2.5 < |\eta| < 3.2$ regions. In the range with a pseudorapidity smaller than 1.8 the calorimeter is preceded by a presampler detector used to correct for the energy lost in the material upstream of the calorimeter.

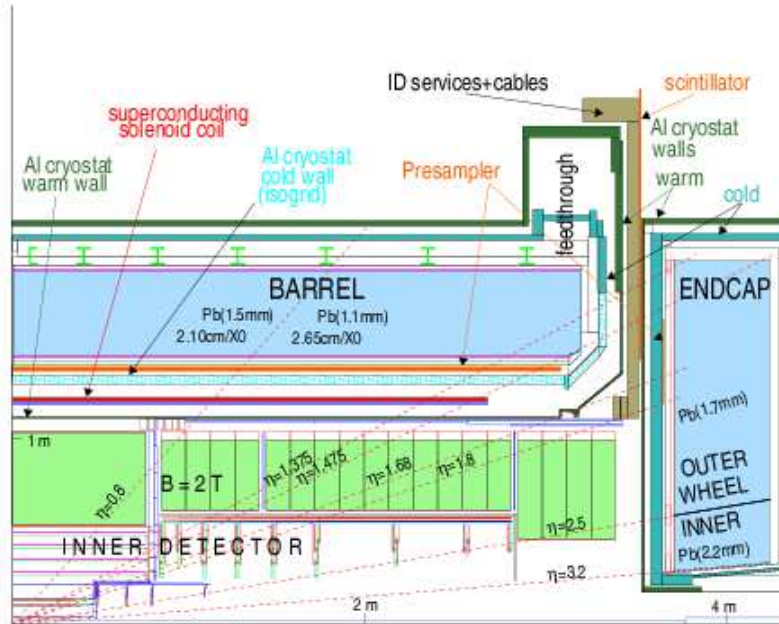


Figure 2.8: Longitudinal section of the EM calorimeters.

Generally speaking the EM calorimeters are divided into two kinds: sampling calorimeters and homogeneous calorimeters.

- In the sampling calorimeters there is an alternation of layers of absorber material and of active material, in which the electric charges generated by the ionization of the active material are collected from the electrodes.
- the homogeneous ones are composed by only one material, that is at the same time the absorber and the active material. These calorimeters are characterized by a very high energy resolution (a few $\%/ \sqrt{E}$) but they usually lack the longitudinal segmentation.

A sampling lead-liquid argon calorimeter has been chosen for ATLAS especially for reasons of cost and linearity of the response. However, with a sampling calorimeter we do not get all the energy but only a fraction that

η	lead thickness
0-0.8	1.5 mm
0.8-1.4	1.1 mm
1.4-2.5	1.7 mm
2.5-3.2	2.2 mm

Table 2.1: Absorber thickness at different η values.

moreover undergoes statistical fluctuations. This fraction is called *sampling fraction* and measures the ratio between the energy deposited in the active material by a minimum ionizing particle and the total energy lost in the detector (absorber+active material). In ATLAS this sampling fraction has the value:

$$F = \frac{\Delta E_{LAr}}{\Delta E_{LAr} + \Delta E_{Pb}} \simeq 19\% \quad (2.11)$$

It is the a term of the Formula 2.10 that takes in account these fluctuations.

ATLAS EM Barrel Calorimeter : The Barrel calorimeter is a lead-liquid argon detector with an accordion geometry, where Kapton-copper electrodes and lead-absorber plates are interleaved over its full coverage.

The accordion geometry provides a complete ϕ symmetry without azimuthal interruption. As we can see in the Table 2.1 the lead thickness has been chosen as a function of pseudorapidity to optimise the calorimeter performance in terms of energy resolution. The liquid argon gap has a constant thickness in the barrel while in the end cap, as described later, it varies with the radius in order to compensate the fact that in each wheel the absorbers have a constant thickness.

The EM barrel calorimeter is segmented in three longitudinal samplings:

- The first sampling has a thickness of $6 X_0$ and is divided in narrow strips in the η direction that give a fine scan. It has the role to identify with a great precision the direction of the electromagnetic shower and to determine its three-dimensional structure with the information on the ϕ direction. Furthermore it has to reject π_0 and jets background for physics channels involving isolated photons. It has a granularity of 0.0031×0.025 . The choice of a coarser strip size in ϕ is a consequence of the fact that showers that start in front of the solenoid are smeared in ϕ by the magnetic field. So it is useless trying to measure their fine structure in ϕ .

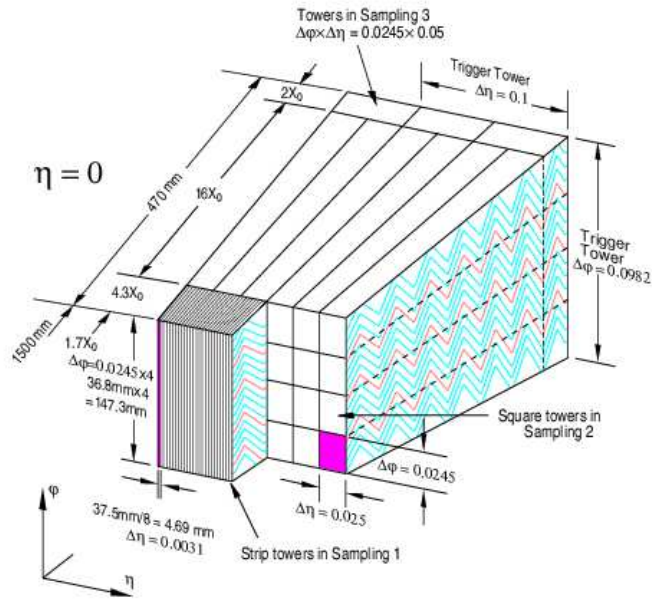


Figure 2.9: Readout granularity of the EM calorimeter.

- The second sampling has a thickness of $18 X_0$ and gets almost the total energy of the shower. Its granularity is of 0.025×0.025 . This granularity derives from the Moliere radius of the calorimeter ($\sim 2.5 \text{ cm}$ in the barrel) and allows us to use cluster sizes which are a compromise between the shower lateral containment and the contribution to the electronic and pile-up noise to the energy measurement. Moreover, this granularity allows us to distinguish between electromagnetic showers from showers produced by pions or jets. Up to energy of 50 GeV it is possible to use only the first two samplings, in order to avoid the contribution of electronic and pile-up noise of the third sampling to the energy measurements.
- The third sampling has a $12 X_0$ length and a coarser granularity because there is no more the necessity to determine the shower direction but only to collect the residual energy.

ATLAS EMEC The EMEC will be described in detail in section (2.3).

Hadronic Calorimeters

ATLAS has also an hadronic calorimeter for the jet and hadrons study: it is a sampling calorimeter composed by a barrel sector (divided in a central part that covers the region of $|\eta| < 1$ and two extended barrels that provide the coverage of $0.8 < |\eta| < 1.7$) and two end cap in the region of $1.5 < |\eta| < 3.2$. The barrel calorimeter uses iron as absorber material and scintillating tiles as active material while the end caps are liquid argon calorimeters.

The general features and physical requirements of hadronic calorimeters are the following:

- Rapidity coverage: because the main task of the hadronic calorimeters is the reconstruction of jets and the measurement of the event missing p_t , it has to extend to $\eta = 5$ (considering the hadronic modules of the forward calorimeters of which we will talk below) to allow an efficient tagging of forward jets associated to the production of heavy Higgs.
- Granularity: a granularity of 0.1×0.1 is needed for the decay $W \rightarrow jet, jet$ in the region of $\eta < 3$. In the region with higher η a granularity of 0.2×0.2 is enough.
- Energy resolution: generally speaking, the HEC has an energy resolution worse than the electromagnetic calorimeter one because the energy deposited has greater fluctuations due both to the effect of the electromagnetic component of the jet and to the presence of energy that cannot be detected as excitation, fission energy or as energy lost by neutrino emission. These factors lead to an energy resolution of

$$\frac{\Delta E}{E} = \frac{50\%}{\sqrt{E}} \oplus 3\% \quad \text{for } \eta < 3.0 \quad \text{for jets.} \quad (2.12)$$

- Total thickness: it has to provide good containment for hadronic showers; the total thickness is 11 interaction lengths at $\eta = 0$.

Forward Calorimeter

It is placed in the same wheel as the electromagnetic end cap, in the same cryostat as the EM calorimeter. It covers the range of $3.1 < |\eta| < 4.9$. It is a liquid argon calorimeter like the others but it has a different structure because it has tubular electrodes having a gap to allow liquid argon to flow inside them. The forward calorimeter is divided in three modules along the z axis: the first one is electromagnetic, the others are hadronic and they differ for the material choice (the first one is in copper, the others in tungsten). The FCAL has a granularity of 0.2×0.2 .

EM CALORIMETER	Barrel	End-cap	
Coverage	$ \eta < 1.475$	$1.375 < \eta < 3.2$	
Longitudinal segmentation	3 samplings	3 samplings	$1.5 < \eta < 2.5$ 2 samplings $1.375 < \eta < 1.5$ $2.5 < \eta < 3.2$
Granularity ($\Delta\eta \times \Delta\phi$)	0.003×0.1	0.025×0.1	$1.375 < \eta < 1.5$
Sampling 1		0.003×0.1	$1.5 < \eta < 1.8$
		0.004×0.1	$1.8 < \eta < 2.0$
		0.006×0.1	$2.0 < \eta < 2.5$
		0.1×0.1	$2.5 < \eta < 3.2$
Sampling 2	0.025×0.025	0.025×0.025	$1.375 < \eta < 2.5$
Sampling 3	0.05×0.025	0.1×0.1	$2.5 < \eta < 3.2$
		0.05×0.025	$1.5 < \eta < 2.5$
PRESAMPLER	Barrel	End-cap	
Coverage	$ \eta < 1.52$	$1.5 < \eta < 1.8$	
Longitudinal segmentation	1 sampling	1 sampling	
Granularity ($\Delta\eta \times \Delta\phi$)	0.025×0.1	0.025×0.1	
HADRONIC TILE	Barrel	Extended barrel	
Coverage	$ \eta < 1.0$	$0.8 < \eta < 1.7$	
Longitudinal segmentation	3 samplings	3 samplings	
Granularity ($\Delta\eta \times \Delta\phi$)	0.1×0.1 0.2×0.1	0.1×0.1	
Samplings 1 and 2		0.2×0.1	
Sampling 3		0.2×0.1	
HADRONIC LAr		End-cap	
Coverage		$1.5 < \eta < 3.2$	
Longitudinal segmentation		3 samplings	
Granularity ($\Delta\eta \times \Delta\phi$)		0.1×0.1	$1.5 < \eta < 2.5$
		0.2×0.2	$2.5 < \eta < 3.2$
FORWARD CALORIMETER		End-cap	
Coverage		$3.1 < \eta < 4.9$	
Longitudinal segmentation		3 samplings	
Granularity ($\Delta\eta \times \Delta\phi$)		-0.2×0.2	

Figure 2.10: Characteristics of the ATLAS calorimeters

2.2.4 Muon spectrometer.

Situated in the external part of ATLAS and arranged in a cylinder of internal radius of 5 meters and an external one of 10, the muon spectrometer [8] has to identify the muons produced in the interactions and to measure their energy and their tracks. It is very important in the study of the $H \rightarrow 4l$ because we could have muons among the final products. Its requirements are:

- wide coverage in η : this spectrometer is operating in the region of $|\eta| < 3$.
- high energy and transverse momentum resolution: very important for the reconstruction of Higgs mass in events with 2 or 4 leptons.
- spatial resolution in the coordinate perpendicular to the plane of the

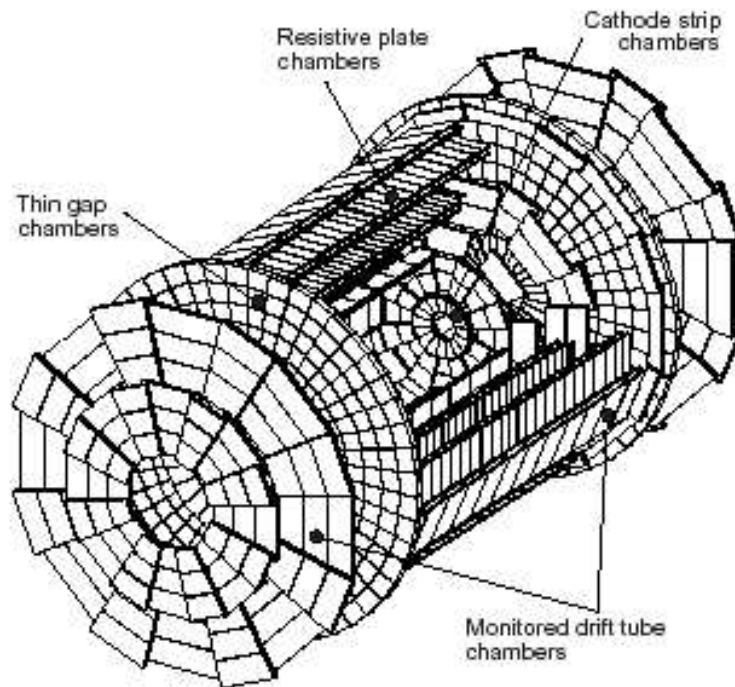


Figure 2.11: Muon chamber picture

track of the muon.

- temporal resolution of first level trigger lower than the bunch crossing interval.

We now briefly schematize his components structure.

Precision chambers: composed by Monitored Drift Tube chambers in the barrel region and by multi-wire chambers (more precisely, *Cathode Strips Chambers*) in the end cap. The MDT have a good spatial resolution while their temporal one is greater than the bunch crossing interval, so they are a good instrument for trajectory reconstruction but they have to be coupled to other instruments who can associate the muon to the event it belongs to. Instead the CSC have both good spatial and temporal resolution; for this reason they are used in the inner part of the end cap where the flux of particles is expected to be great.

Trigger chambers: they have a greater temporal resolution, so they are complementary to the Drift chambers. Without the trigger chambers it would be almost impossible to say to which event a muon belongs. The muon spectrometer is inside a magnetic field generated by toroidal magnets. In the region with $|\eta| < 1$ the field maximum value is 3.9 T while in the end cap one ($1.4 < |\eta| < 2.7$) it reaches a peak value of 4.1T. In the transition region the field is made up by a superposition of the two previous ones and is perpendicular to the muon trajectory.

2.2.5 Data acquisition and trigger system.

Because of its high luminosity and the incredibly high interaction frequency (40 MHz), it is of fundamental importance that ATLAS has very good systems for fast signal extraction, for selection of interesting events from the background and data storing.

The ATLAS acquisition and trigger system works on three levels in cascade and each one operates on the results given by the previous one. Its schematization is shown in Figure 2.12.

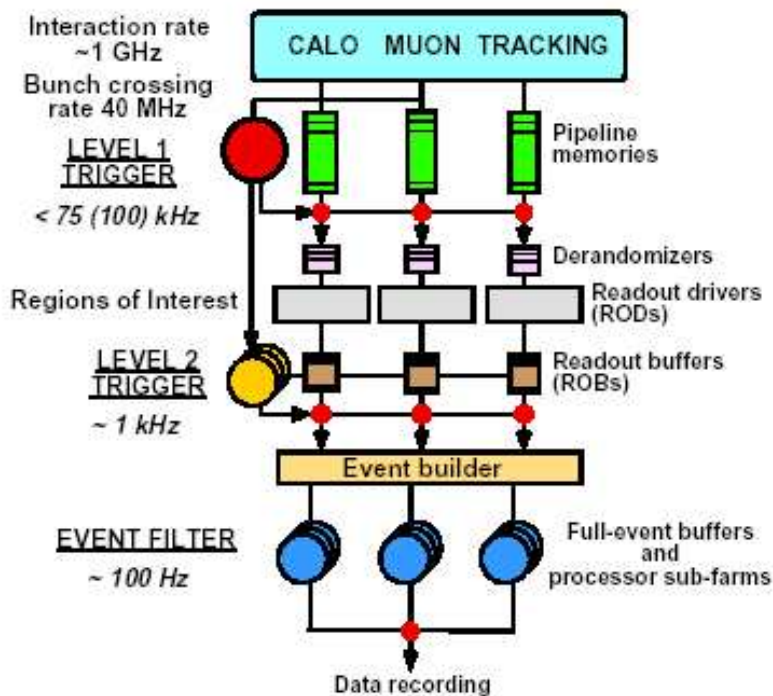


Figure 2.12: Trigger scheme

The first level trigger (LVL1) elaborates the data that come from the various subsystem of ATLAS in order to get a first scan in η and ϕ . It principally uses the signals from the trigger chambers of the muon spectrometer. Even in this first phase there is a search for photons and electrons with high p_T , at the calorimeter level. The time needed by LVL1 trigger to know whether to reject or to accept a signal has to be reduced as much as possible; the requirements are of intervals shorter than $2.5 \mu s$ and during this time the informations are stored in particular memories called *pipeline*.

By *Read Out Drivers* and *Read Out Buffer*, the informations of the accepted signal go to the LVL2 trigger. The *Read Out Buffer* stores the data while the LVL2 takes a decision about the signal: if it is kept, it goes to the Event Filter. The LVL2 trigger works in a different way with respect to the LVL1 trigger. While the latter get information from all the detector, the former uses only the data of the so called *Region of Interest* indicated by the LVL1. Upon this *RoI* the LVL2 makes a finer analysis.

If an event passes these two triggers, its signal goes to the *Event Filter* and then is ready to be stored and analyzed.

2.3 The electromagnetic End Cap calorimeter (EMEC)

Now we give some features of the electromagnetic end cap, because the study of its performance will be the main subject of this work.

As the barrel, the end cap calorimeter consists of accordion-shaped lead absorbers interleaved with electrodes and the gap filled with liquid argon. It has an external radius of 2077 mm and it is located in the end cap cryostat at a 3641 mm distance from the interaction points. It covers the pseudorapidity range $1.375 < |\eta| < 3.2$ for a full thickness ensured between 1.475 and 3.2. Actually, the EMEC is made up of two coaxial wheels (see Figure 2.13 and Figure 2.14), with a boundary at $\eta = 2.5$.

- The outer wheel contains 768 absorbers and 768 electrodes, while the inner wheel contains only 256 absorbers and electrodes.
- Each absorber of the inner wheel is aligned with an absorber in the outer wheel.
- The lead thickness of the absorber is 1.7 mm in the outer wheel and 2.2 in the inner wheel.

2.3. THE ELECTROMAGNETIC END CAP CALORIMETER (EMEC)29

In order to accommodate the accordion geometry in this region, the absorber plates are arranged radially like the spokes of a bicycle wheel and the accordion waves run parallel to the beam axis.

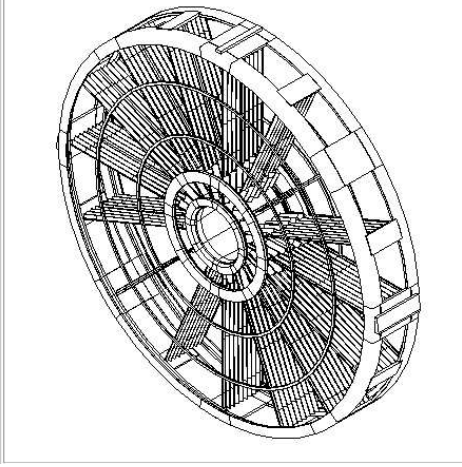


Figure 2.13: EMEC view. See the wheel-spoke-like distribution of the absorber plates.

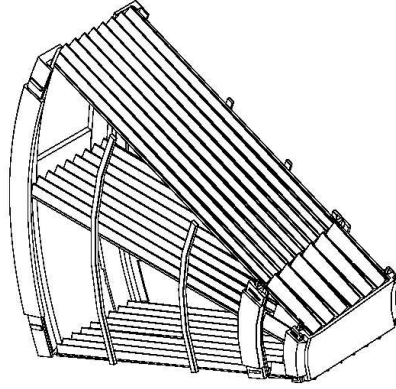


Figure 2.14: The ratio 1:3 between inner and outer wheel absorbers. Only 3 out of 96 absorber for the outer wheel are drawn.

To ensure a good azimuthal uniformity of the response, the combined thickness of liquid argon and absorbers crossed by the particles must be independent of the angle ϕ . Considering that the liquid argon gap increases with the radius, it is necessary to vary the height of the absorber waves and the folding angle as well. For technical reasons, the folding angle must be kept between 60 and 120 degrees and this limits the ratio of the external to internal radii of the absorbers to about three. So it is impossible to cover the pseudorapidity range with only one accordion structure; for this reason we need two coaxial wheels.

The η and z dependence of the gap width g and of the sampling fraction is shown in the Figure 2.15. The peak current of the calorimeter can be expressed as

$$I_{peak} = f_{samp}/g \cdot v_d. \quad (2.13)$$

For a given constant electric field and thus a constant drift velocity v_d , the dependences of f_{samp} and g with η almost cancel out, but for a better compensation of these two variables, that is to get a fully uniform response, one has to vary the electric field, by taking advantage that the drift velocity is a function of the electric field in the gap, varying as E^b , with $b \sim 0.3$, over a

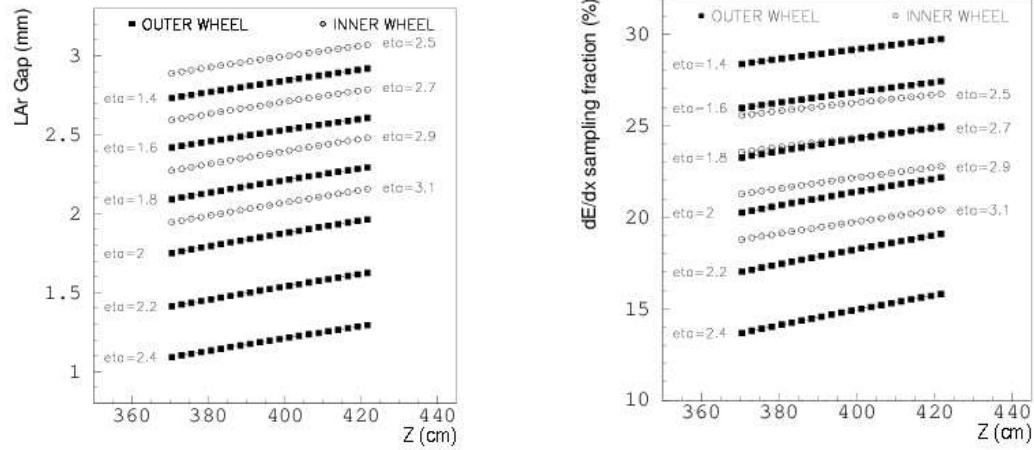


Figure 2.15: *Left*: liquid argon gap variation as a function of η and depth z . *Right*: Sampling fraction as a function of η and z in the end cap.

voltage range of 100 V/mm-1.2 kV/mm. Since E depends on the high voltage V as $E = V/g$, the expression for the peak current can also be written as

$$I_{peak} \propto \frac{f_{samp}}{g^{1.3}} \cdot V^{0.3} \quad (2.14)$$

To provide an eta-independent current to energy conversion factor one could use a continuously varying high voltage with η , but in practice a high voltage varying by steps will be used. Then, the reconstructed energy has to be corrected for each HV sector.

2.3.1 Absorbers and electrodes

The absorber are made of lead plates clad with two layers of stainless steel to ensure the absorber rigidity and smooth surface for high voltage. These are glued using a 0.15 mm thick glass fibre prepreg adhesive. The absorbers have nine waves in the outer wheel and six waves in the inner one.

To minimize the contribution of passive material to the constant term in the energy resolution, stringent tolerances on the lead plate thickness and liquid argon gap must be imposed: to get a contribution to the c term of energy resolution not bigger than 0.3%, the distribution of the absorbers thickness must have a rms lower than $17\mu m$ for the outer wheel and $22\mu m$ for the inner wheel.

The readout electrodes are flexible printed circuit boards folded with the same geometry as the absorbers. They consist of three layers of copper ,

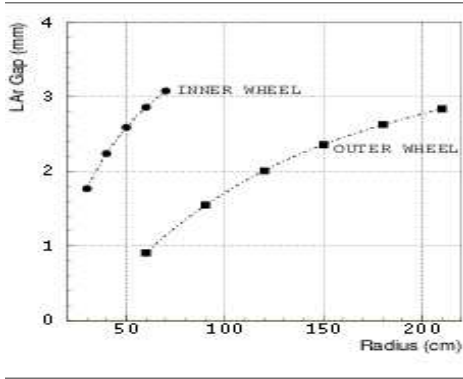


Figure 2.16: Liquid argon gap variation as a function of the radius.

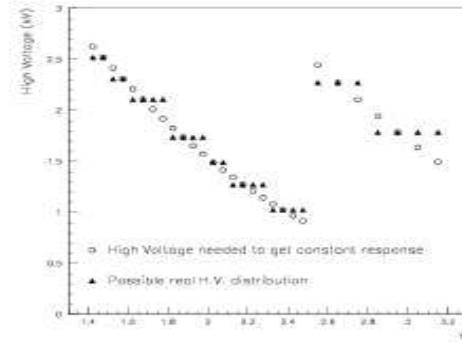


Figure 2.17: compensating high voltage in EMEC as a function of η , in the outer (left) and the inner (right) wheel; continuously varying high voltage (open symbols) and nominal high voltage (closed symbol).

insulated by two Kapton polyimide sheets: the external ones provide the high voltage to the liquid argon gap necessary to collect the charges, the internal one allow signal collection by capacitive coupling. Resistive ink pads have been used to minimize the crosstalk effect and to distribute the High Voltage over the electrodes, that is to minimize the fact that a cell could influence a neighbour one by inductive effects.

2.3.2 Energy measurement.

In general, the energy reconstructed in all the EM calorimeters can be written in the following simple way:

$$E = w_{glob}(w_{ps}E_{ps} + E_{str} + E_{mid} + E_{back}) \quad (2.15)$$

where w_{glob} is a global calibration factor and E_{ps} , E_{str} , E_{mid} and E_{back} are the energies measured in a given cluster of cells in the presampler, strip section, middle and back sampling of the calorimeter. The weight w_{ps} is chosen to minimize the energy resolution. While in the barrel part of the EM we do not have to apply any weight to the energy deposited in a given longitudinal compartment (because the sampling fraction and the liquid argon gap are constant), in the end cap, where the sampling fraction and the thickness

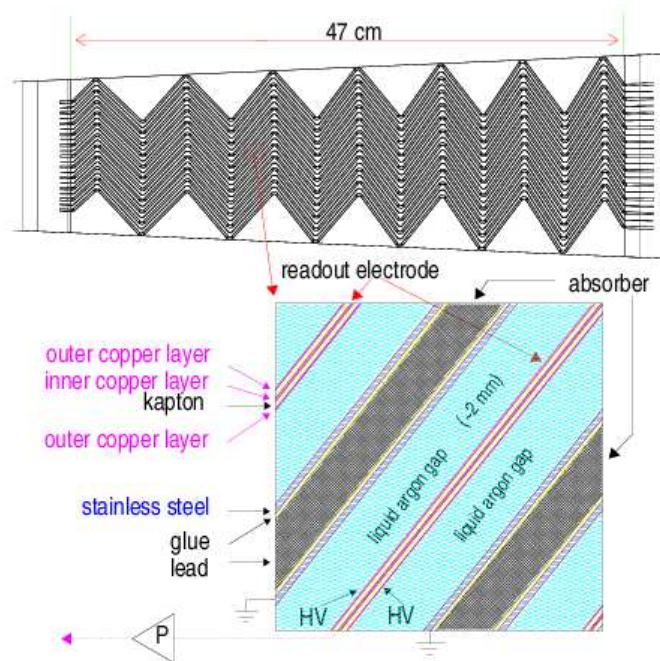


Figure 2.18: Structure of the barrel calorimeter gap, absorber and electrodes. The end cap structure is the same.

of the gap grow with the radius, in theory we should add proper weights. However, it has been found that with the adopted longitudinal segmentation the optimum weights are close to unity.

Detailed studies in the case of the barrel have shown that Formula 2.15 has to be modified somewhat to optimize linearity and resolution.

The energy response of the calorimetry is potentially affected by the following effects:

- upstream energy losses;
- ϕ -modulation and azimuthal gaps between presamplers sectors;
- lateral leakage outside the cluster;
- longitudinal leakage behind the EM calorimeter.

Efficient corrections can be applied for most of these effects, which allow to preserve a good energy resolution.

Formula (2.15), as we said, is a very general one; in fact, in the end cap things are slightly different. The presampler is present only in the region

$1.5 < |\eta| < 1.8$ to improve the energy measurement in the barrel-end cap transition, where the material in front of the calorimeter is the largest and for the inner wheel the reconstructed energy is reduced to the sum of E_{mid} and E_{back} .

2.3.3 Granularity

As we have seen in Table (2.10), the granularity of the EMEC outer wheel is very similar to the barrel's one. The inner wheel has instead a much coarser granularity, because its main goal is not the spatial resolution but coverage at high η to improve the measurement of the missing energy of the events.

The two coaxial wheels differ also for the number of the samplings: while the outer wheel has three samplings, the inner wheel does not have the front one.

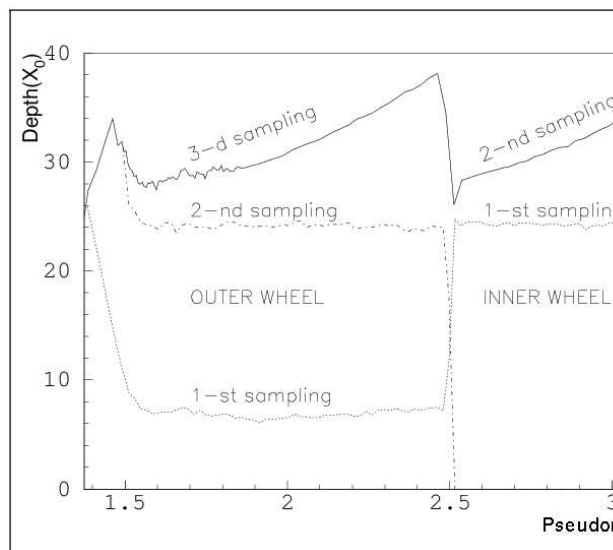


Figure 2.19: Total thickness (in radiation length) up to the end of the first, second and third sampling.

2.4 Test Beam

2.4.1 Test Beam Setup

In the Test Beam of 2004 1/8 of the EMEC inner wheel was placed in a cryostat with a pre-sampler and two modules of the HEC. The cryostat was

filled with liquid argon at a temperature of 89.9 K.

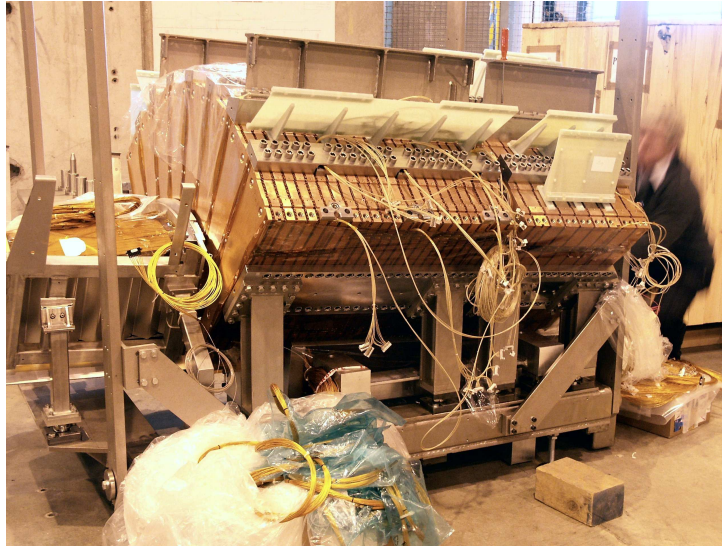


Figure 2.20: View of the EMEC module (the small one) and the HEC module.

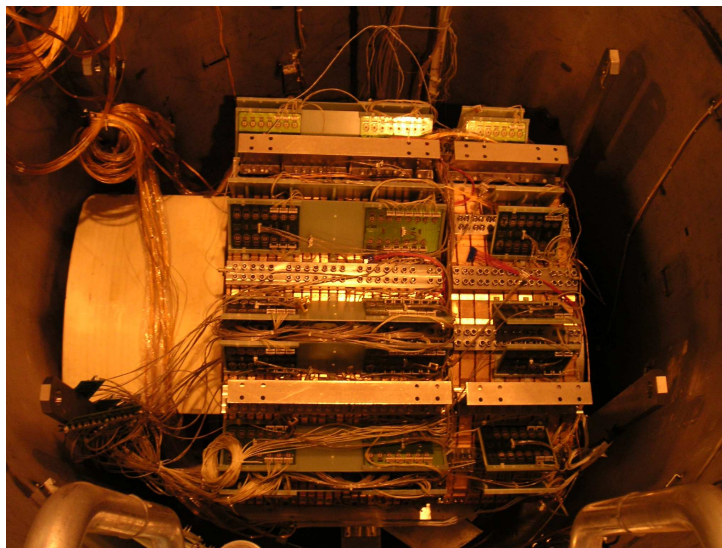


Figure 2.21: EMEC and HEC modules inside the cryostat.

In Figure 2.22 we can see the complete setup of the best beam with all the sub-detectors used to provide a trigger signal and to track the beam particles.

To study different impact points on the calorimeter modules, the cryostat was mounted on rails that allow it to move vertically and horizontally. The Multi Wire Proportional Chambers (MWPC) placed along the beam are used to extract the particles tracks and help in the the determination of the exact impact point on the detector. To reduce the dead material in front of the

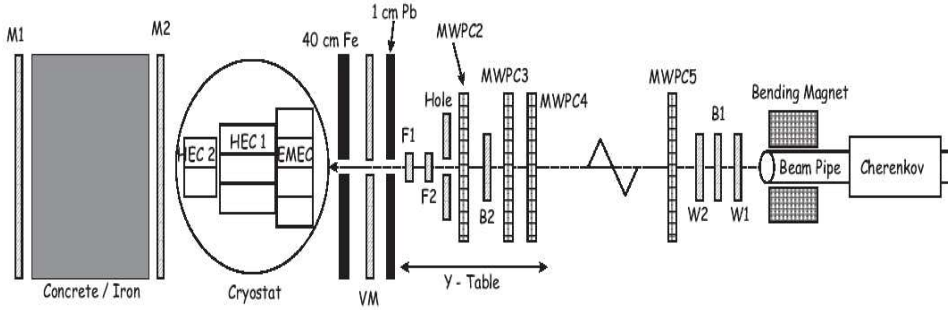


Figure 2.22: Schematics of Test Beam Setup

calorimeter, the cryostat has a circular window of 60 cm diameter with a reduced wall thickness and the liquid argon in front of the calorimeter was excluded by a low density foam excluder. The effect of dead material in front of the calorimeter has been studied by placing absorber plates of different thickness in front of the cryostat for some runs.

The Test Beam was performed in the H6 beamline at CERN North Area, using the Super-Proton-Synchrotron (SPS); 450 GeV proton beams are produced and directed on a common production target for the secondary beams of the H6 and H8 beamline. Here electrons are separated from pions by their synchrotron radiation energy loss in a bending magnet. The beam momentum spread of the H6 beam is typically $\delta p/p \sim 0.3\%$ and so it is negligible if compared to the resolution of the calorimeter.

2.4.2 Trigger System

The read-out of the detector was triggered with the help of several trigger counters installed along the beam line as was sketched on Figure 2.22. F1 and F2 are fast scintillation bars with a time resolution of 70 ps. They are oriented perpendicular to one another and define the transverse size of the beam.

VM and HOLE are scintillating counters used to veto events in which particles from the beam halo arrived at the same time as pre-trigger signal. Moreover, events that occurred too close in time were not recorded to prevent pile-up phenomena.

The trigger for muons required in addition a signal in the planar arrays of scintillation detectors M1 and M2 behind the cryostat and an additional iron wall.

2.4.3 Read Out Electronics

The charge generated by a ionizing particle that crosses the active region of the calorimeter is collected by the High Voltage applied between electrode and absorber. The signal that we get has a triangular shape. Considering that the mobility of the electrons in the liquid argon is much higher than that of the ions, the signal is generated by the former.

The ATLAS calorimetry does not have an internal gain, so the measured signal is directly proportional to the collected charge. This signal has a very steep rise (it lasts about 1 ns) and a linear decrease of about 450 ns, equal to the drift time T_D of the electron inside the liquid argon gap.

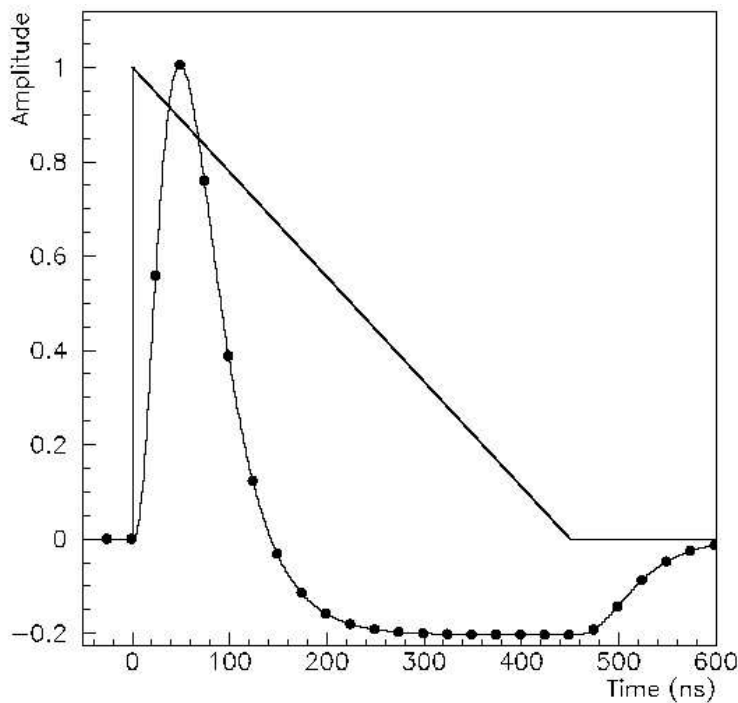


Figure 2.23: Signal before and after the shaping. On the shaped signal a 25 ns sampling has been drawn.

The signal generated in a liquid argon gap is read by the electrodes and sent to the *Summing Board*, where the signals of the electrodes belonging to

the same read-out channel are summed: each Summing Board is linked to eight electrodes, thus covering $\Delta\phi \sim 0.2$ (two cells in ϕ).

The Summing Board are grouped in a 2×2 scheme by the *Mother Board*. The signal is then sent from the Mother Board to the read out electronics situated outside the cryostat. In the read-out electronics there is a pre-amplifier that amplifies the signal and convert the current to voltage. The amplified signal is then elaborated by a multi-gain shaper $CR - RC^2$ with a time constant of $\tau \sim 13$ ns that minimise the signal-noise ratio. Has been chosen such a shaper to get a shaped signal of zero global area, because that allows to treat the pile-up phenomena as a noise contribution to the physical events.

The shaped signal is sampled each 25 ns, that is at the bunch-crossing frequency of LHC and then it is stored in analogic memories waiting for the decision taken by the LVL1 trigger. If that signal is considered an interesting one, it will be amplified using one of the possible gain (LOW, MEDIUM, HIGH) and five points of its positive part are digitised and stored.

Considering that only 5 samples will be kept, of fundamental importance will be the methods that allow a precise energy reconstruction. The most important methods are the *Parabola method* and the *Optimal filtering method*; they are briefly described in Appendix A. Here we can outline the typical procedure of energy reconstruction:

- Calculation of the pedestal, that is, the base ADC level for zero input.
- Subtraction of the pedestal from all the signal time samples.
- Calculation of amplitude and time position for each event using either a cubic interpolation, the parabola method or the optimal filtering method. We have to remark that the parabola and the cubic interpolation are simple methods that do not require the knowledge of the signal shape but introduce some systematic errors (see Appendix A).
- Conversion of the ADC counts values to nA and GeV using the calibration coefficients (see section 2.4.4).

2.4.4 Electronic calibration

The calibration of the electronic chain ([9], [25]) has the following purposes:

- Obtain a relation between the ADC counts and the ionization current.
- Determine the signal shape and the noise autocorrelation function of each channel for the signal reconstruction using the method of optimal filtering.

- Measure the inter channel cross-talk.

The hardware calibration system allows to inject a known current pulse to the electrodes of each calibration line. The charge can be injected in only one calibration line or in all channels at the same time. From the difference in response of these two modes the inter channel cross-talk can be evaluated.

Detailed analysis of the calibration signal are beyond the goal of this thesis, so we briefly explained the steps that has to be followed.

- First of all charge pulse of different (but known) size are injected in every channel. Actually the calibration signals are not directly injected in the read-out electrodes, contrarily to the physics signal and one has to take in account of this difference in the calibration pulse shape reconstruction.
- Finally one has to fit with a cubic polynomial the relation between the current I and the amplitude of the triangular pulse shape, deduced from the calibration signal, above the pedestal:

$$I[nA] = \sum_{i=0}^3 p_i \cdot A[ADCcounts] \quad (2.16)$$

In general the coefficients p_2 and p_3 are compatible with zero, while in the p_0 one there is the constant offset between the set current and the real injected current: it is not used to convert the amplitude of physics signals from ADC to the corresponding current.

Chapter 3

HV-Energy curve and Signal Shape

3.1 HV-Energy Curve

The first goal of this work is to test the performance of the EMEC, analyzing the results of the combined test beam (CBT) of autumn 2004. At the beginning we paid particular attention to the signal shape after the shapers and to the HV-Energy curve to test its universality, that is, to check if really it has the same behaviour all over the electromagnetic calorimeter. Specially this second point has brought interesting results and it could also be important for an evaluation of corrections that will have to be made when the HV nominal value cannot be applied.

For this part we have taken inspiration from the analogous work on the barrel calorimeter described in [10].

In Figure 3.1 we can see a view of the inner wheel of the EMEC and the HEC placed behind. We have used runs with the beam that hits the EMEC in the two points we have circled, belonging to two different HV sectors.

All the runs have almost the same characteristics about the number of events and the number of samples for each event, with the exception of the nominal HV value one in the HV sector at higher η (closest to the beam pipe) of the inner wheel, which has much more events: for this reason we will usually use this one in our analysis.

3.1.1 Determination of the electron energy peak

The first step is the calculation of the electron energy peak value; if we use the nominal HV run, the electronic peak we get from the distribution of the energy of all events will give the real energy of the electrons of the beam.

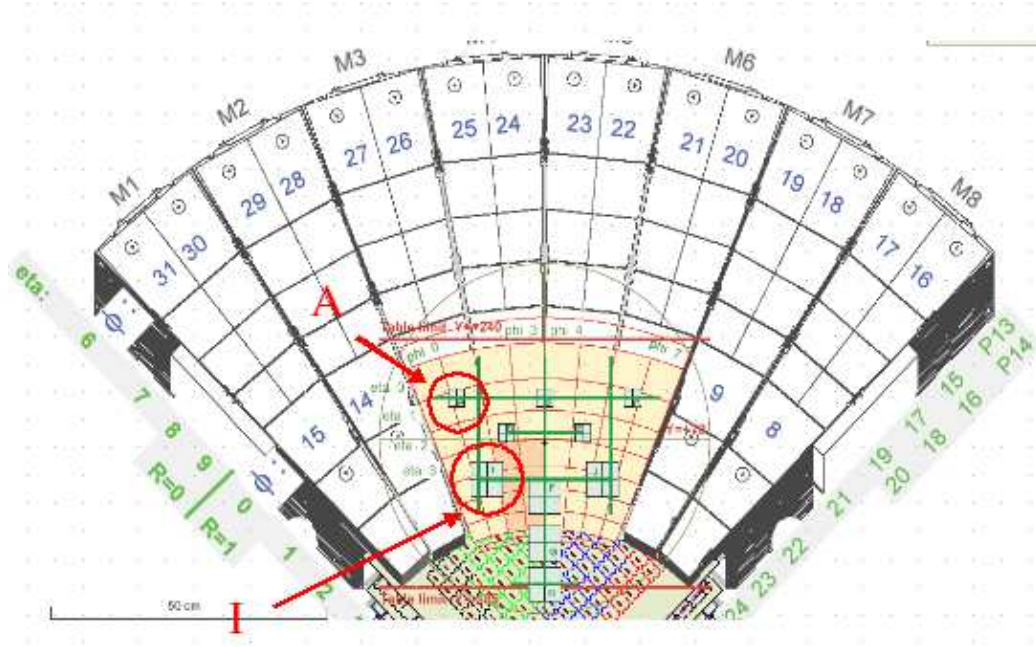


Figure 3.1: EMEC inner wheel front view, with the HEC behind. The point A belongs to the HV sector at $2.5 < \eta < 2.8$, the point I to the other ($2.8 < \eta < 3.2$).

The energy of each event has been calculated using a 3 by 3 cells cluster around the barycenter cell, in order to minimize the influence of the noise that dominates the output of the cells far from the ones where the beam is pointed: that is, for each event we have calculated the barycenter cell using the value of the energy released in each cell, and then we have taken the eight cells that surround it and then the barycentre of such a cluster. η and ϕ barycenters are calculated in S_2 in the following way [11]:

$$\begin{aligned} \eta_{bar}^{S_2} &= \sum_{j=1}^{N_j} \sum_{k=1}^{N_k} \frac{E_2(\eta_j, \phi_k) \times \eta_j}{E_{S_2}} \\ \phi_{bar}^{S_2} &= \sum_{j=1}^{N_j} \sum_{k=1}^{N_k} \frac{E_2(\eta_j, \phi_k) \times \phi_k}{E_{S_2}} \end{aligned} \quad (3.1)$$

We take in account only nine cells in the calculation of the energy because of the cells dimension: as we said in the EMEC description, their sizes are quite big (0.1 in η and ϕ), so it is reasonable to think that all the particle energy is contained in this cluster. But if we do not impose a cut on the energy value of the cells, when we perform the calculation of the barycenter,

there will be plotted even events that release only few MeV in the EMEC, that is, events relative to pions and muons.

Effectively, without energy cut in the barycenter calculation, we get a very bad energy spectrum and in the 2-dimensional plot with the EMEC energy versus the HEC one we can understand the reason (Figure 3.2): our beam is very polluted with μ and π that we can easily detect. In fact the muons do not deposit energy in the calorimeters while the pions leave in the HEC almost the totality of their energy.

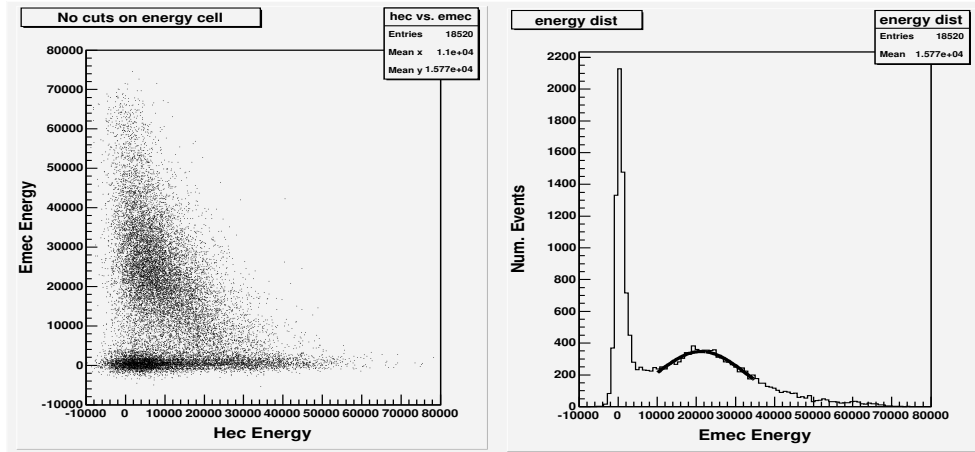


Figure 3.2: No cut applied on energy cell. *Left*: HEC energy Vs. EMEC energy. *Right*: EMEC Energy distribution.

We can see that the electron peak has not a great energy, it is only slightly greater than $20 GeV$, so we were forced to keep the energy cut quite low: to keep an event there has to be at least a cell with a deposited energy greater than $1 GeV$. Using such a cut (Figure 3.3), things get better but the gaussian fit of the electron peak has still a great σ .

3.1.2 Cleaning of the beam

Because of such low energy and polluted beam, for any sort of analysis, becomes of fundamental importance its cleaning by appropriated cuts. The first two cuts we carried out are the ones on the S2 scintillator and specially on the Halo scintillator:

- Since the Halo scintillator tells wether the particle is well inside the cryostat window or not, high Halo values mean that they are not com-

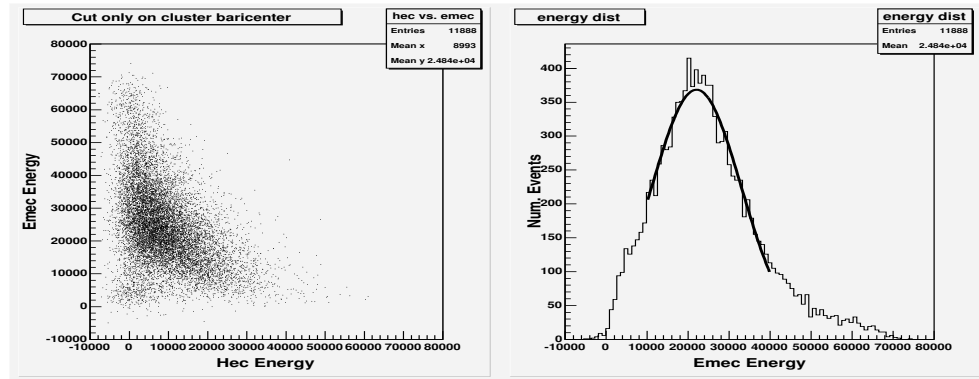


Figure 3.3: Cut on energy cell: at least one cell of the cluster has to have more than 1 GeV. *Left*: HEC energy Vs. EMEC energy. *Right*: Energy distribution.

pletely inside that window and so they lose some energy before being analyzed; for this reason we reject these events.

- The values measured S2 are the energies that each events deposit in this small scintillator. When the energy deposited is high, this can be interpreted as the passage of two particles at a time.

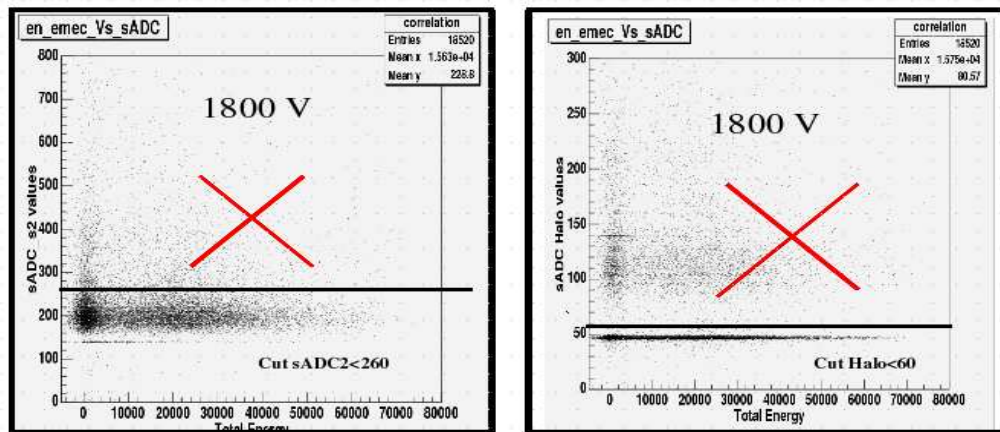


Figure 3.4: Left: cut on the sADC_{s2}. Right: cut on the Halo scintillator values.

These two cuts reduce the number of the events and slightly improve the spectrum but not yet to an acceptable level (Figure 3.5).

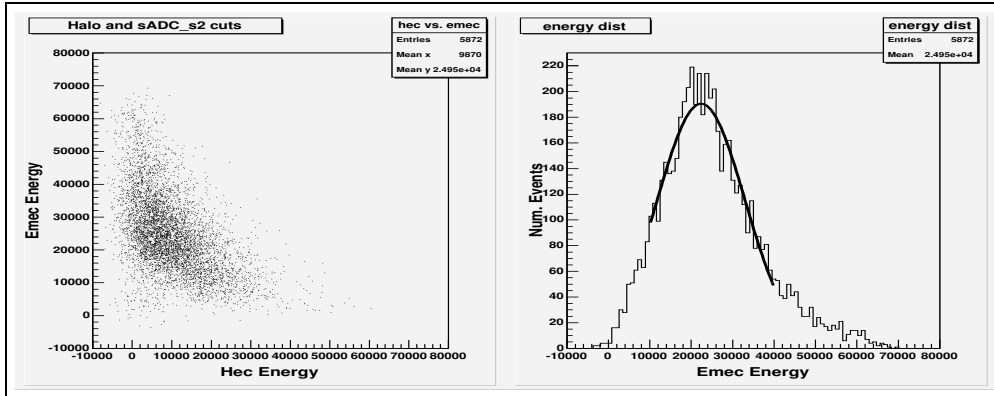


Figure 3.5: EMEC energy Vs. HEC energy and Energy distribution after Halo cut.

Finally, to get rid of all pions and muons, we decide to apply a further and more violent cut: reject all the events with an EMEC released energy smaller than an HEC released one. More precisely we choose to keep only the events for which the EMEC energy is greater than $6/5$ the HEC energy: the choice of this factor comes from the fact that it is a good mediation between the background reduction and the preservation of good statistics. After this cut we get the spectrum in Figure 3.6: now we can begin our analysis.

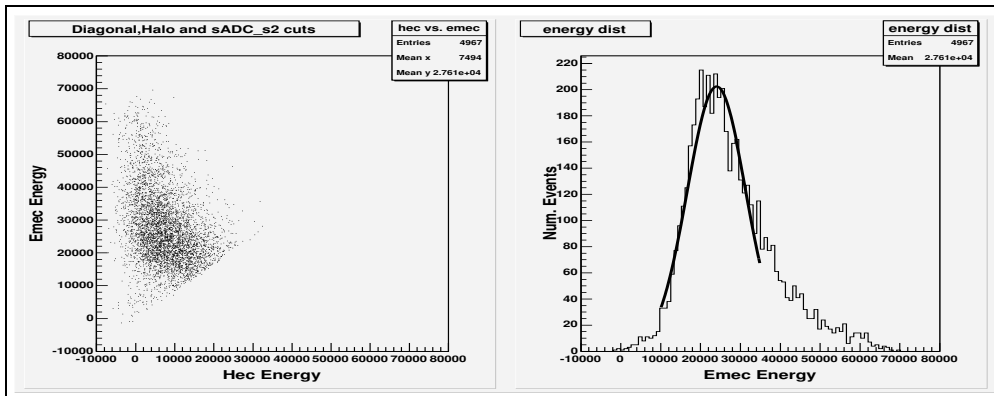


Figure 3.6: EMEC energy Vs. HEC energy and Energy distribution after all the cuts.

	Mean value	Error	σ
No cuts	$2.12 \cdot 10^4$	$2.25 \cdot 10^2$	$1.13 \cdot 10^4$
Barycenter cut	$2.18 \cdot 10^4$	$1.76 \cdot 10^2$	$1.02 \cdot 10^4$
Halo cuts	$2.21 \cdot 10^4$	$2.25 \cdot 10^2$	$9.8 \cdot 10^3$
Diagonal cut	$2.40 \cdot 10^4$	$1.68 \cdot 10^2$	$7.3 \cdot 10^3$

Table 3.1: How the mean values and the σ change adding more cuts

3.1.3 Fitting the HV-Energy curve

We apply the same cleaning procedure to all the other runs and for each of them we fit their peaks using a gaussian fit function and plot the mean values and the errors that it gives us. Following [10] we try to fit this graph using a power function of the sort of

$$E = a \cdot HV^b \quad (3.2)$$

keeping, for the moment, the runs of the upper side separated from the lower side ones because they belong to different HV sectors. We begin by fitting the lower side runs just because their number is greater and we obtain the values on the plot in Figure 3.7.

If this curve depended only on the property of the liquid argon, we should get, even for the runs in the upper side, a reasonable fit using the same exponent b and fitting only factor a , as shown in Figure 3.8. The result is not bad and we superposed the two graphs making a rescaling of the second: since a is proportional to the sampling fraction (see [12]) that in the EMEC strongly depends on the radius r , we multiply each point of Figure 3.8 by the ratio a/a' .

The result in Figure 3.9 is quite satisfactory but there are facts that lead us to think that it could be improved if we do not consider the runs at 50 V. These facts are:

- at such a low HV , the number of events that passes all the cuts applied on beam instrumentation is very small, so we do not get a satisfactory statistics.
- we see that while all the points are above the fit, the 50 V one is well below (see Figure 3.8).
- if we perform the calculation of the ratio between the theoretical value ($a \cdot HV^b$ with a and b from the fit of Figure 3.7) and the measured value, we should obtain an almost constant value, if our hypothesis of

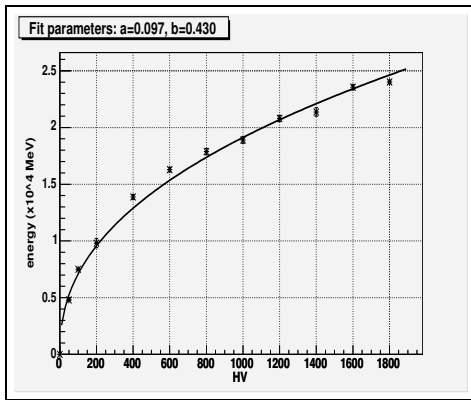


Figure 3.7: Fit of lower side runs.

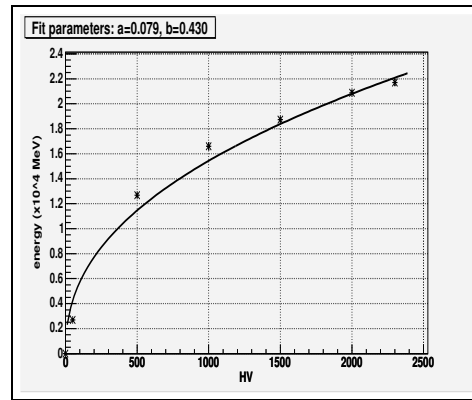
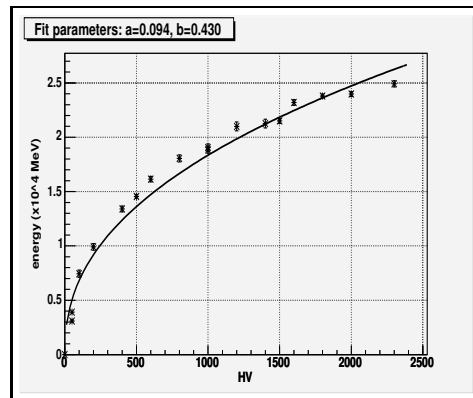
Figure 3.8: Fit lower side runs with the same exponent b get from the lower side ones.

Figure 3.9: HV-Energy curve after the rescaling of the upper side runs.

universality was correct. As we see in Figure 3.10, this is true for all the points with the exception of the 50 V one.

The points at 50 V are not very reliable on account of the very low HV applied: we decided to remove it from the fit and actually the fit parameters we get change considerably (Figure 3.11 to Figure 3.13)

Finally we consider only the runs with a $HV \geq 400$ V, to have runs with a quite high HV and a greater statistics: we can note that the exponent b becomes still lower and the point at 2300 V, that in Figure 3.13 was quite far from the fit, is better fitted (see Figure 3.14 and Figure 3.15).

We can conclude that, with the exception of the run at 50 V, the behaviour

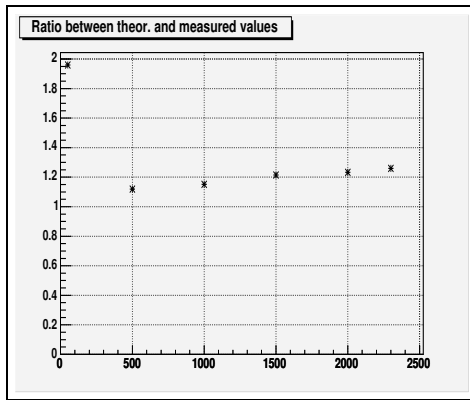


Figure 3.10: Ratio between theoretical and observed values.

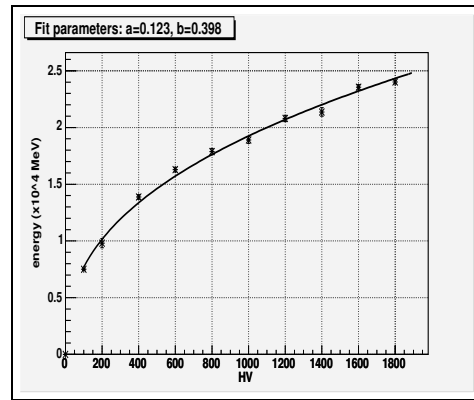


Figure 3.11: Fit without the 50 V run.

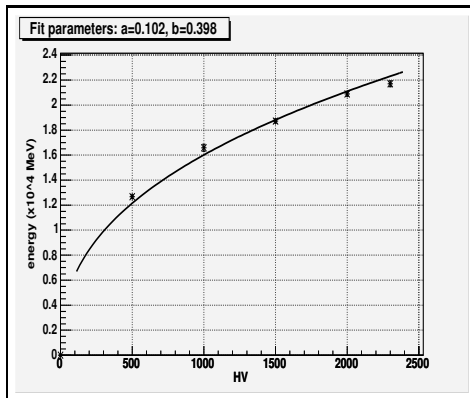


Figure 3.12: Ratio between theoretical and observed values.

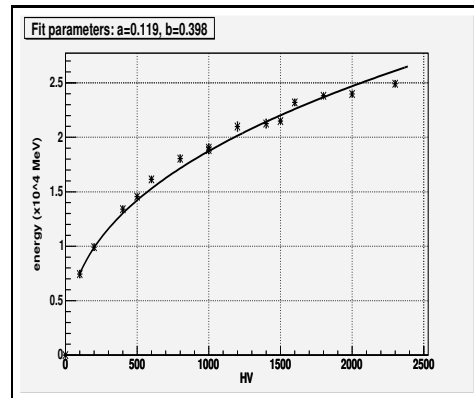


Figure 3.13: Fit without the 50 V run.

of the curve corresponds to the one expected, with exponent values very close to those we can find in [10].

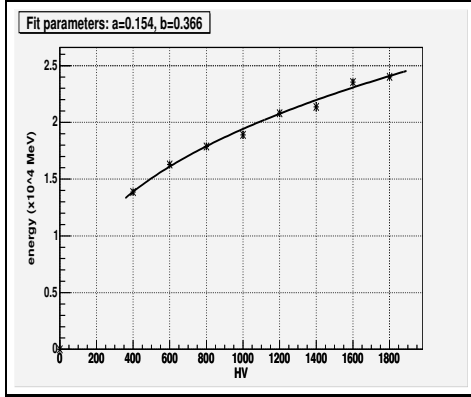


Figure 3.14: HV-Energy curve with $HV > 400$ for point I runs.

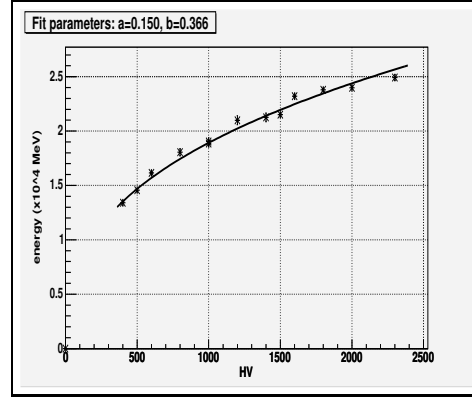


Figure 3.15: HV-Energy curve keeping only the runs with $HV > 400$.

	Our results			L. di Ciaccio results	
	a	b		a	b
All runs	0.094	0.430	100 GeV beam	8.7	0.44
Without 50V	0.119	0.398	245 GeV beam	13.9	0.37
$HV > 400V$	0.150	0.366			

Table 3.2: Comparison between our values and those found in [10].

3.2 Signal shapes

Studying the signal shapes, their evolution comparing them to the theoretical shapes is another important introductory study. The function that describes the theoretical shapes could be found in [17].

Below same shapes with different drift time parameters are drawn (see Figure 3.16), in order to observe how the curves change when we modify the drift time: in fact our goal is to study how they change with different HV values, that are linked to the drift time by

$$\frac{T_{drift,1}}{T_{drift,2}} = \left(\frac{HV_1}{HV_2} \right)^b \quad (3.3)$$

The CBT signals in Figure 3.16 are in fact a mean on the 18500 events of the shape of the single events: we accumulated the values of the single bins and then we have normalized them dividing by the number of events to get a

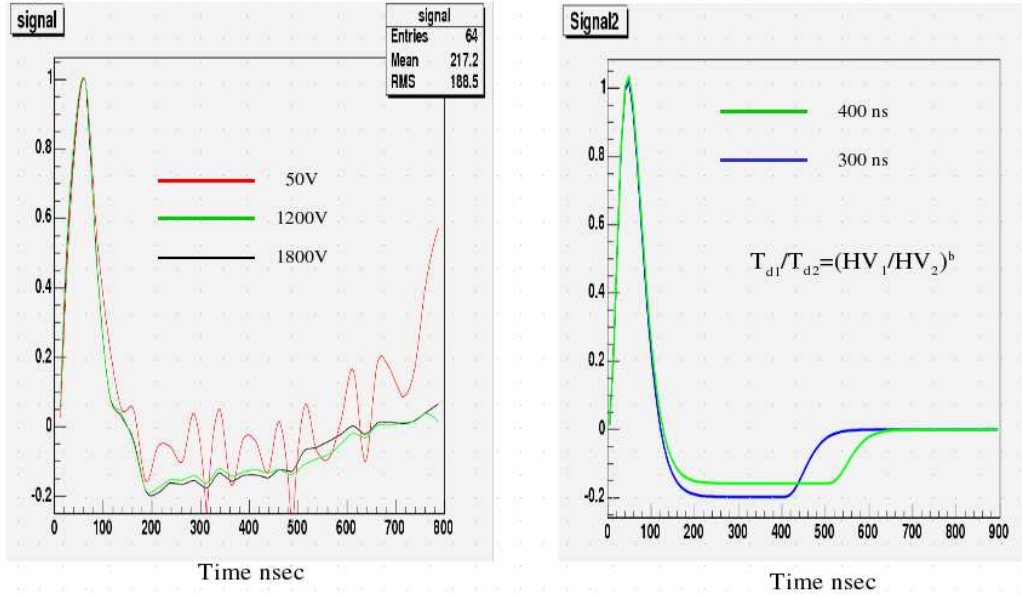


Figure 3.16: *Left*: signal shapes obtained from the CTB data. The fluctuation in the 50 HV curve are essentially due to a normalization effect: for this run the ratio between signal and noise is worse and normalizing the curve this fact is amplified *Right*: theoretical signal shapes.

more uniform signal. Anyway if we compare them to the theoretical signals it is easy to note the substantial differences, even only from a qualitative point of view: the undershoot is not flat and there is not a steep rise after it, it is very smooth and it is not well distinguished from the undershoot [13]. Moreover, we observe that the relation between drift time and HV is not exactly respected: if we consider the runs at 1800V and at 100V, for relation 3.3 we should have drift time differences of the order of 20%. Instead, looking at Figure 3.17, we see effectively a correlation between those two variables but the time difference we obtained for the same runs is the 10%.

We have made some hypotheses about the strange behaviour of the undershoot and about the fact that there is not a perfect correlation between drift time and high voltage.

- First we have thought about recombination effects of the charges produced in the liquid argon: these effects could make smoother the rise to zero of the signal. However, as can we see in [14], they influence only the 5% of the produced charge and the proper time of this effect is of the order of milliseconds while the sampling is effectuated every

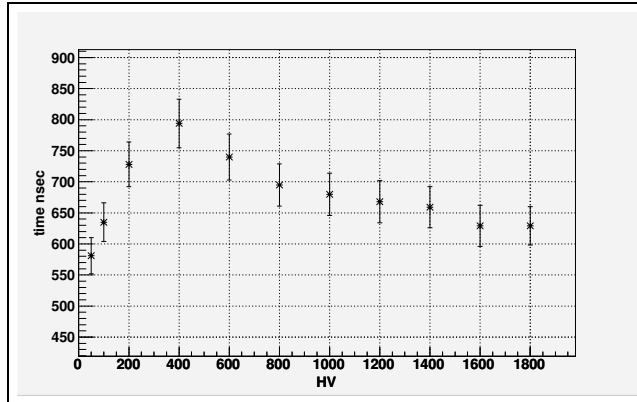


Figure 3.17: Time of second passage of the signal shape across zero (drift time crude estimate) Vs. high voltage

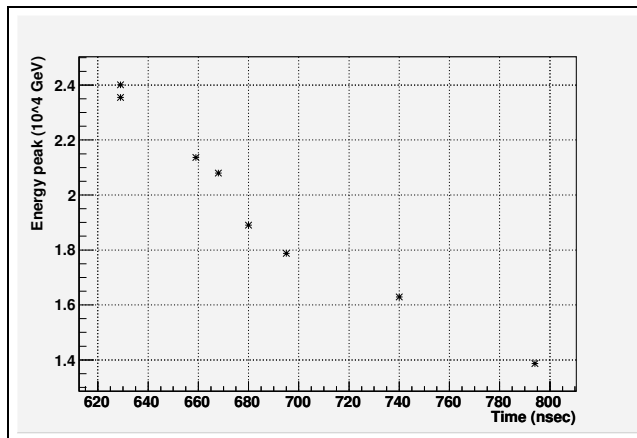


Figure 3.18: Time of second passage of the signal shape across zero (drift time crude estimate) Vs. peak energy

25 nanoseconds.

- Other hypotheses could be the pollution of the liquid argon and the non-uniformity of the absorber thickness (and so of the liquid argon gap). But levels of liquid argon pollution in the test beam have been kept below the value at which they could influence the signal.

Then the most probable explication becomes the accordion geometry of the electrodes and absorbers. In the regions of the folding angles the distance between the two absorbers is greater so the particles are exposed to a weaker

electric field. The ionization curve in Figure 2.23, that in principle should be triangular, will be an interpolation of triangular curves with different drift times and different peak amplitudes: this fact will give a resulting exponential-like curve that after the shaping will have a not flat undershoot (see Figure 3.19 and Figure 3.20).

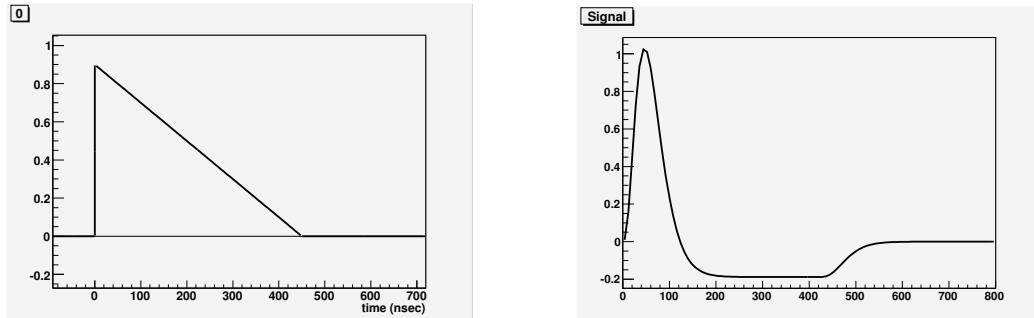


Figure 3.19: *Left*: Theoretical ionization curve that we would find if the distance between the electrodes were constant. *Right*: Signal shape after $CR - RC^2$ shaping.

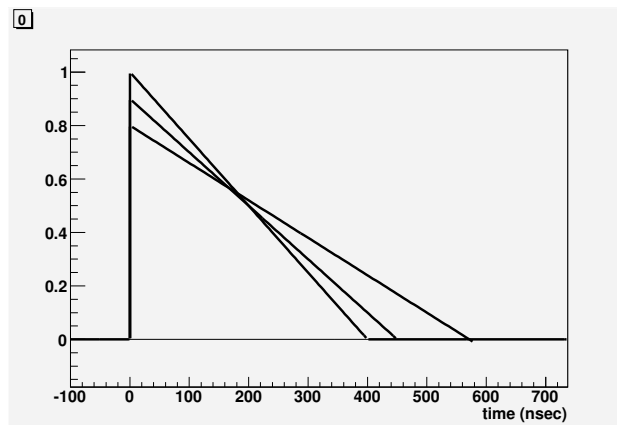


Figure 3.20: Superposition of ionization curves that correspond to different distance between electrodes. After the $RC - CR^2$ shaping we obtain the actual signals of Figure 3.16 on the left.

In the EM barrel, which is the part of the calorimeter that should perform the more precise measures, this effect has been studied and taken into account. For the EMEC a similar study has not been performed yet, so we give only this qualitative explication.

Chapter 4

Noise

In this chapter we will do a brief analysis of the EMEC electronic noise to quantify how much it can influence the measurements of physical events. To do this we have used one r -tuple containing only random events.

The first goal was to check if the electronic noise was purely gaussian, that is, characterized only by statistical fluctuations, or if it had particular behaviours; we also compared the noise with that of older test beam data.

4.1 Noise measurement

If the noise was purely gaussian, we should find out that the *RMS* of the distribution of the means of the 32 sample we had for each event is equal to the mean of the distribution of the *RMS* for each event, divided by the square root of the number of samples [22].

$$\frac{\sum_{i=1}^{i=N} (y_i - \bar{y})^2}{\sqrt{N}} = \frac{\sum_{i=1}^{i=N} \left(\sum_{j=1}^{j=32} (x_{i,j} - \bar{x}_i)^2 \right) / \sqrt{32}}{N} \quad \text{with } y_i = \sum_{j=0}^{j=32} x_{j,i} \quad (4.1)$$

For each cell of layer 1 we obtained the values of RMS plotted in Figure 4.1, keeping in mind that the 0 in the η axis correspond to the η physical value of 2.5 and 7 correspond to 3.2.

From Figure 4.1 we can immediately see some particular characteristics:

- In the up-left plot (that display the means of the RMS distributions) we see that the noise values rise with η , that is, the noise grows when we approach the beam axis.
- In the up-left plot the cell with $\phi = 25, 26$ have a noise much bigger than the other cells' one.

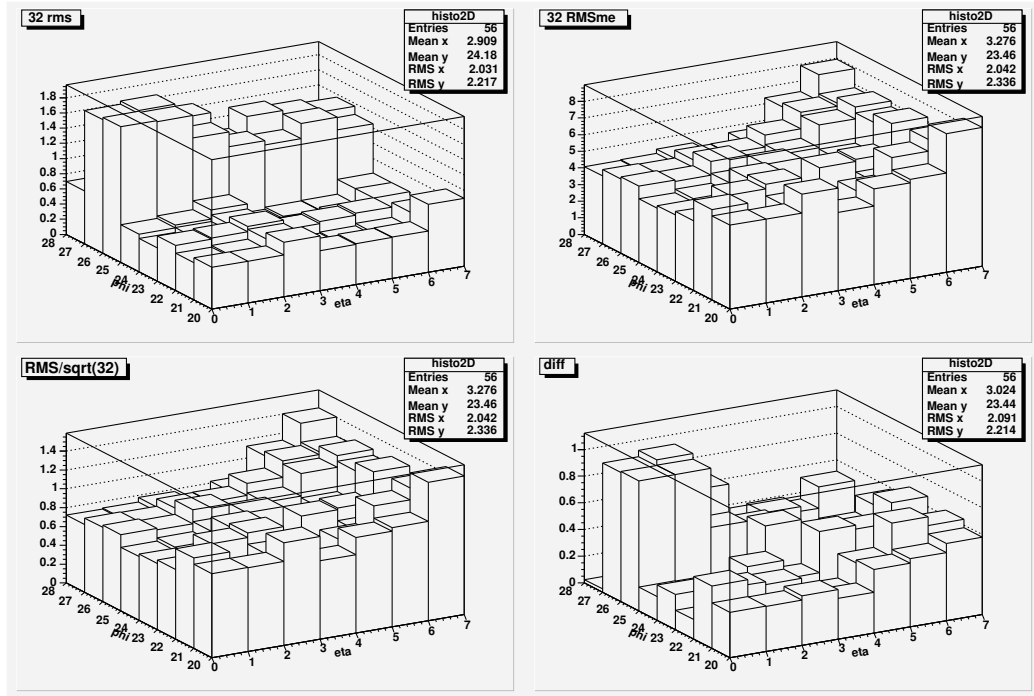


Figure 4.1: *Up-left*: RMS of the distribution of the means over 32 samples. *Up-right*: means of the distribution of the RMS calculated event by event. *Down-left*: same values as up-right but divided by $\sqrt{32}$. *Down-right*: difference between *Up-left* and *down-left*.

- The difference we are interested in is especially marked in four cells, those with $\eta = 0, 1$ and $\phi = 25, 26$

The η variation, anyway, is not too worrying, is very smooth and not too much accentuated. Instead the ϕ variation deserves more attention: it is an abrupt change and it is limited to only two cells lines. We have to develop further analysis to understand this strange pattern that differs from the gaussian expected one. To check this strange behaviour of the right side of our detector, we had repeated this analysis for the other layer and actually we get the same pattern and even with an other run the plot does not change, indicating that this feature is constantly present.

The origin of the high noise in the row with $\phi = 25, 26$ could be due to some electronic device that does not work properly, as summing board, HV board or mother board. To test this hypothesis we looked at some photos that have been taken of the inner wheel during the test beam, photos that shows how the different devices were arranged on the absorbers. In particular we can see from the Figure 4.2 that each summing board covers a region of

two cells in ϕ , with 4 summing board to cover all the ϕ coordinate: that means that the $\phi = 25, 26$ lines are not served by the same summing board and this decreases the possibility of a high RMS due to such a device that does not work well. We have also noted that even the HV boards have

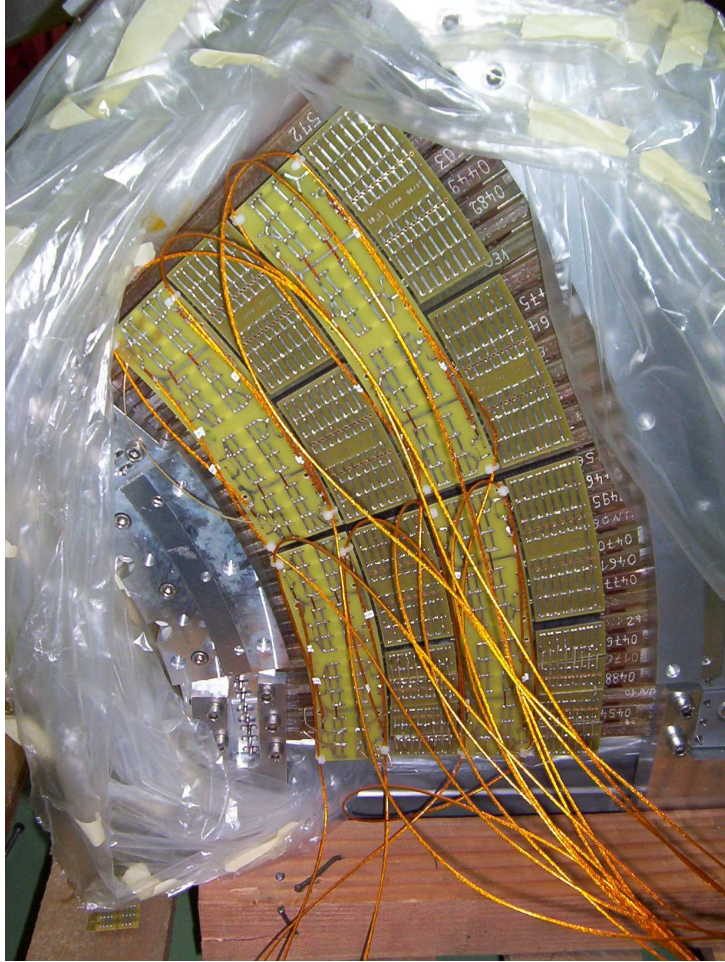


Figure 4.2: Photos of EMEC summing board.

the same disposition as the summing boards, while there is only one mother board to cover these lines. Only the latter could be a possible origin of this strange pattern.

However we should keep in mind that the amplitude of the effect is of the order of 1 *ADC* count that corresponds to a reconstructed energy of ~ 25 *MeV*. Furthermore we did not have the possibility to make direct measures on the test beam setup.

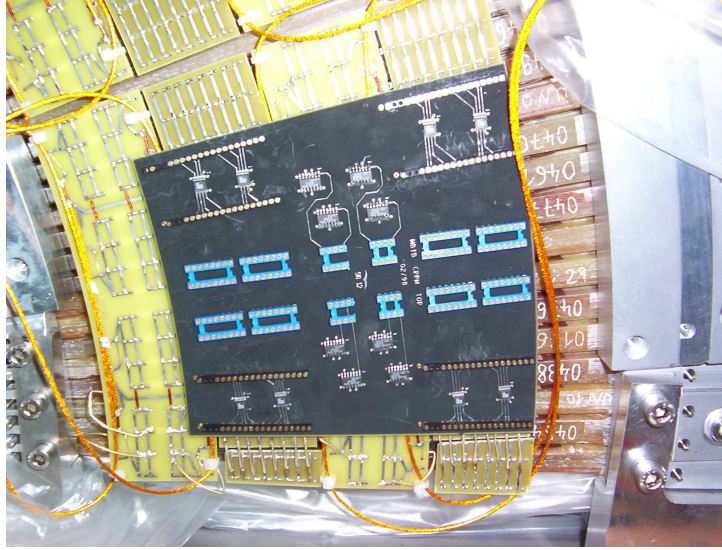


Figure 4.3: Photos of EMEC mother board.

4.2 Search for a low frequency noise.

The origin of this pattern could be the presence of a low frequency noise that affects the distribution of the averages (and increase it) but not that of the RMS. To test it we can make the same plot as in Figure 4.1 but using only 16 or 8 samples instead of 32: in this way the difference between the two values have to change if actually there is a low frequency noise.

Effectively there is such an increase and it seems common to all the layer. A way to show these oscillating noises and to calculate their frequency is plotting the average of the 32 samples versus the signal slope (the latter obtained by linear regression). To obtain the noise frequency we can use the following Formula

$$\left. \begin{aligned} A &= A_0 \sin(\omega t) \\ \frac{dA}{dT} &= A_0 \omega \cos(\omega t) \end{aligned} \right\} \Rightarrow \omega = \frac{\max(\frac{dA}{dT}) - \min(\frac{dA}{dT})}{\max(A) - \min(A)} \quad (4.2)$$

In [15], the same work has been done for the hadronic end cap (HEC): there such phenomena are much bigger, of the order of 300 *ADC*, while in the EMEC these phenomena should have, if there are any, an amplitude $\sim 1ADC$ count. Compared to the enormous oscillations of the HEC ($\sim 300ADC$ counts) the EMEC ones are maybe negligible but they are of the same order of the difference between the RMS of the means distribution and the mean of the RMS one, so this could be the answer to our problem.

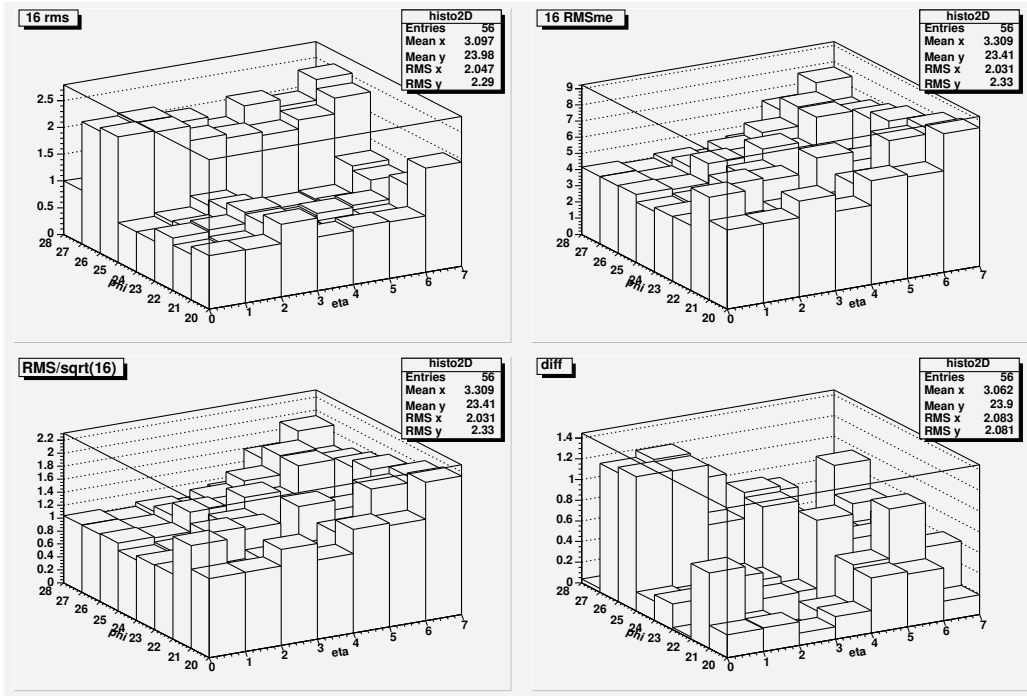


Figure 4.4: Same plots as Figure 4.1 but using only 16 samples for each event.

Unfortunately, for the EMEC we did not find any structure similar to that of Figure 4.6 (on the left): the distribution was uniform and not concentrated on a circumference, even for the cell with a high noise.

One other possible origin of this noise could be a correlation between the HEC and the EMEC: we want to test if the hadronic calorimeter, with its oscillating noise, could influence the EMEC behaviour. For this reason we decided to plot the energy (in ADC counts) of one of the strange EMEC cells Vs. the energy of a HEC cells with an oscillating noise (Figure 4.7).

Even if there seems to be a slight correlation (high HEC values correspond to lower EMEC values), the correlation coefficient ρ is very small: even for the cell $\phi = 25$ $\eta = 1$ we get the value $\rho = -0.17$, so the visual impression has not to be followed.

4.3 Correlation between EMEC cells.

We performed one other test to look for eventual cross-talk phenomena plotting the means of the samples sums of two neighbour cells and observe if

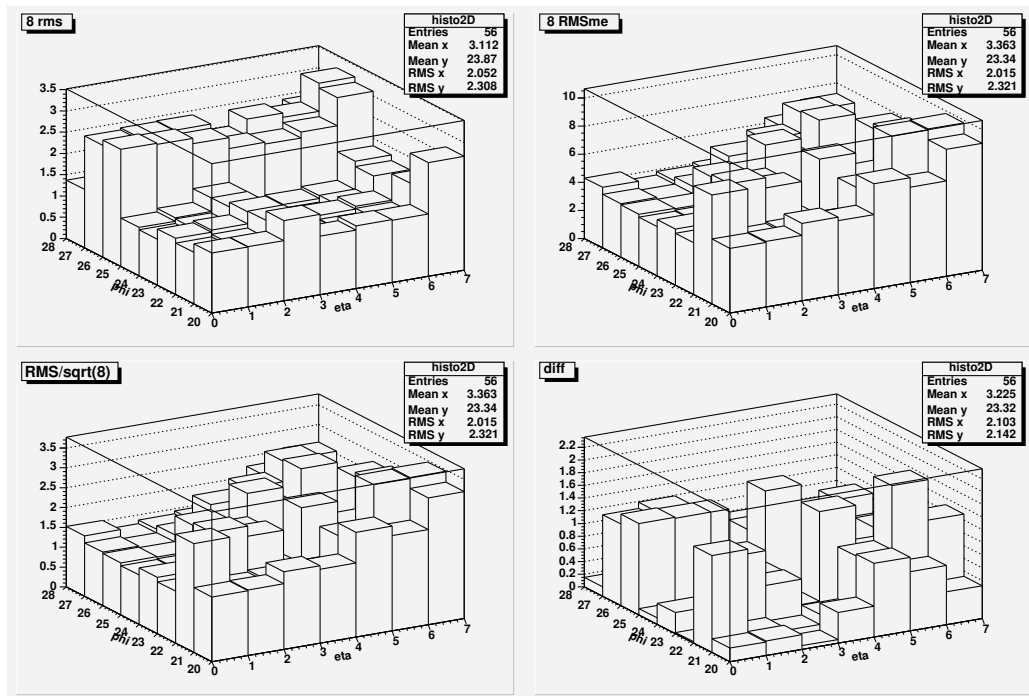


Figure 4.5: Same plots as Figure 4.1 but using only 8 samples for each event.

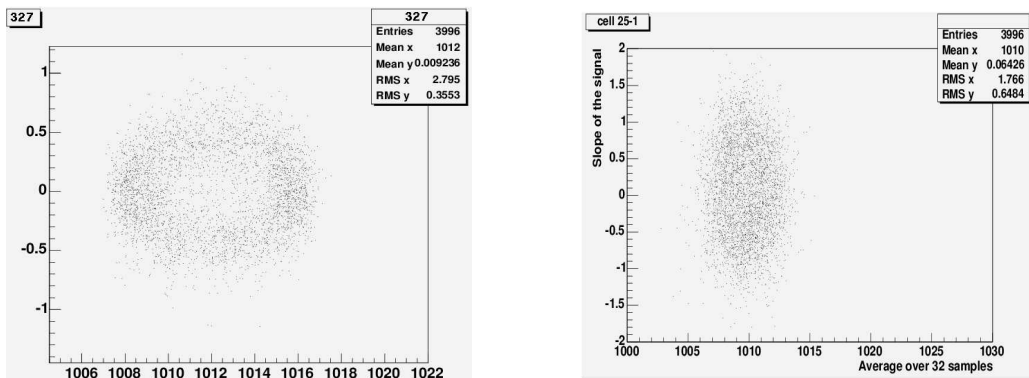


Figure 4.6: *Left*: oscillation in the Hec. We plot the slope of the signal versus the ADC counts output. The pedestal has not been subtracted. *Right*: in the EMEC cell we did not find any oscillating noise, we obtained a completely uniform distribution.

the

$$(RMS(1 + 2))^2 = (RMS(1))^2 + (RMS(2))^2 \quad (4.3)$$

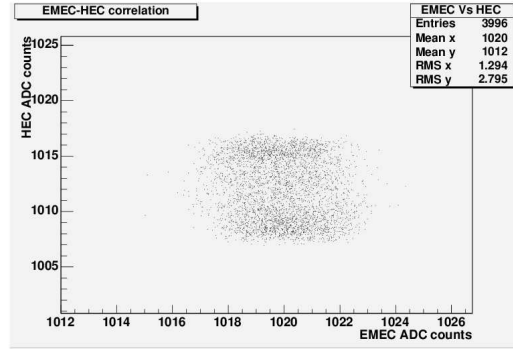


Figure 4.7: EMEC-HEC correlation: apparently there is a slight anticorrelation, but the ρ is too small for a real correlation.

as we should expect from a gaussian noise; that is, we looked for some correlations between the EMEC cells. We took a cell and made this work with the eight neighbours; for the cells in the up left region we note no particular discrepancy, that it means that the cross-talk and other disturbing effects are almost negligible (the difference between $(RMS(1+2))^2 = (RMS(1))^2 + (RMS(2))^2$ is below the 0.5 ADC counts). Instead, in the right side, we have great differences especially between two cells with a high RMS value that means a great noise-correlation between them. Actually, if we make the same plot as in Figure 4.7 but between two EMEC cells, we see a very strong correlation (Figure 4.8). In fact we discovered that *all* the cells are correlated, not only the ones in the columns with $\phi = 25, 26$: the whole calorimeter underwent some fluctuations, in the $\phi < 25$ region less strongly (as we can see from the slope of the plots) but in a way equal to the cells of columns 25 and 26.

Cell 1		Cell 2		ρ	slope a
ϕ_1	η_1	ϕ_2	η_2		
25	1	26	1	0.989	0.89
25	3	21	6	0.72	0.12
21	3	22	3	0.75	0.11
22	2	27	2	0.86	1.61

Table 4.1: As we said, cells with high noise are more correlated than the other. It is interesting to note that even cells with different η values are correlated, confirming the hypothesis that the fluctuation are common to the whole calorimeter.

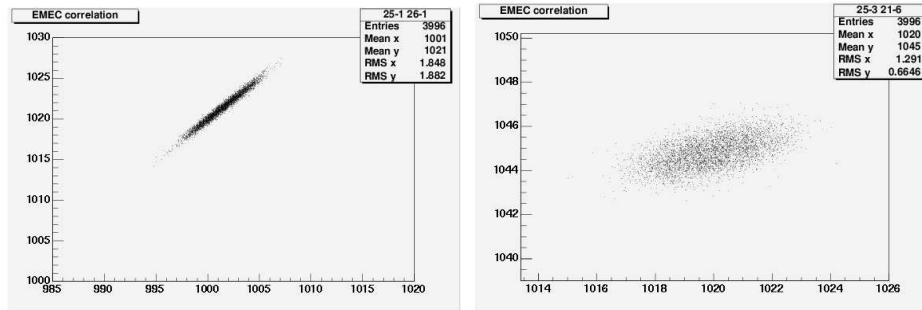


Figure 4.8: EMEC cells correlation. *Left:* the correlation between cells with high noise is strong and the the events are placed on a line with slope 0.89. *Right:* the correlation between these cells is evident but less accentuated and the slope formed by the events is much smaller (0.124).

4.4 Comparison between Test Beam 2004 and other Tests Beam.

We make now a brief comparison between the new Test Beam and an old one (series module H6 of the 2002). The RMS of the old test beam we have analyzed are actually the means of the RMS distribution but with only a sample each event, so we made the same things with the new one.

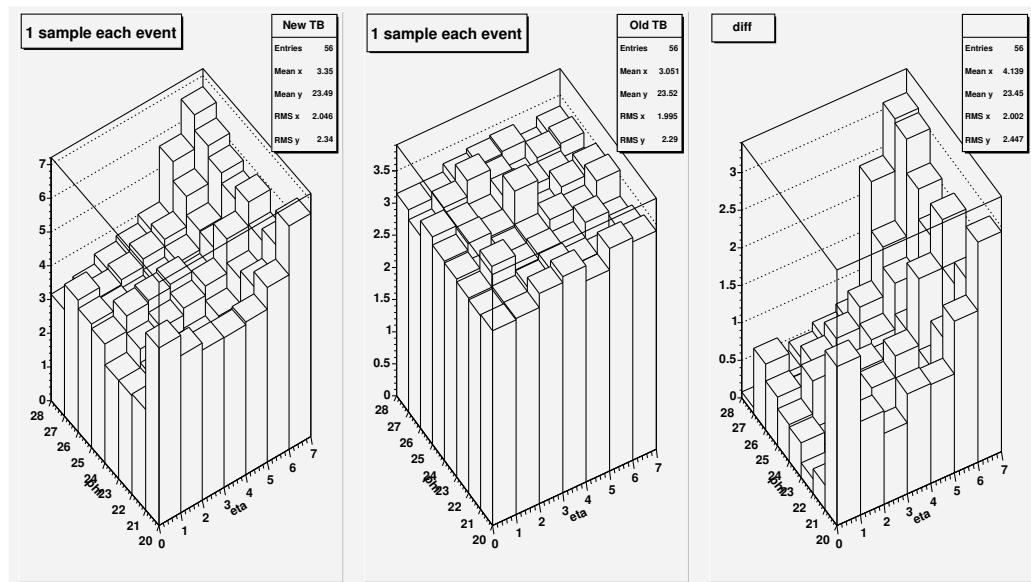


Figure 4.9: Layer 1. *Left:* noise of new TB. *Middle:* noise of the old TB. *Right:* absolute difference between old and new TB noise.

4.4. COMPARISON BETWEEN TEST BEAM 2004 AND OTHER TESTS BEAM.59

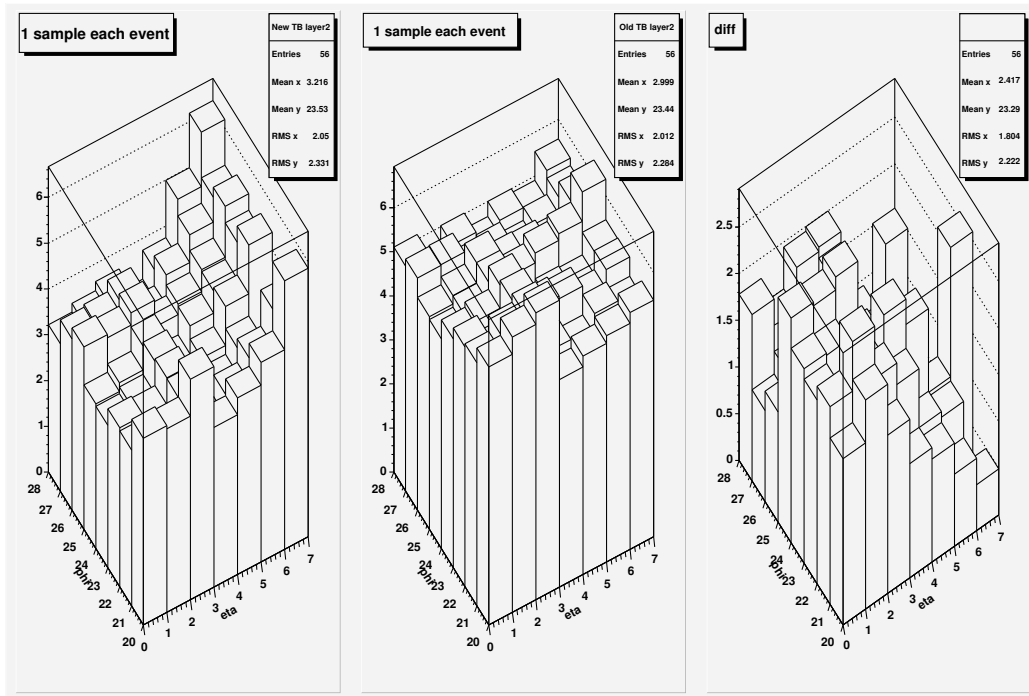


Figure 4.10: Layer 2. *Left*: noise of new TB. *Middle*:noise of the old TB. *Left*:absolute difference between old and new TB noise.

Remarks:

- In both the tests beam the noise was measured in high gain.
- The noise, in the layer 1, has the same order of magnitude but in the old test beam it is more uniform and smaller especially for high η values.
- The two test beam have noise pattern common to the two layer, but while in the old the layer two has a noise greater than that of the layer 1 (at least 2 ADC counts), in the new one the amplitude is almost the same.

Chapter 5

HV corrections

In this chapter we want to analyze the High Voltage corrections that should be performed to the electromagnetic end cap calorimeter data. We have studied only the η -Energy corrections because they are those that strongly affect the uniformity of the response. The ϕ corrections influence the uniformity at a 1% level: a complete study can be found in [20].

5.1 Energy- η corrections

The most important one concerns the η response, because in the EMEC the liquid argon gap decreases with η and to keep a response independent from η we should use a continuously varying potential. For technical reasons, the high voltage is set by steps in nine η sector all over the EMEC, seven for the outer wheel and two for the inner wheel. However, this division leaves an η -dependence that should be taken in account and corrected ([16], [12]). This is done weighting each EMEC cell depending on its η position taken by the center and its HV sector (l) using the following Formula

$$E_{cell}^{HV-corr}(\eta, l) = E^{cell} \cdot \frac{\beta^l}{1 + \alpha^l \cdot (\eta - \eta_l^{center})} \quad (5.1)$$

Let us briefly explain the meaning of the parameters:

- β is a scale factor whose value is in theory close to 1.
- The value of α can be calculated approximately in the following way: we know that the calorimeter response could be written as

$$E \propto \frac{f_{samp}}{g^{b+1}} U^b. \quad (5.2)$$

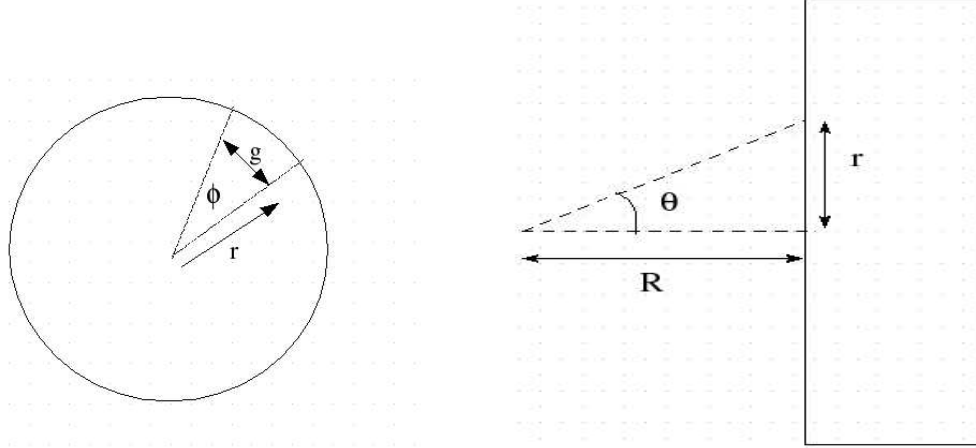


Figure 5.1: *Left*: schematic frontview of the inner wheel. *Right*: schematic sideview.

In each HV sector the high voltage is constant, that is $\Delta U = 0$, so

$$\frac{\Delta E}{E} \sim \frac{\Delta f_{samp}}{f_{samp}} - (b+1) \frac{\Delta g}{g} \quad (5.3)$$

where, as usual, f_{samp} is the sampling fraction and b is the exponent of the power function that fits the HV-Energy curve we have studied in Chapter 3.

We have now to express the gap g as a function of η : as shown in Figure 5.1

$$g \sim r\phi \quad (5.4)$$

$$r \sim R\theta \quad (5.5)$$

so we get the following results

$$\frac{\Delta g}{g} \sim \frac{\Delta r}{r} \quad (5.6)$$

$$\frac{\Delta r}{r} \sim \frac{\Delta \theta}{\theta} \quad (5.7)$$

Keeping in mind the pseudorapidity definition

$$\eta = -\ln|\tan(\theta/2)| \sim -\ln|\theta/2| \quad (5.8)$$

and the relation 5.6 and 5.7, we obtain

$$\Delta\eta \sim -\frac{\Delta\theta}{\theta} \sim -\frac{\Delta r}{r} \sim -\frac{\Delta g}{g} \quad (5.9)$$

In [17] we can see that with a simple calculation we can get

$$\frac{\Delta f_{samp}}{f_{samp}} \sim (1 - f_{samp}) \frac{\Delta g}{g} \quad (5.10)$$

If we insert 5.9 and 5.10 in the expression 5.3, we have the energy variation of each HV sector that we can express, at the first order, as

$$\frac{\Delta E}{E} \sim \frac{\Delta f_{samp}}{f_{samp}} - (b + 1) \frac{\Delta g}{g} \sim (b + f_{samp}) \Delta \eta \quad (5.11)$$

So, if we compare it with 5.1, we deduce that at the first order $\alpha \sim b + f_{samp}$. The value of b being close to 0.4 (see Chapter 3) and the value of f_{samp} between 0.1 and 0.2, our α should fall in the interval [0.4, 0.7].

We have begun our analysis with a Y scan at $X=0$, that is, a vertical scan along the η coordinate in the middle of the detector.

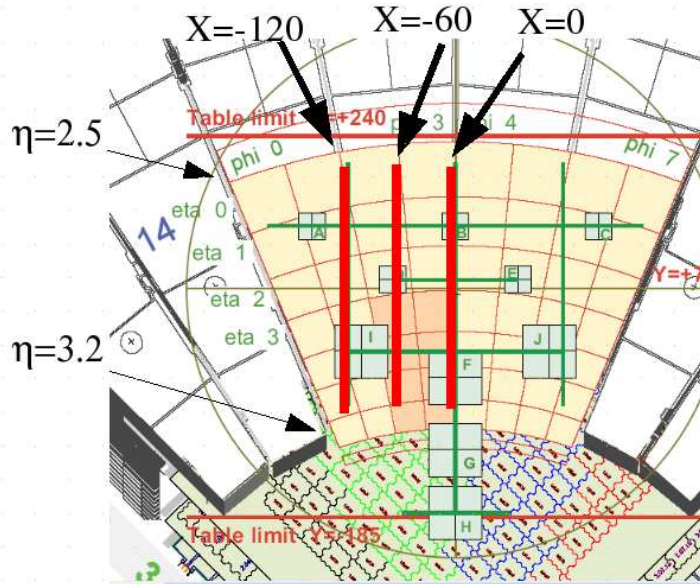


Figure 5.2: EMEC Inner Wheel frontview. We have enlightened the Y-scans at different X performed.

5.1.1 Results of Scans Performed

We used the r-tuple [1359..1376] that are referred to a wide beam of 120 GeV positrons; wide means that the beam hits more than one cell at the time. The energy in these r-tuple has been reconstructed using the cubic fit method and we have calculated the energy of each event using a 3 by 3 cells cluster centered on the barycenter cell as we did in the HV scan. As we already said in Chapter 3 we can state that all the energy of the event is included in such a cluster on account of the cells width ($\Delta\eta 0.1 \times \Delta\phi 0.1$). In Figure 5.3 we have plotted the mean of the η values distribution of the cluster barycenter versus the calculated energy. Being a wide beam, the energy distribution has two or more peaks according to the number of cells in η that have played the role of barycenter.

Watching the Energy vs η plot in fig(5.3) we can immediately see two surprising characteristics: first of all the energy range is very wide, the energy varying by almost 40 %, especially if we compare it to the Combined Test Beam of 2002, where the variation was within the 20% (see [20]). Then, if we consider only Formula 5.1, the point at $\eta = 2.65$ should remain unchanged (it is the center of one HV sector), and so it should have an energy of 120 GeV, the scale factor being close to 1. There are maybe some not well working cells or the problem is in the energy reconstruction.

To test the first hypothesis we made the same work with other scans: one Y scan at X=-60 (narrow beam of 60 GeV electrons) (see Figure 5.3) and runs with the beam on the so called *standard points* (see Figure 5.2): this way we covered almost all the ϕ and η ranges reducing the risk that our results could be biased by dead cells. The resulting plots are in Figure 5.5.

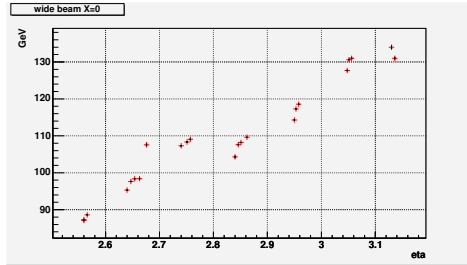


Figure 5.3: Y-scan at X=0 of a 120 GeV wide electron beam.

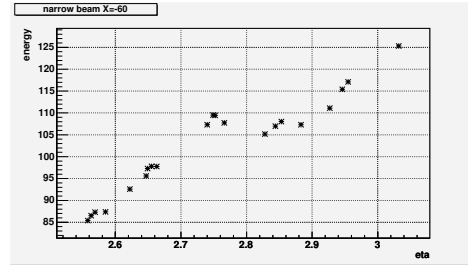


Figure 5.4: Y-scan at X=-60 of a 120 GeV narrow electron beam.

In Figure 5.5 we perceive a slight ϕ asymmetry that we have to analyze but, anyway, it does not change considerably the width of the energy range (our main problem) because it only shifts it. The same behaviour in all the

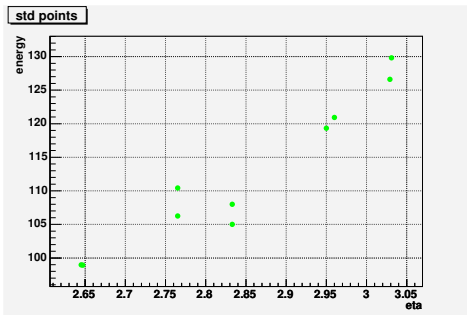


Figure 5.5: Standard points scan.

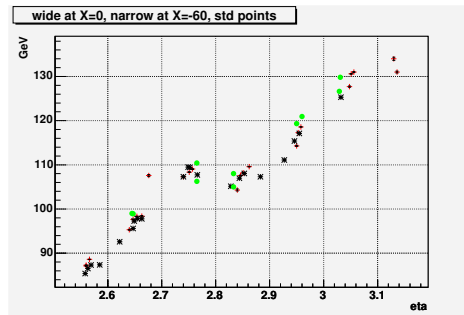


Figure 5.6: Overlapping of the previous three plots.

Kind of scan	R-tuple numbers	Energy	Beam size
Y scan at X=0	[1359..1376]	120 GeV	wide
Y scan at X=-60	[1659..1681]	120 GeV	narrow
Std points: A,B,C,E..	[2331..2410]	193 GeV	wide

Table 5.1: Characteristics of the analyzed runs

runs tested becomes manifest if we superimpose the three previous plots as we do in Figure 5.6.

5.1.2 First corrections

If we try to correct these plots using the Formula 5.1 with reasonable parameters ($\alpha = 0.5$ and $\beta = 1$), we do not reach a constant response in η : the slopes of the points in both the HV sectors decrease but not enough, we are far from getting the correct energy value from all the detector, especially in the low- η HV sector (Figure 5.7).

To obtain it we should use an unphysical α value. Moreover, in the same sector, there is a scale problem to understand. Having excluded the influence of dead cells in this result, the hypothesis of problems in the energy reconstruction becomes predominant.

At the time there was no OF reconstruction: this was the reason we used the cubic fit reconstruction. To test the effect on the response of the reconstruction method, we did the same analysis using some crude optimal filterings: we used 5 samples with the constraint that the sum of the five coefficients that weight the samples be equal to one. The OF we used are:

- [0, 0, 1, 0, 0]: We simply give all the information to the third sample.

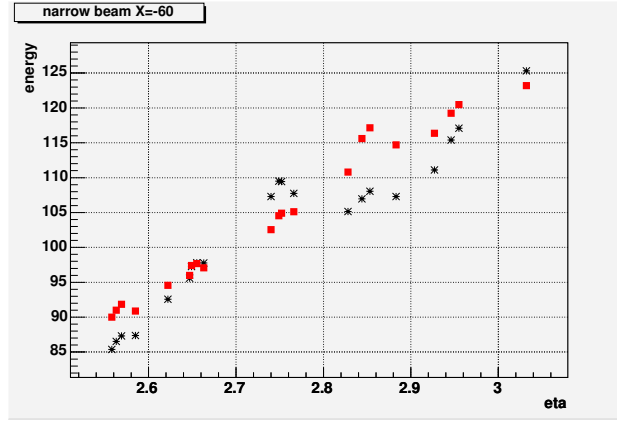


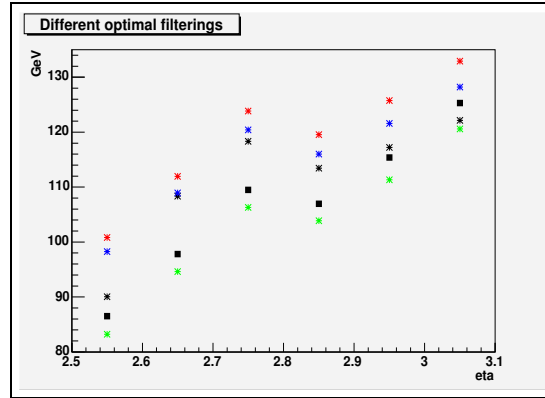
Figure 5.7: HV correction using $\beta = 1$ and $\alpha = 0.5$. We do not get a constant response.

- $[0.2, 0.2, 0.2, 0.2, 0.2]$: we average the signal over the five samples.
- $[0.02, 0.25, 0.38, 0.25, 0.1]$: we weight the coefficient for a signal in the high η HV sector.
- $[0.01, 0.19, 0.34, 0.29, 0.17]$: we weight the coefficient for a signal in the low η HV sector.

To calculate the energy we have used the same 3 by 3 cells cluster.

In these optimal filterings, the problem of the scale factor has been neglected: so, in the plots in Figure 5.8 no attention has to be paid to the absolute energy value but only to the slope of the points. For simplicity we have used only some runs of the Y scan at X=-60, the narrow beam one.

We note, on Figure 5.8, that the slopes we get using these crude optimal filterings are in general less steep than the one of the cubic fit: the situation improves specially for the HV sector closest to the beam pipe, while the change in the other HV sector is not too much significant. To have a quantitative answer to our hypothesis - that is, if there is a problem in the energy reconstruction - we calculate which value α has to assume to give us an η uniform response, in the two HV sector separately: the values in Table n.5.2 show us that actually things get better in the region near the beam pipe and in some case, in the finest filterings, are compatible with the expected α values.



The square points come from the cubic fit					
Black	0.2	0.2	0.2	0.2	0.2
Red	0.02	0.25	0.38	0.25	0.1
Green	0	0	1	0	0
Blue	0.01	0.19	0.34	0.29	0.17

Figure 5.8: Inner wheel response comparing the cubic fit and some crude optimal filterings. We see that for some of them the response in the second HV sector is less step.

Coeff. values	α values	
	$2.5 < \eta < 2.8$	$2.8 < \eta < 3.2$
Cubic fit	1.2	0.8
Crude optimal filterings	1	0.5
	1.1	0.5
	1.3	0.7
	1.1	0.5

Table 5.2: α values needed to get an uniforme response.

Resolution using different method of energy reconstruction.

We must check how resolution changes when we modify the way by which the energy is reconstructed; if we had a great loss in resolution, any improvement in the α value would not be meaningful. For this reason we have calculated, for all our crude optimal filterings, the ratio between the σ of the energy distribution and the mean value of the same distribution and then we plotted

these results in function of η .

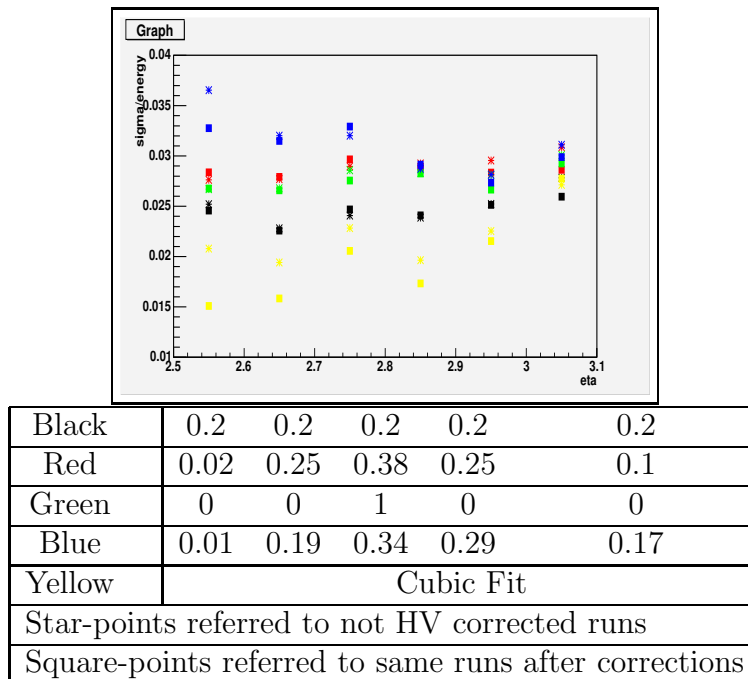


Figure 5.9: Plot to show that using these crude optimal filterings we do not degrade significantly the energy resolution. Moreover, the HV correction itself does not worsen resolution.

Looking at Figure 5.9 it is evident that the resolution of the cubic fit is still better all over the EMEC inner wheel, much better for low- η values and only slightly for high η . Anyway we see that in any case, the HV correction does not worsen the resolution.

In september 2005 the new version of the OFC energy reconstruction was ready but the situation did not improve. The remaining explanation for such a wide energy range was a wrong or missing calibration: what supported this hypothesis was the fact that even in the TB of 2002 we had a similar situation (see Figure 5.10). Let us explain the meaning of this figure:

- the black points are the old TB energies without calibration. The ADC counts response has been directly plotted, without any transformation to nA. Actually the Y-axis of this histogram displays the relative response, because we are interested only in the energy range scale.
- the red points are the energies of the same runs, but obtained using the calibration performed for that TB.

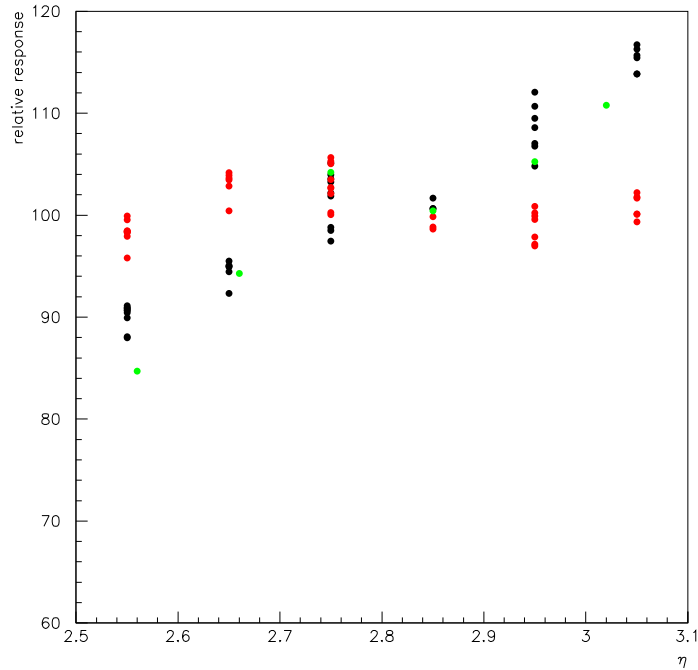


Figure 5.10: Reconstructed energy in function of η in the test beam 2002

- the green points are the energies of some runs of the 2004 TB that we have used above

Actually we see that the Old TB points without calibration covered an energy range very similar to the one that we have found before, while using the calibration (and before any sort of corrections), the range was reduced at least to the half.

Corrections using the new calibration.

Using the new calibration [19], the situation gets immediately better: we calculated the energies for the same runs as before, using the same kind of cluster and we can see that the energy ranges now are within 20%. In Figure 5.11 and Figure 5.12 we have displayed in black the uncorrected energies and

in red the corrected ones for 2 Y-scan, the first using a 120 GeV wide beam in the middle of the detector and the second from a 120 GeV narrow beam at $X=-60$ mm.

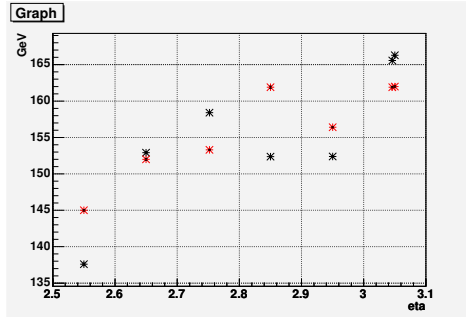


Figure 5.11: Y-scan at $X=0$ of a 120 GeV wide electron beam.

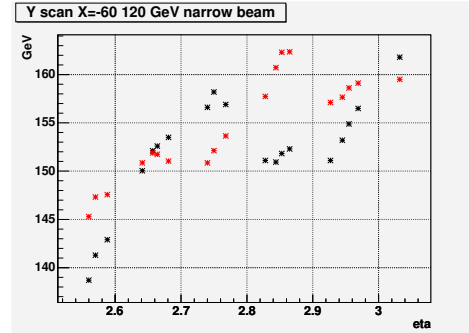


Figure 5.12: Y-scan at $X=-60$ of a 120 GeV narrow electron beam.

This first correction has been performed using $\alpha = 0.5$ for both the HV sectors and ignoring, for the moment, the β normalisation factor. We can say that the new calibration works globally well, all the calculated energies are within 20% and after a correction with an α value that has physical sense the range is within 4%. Anyway we have to remark that:

- The runs that have their barycenter in the $2.5 < \eta < 2.6$ cell have energies smaller than those we expected, even before correction. This can be explained reminding that here we are on the very top of the inner wheel, so for these runs it is not possible to have a nine cells cluster and consequently we have an energy leak.
- The calculated energies in the $2.9 < \eta < 3.0$ cell do not follow exactly the slope of the other cells of the same HV sector, but this could be due to residual cluster level corrections.

We have then performed other scans to confirm the first impression. In Figure 5.13 we have plotted the energies of a 193 GeV wide scan in the middle of the detector. In red there are the energies corrected with $\alpha = 0.5$ for all the sectors while the points in green represent the corrected energies using $\alpha = 0.55$ for the first sector ($2.5 < \eta < 2.8$) and $\alpha = 0.45$ for the second.

Actually we see that the points follow the same trend of the previous scans, with the same problem for the cell at the top of the detector and for the $2.9 < \eta < 3.0$ one. Moreover, changing the correction factor α by 10% does not bring dramatic differences in the corrected energies. Anyway, we will have to find the value that minimize the energy range.

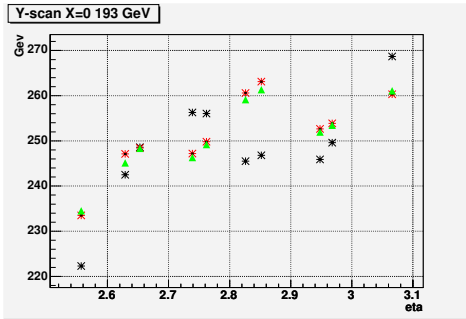


Figure 5.13: Y-scan at $X=0$ of a 193 GeV wide electron beam.

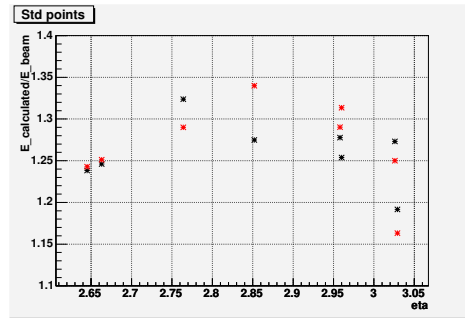
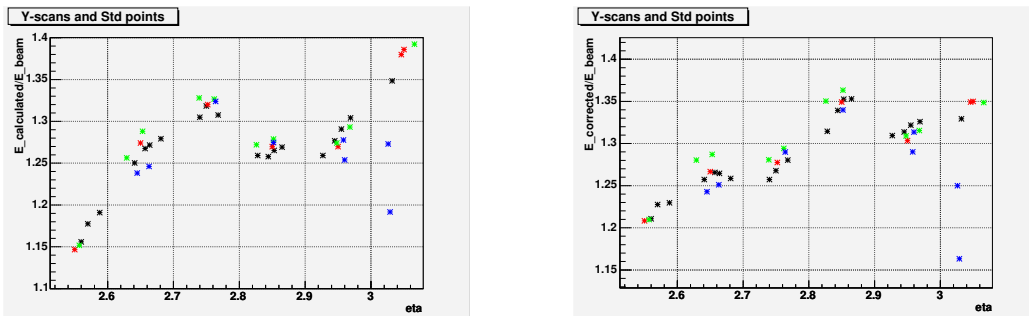


Figure 5.14: Beam of 193 GeV electrons on the Std. Points.

For the runs in which the beam is pointed towards the standard points the situation is a little bit worrying. As we can see in Figure 5.14, the runs with the beam in the Standard Points I and J are well below what expected, their energies are smaller than those that have smaller η . This strange behaviour of the Standard points I and J becomes more evident if we overlap all the previous plots dividing the calculated energies by the beam ones (Figure 5.15). Only these two runs do not follow the common trend. One possible explanation could be a not perfect calibration for those cells



Black	Y-scan at $X=-60$, 120 GeV beam
Red	Y-scan at $X=0$, 120 GeV beam
Green	Y-scan at $X=0$, 193 GeV beam
Blue	Some Standard Points

Figure 5.15: Overlapping of previous scans before correction (on the Left) and after correction (on the Right).

because in Figure 5.6 they were perfectly aligned with the others.

Another explanation could be the gain: actually we see in [19] that while for high gain the calibration is good, for medium gain there are some channels not too well calibrated. Considering the high energy that the runs in the standard point have, there is the possibility that the points I and J correspond to some strange channels. To test this hypothesis, we analyzed a Y-scan at X=-120 with a beam energy of 60 GeV (in this scan we find the same cell of Std Point I): for such an energy the gain chosen is the high one, so the previous problem should disappear. In Figure 5.16) we clearly see that the energy problem is common to all the runs of the scan: the energy we measured is smaller than what expected by about the 20%. Moreover, the normalized energy of the cell with $3.0 < \eta < 3.1$ has the same value of the normalized energy of standard point I, so definitely it is not a question of gain.

We decided to see if using the calibration of the TB 2002, such a problem could disappear: the electronic and the set-up of the two tests-beam are almost the same, so in principle we should find the same values for the two calibrations.

Correction using 2002 calibration.

Indeed, using the calibration of 2002, our problem disappears and the values of the measured energies in the cells of the Y-scan at X=-120 overlap very well the values of the other scans (see Figure 5.16). In Figure 5.17 we have superimposed now the TProfile of the three Y-scans at X=0, X=-60 and X=-120 getting a satisfactory uniform response: using the calibration of the old TB there seems not to have cells that behave in particular strange way. Moreover we can find the same behaviour in cell $2.9 < \eta < 3.0$ for all the three scans, and the differences in energy are very small. To have the maximum of the η coverage and considering the common behaviour of these scans, we decided to put all their data in a common TProfile histogram from which then we extracted the values of α and β .

As a last test, before performing the calculations of the factors α and β , we analyzed a vertical scan at X=120, that is in a symmetric place with respect to the scan that with the new calibration has given some problem. It is the region of the standard point J. Superimposing its TProfile to the common one that we will use to get α and β , we see that uniformity is preserved even in the right side of the detector.

Calculation of α and β

The best values of α for the first and the second HV sector, that is, the values that make the response the most uniform possible, are the ones who

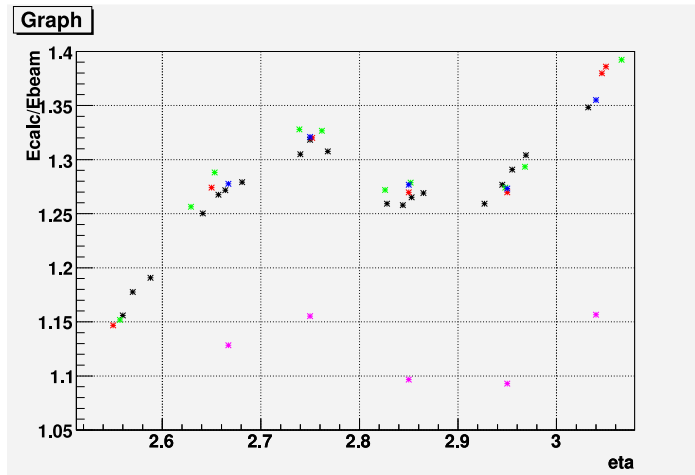


Figure 5.16: In purple are the scan at $X=-120$ at 60 GeV with the new calibration. The blue points belong to the same scan but 2002 calibration has been used (as for the other points).

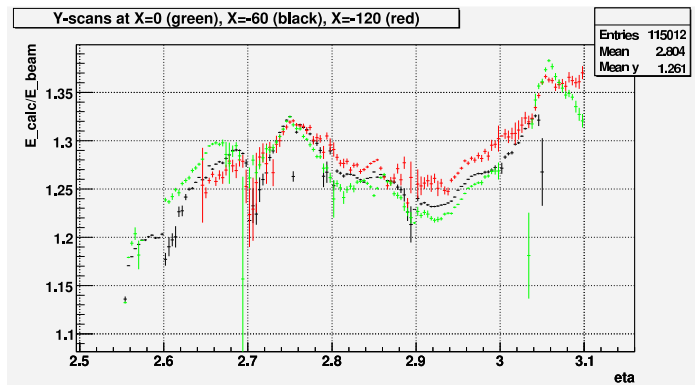


Figure 5.17: We have overlapped the TProfile of three scans: the *green* is a 193 GeV scan at $X=0$, the *red* a 60 GeV scan at $X=-120$ and the *black* a 120 GeV one at $X=-60$. All over the η range differences are within the 3%.

minimize the distribution of the bin values of the TProfile. Varying the α

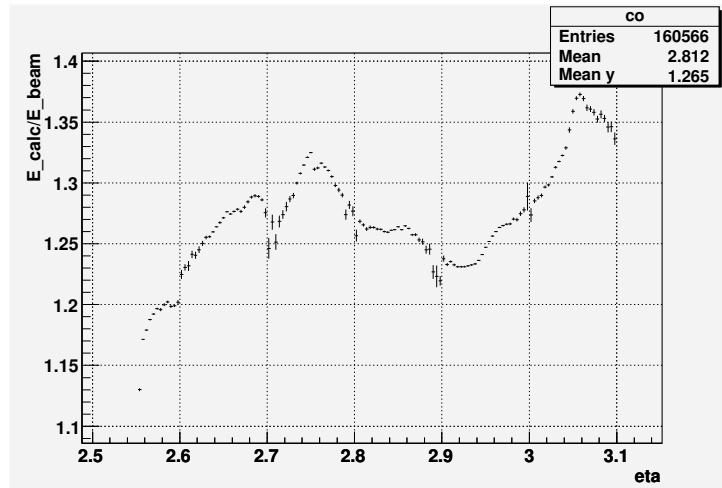


Figure 5.18: We inserted in a single histogram all the data of the three scans at $X=0, -60, -120$.

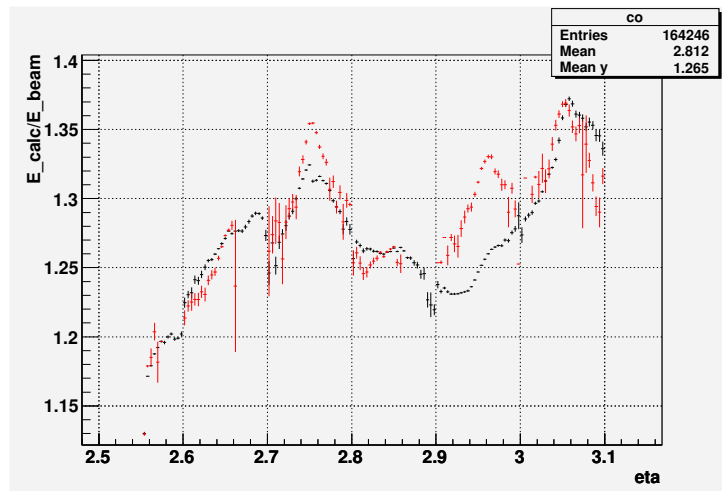


Figure 5.19: Common TProfile and (in red) the scan at $X=+120$. The behaviour is the same with the exception of cell $2.9 < \eta < 3.0$.

values, we see which of them minimise the σ of the bin values, weighting each

Kind of scan	R-tuple number	Energy	Beam size
Y-scan at X=-60	[1659..1681]	120 GeV	Narrow
Y-scan at X=0	[2436..2462]	193 GeV	Wide
Y-scan at X=-120	[2834..2844]	60 GeV	Wide
Y-scan at X=120	[2463..2489]	193 GeV	Wide

Table 5.3: List of the scans used with the calibration ramps of TB 2002. The common TProfile has been created using the first three scans.

bin by the number of events that fall in each bin

$$\sigma_{tot} = \sigma_1 \cdot \frac{n_1}{n_{tot}} + \sigma_2 \cdot \frac{n_2}{n_{tot}}. \quad n_{1,2} \text{ are the number of bins for each HV sector.}$$

$$\sigma_1 = \frac{\sum (\bar{E} - E_i)^2}{\sqrt{N_{ent, i}}} \text{ with } i \text{ that runs over the first HV sector bins.} \quad (5.12)$$

The two HV sectors are not completely independent because the events whose clusters have barycenters in the middle cells have energy correction affected by both the α : an event with a cluster barycenter at $\eta = 2.85$ will have the energy collected by the right cells of the cluster augmented by the correction of α_2 while the energy collected by the other cells is lowered by the α_1 correction (see Figure 5.20).

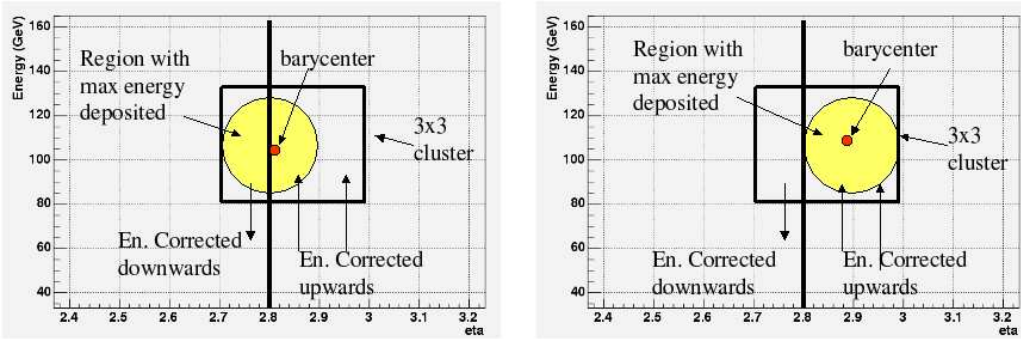


Figure 5.20: How the two α values act on the clusters that have barycenter in the middle cells.

The more the barycenter is close to the border of the two HV sector (in our case $\eta_{bar} \rightarrow 2.8_+$, the lower will be the energy of the event, because it has lot of energy in the first sector. Contrarily, if $\eta_{bar} \rightarrow 2.9_-$ almost all the energy will be in the second HV sector.

In these middle cells the effect of the combination of the two α is summed to second order corrections (common to all the cell) and they are responsible

of the remaining non-uniformity. These second order corrections will be analyzed in section 5.1.3.

The strategy we have followed to get the values of α was to fix α_1 and vary α_2 . Once we found a minimum in the σ of the points distribution, we fixed α_2 and varied α till we converged to a point in the $\alpha_1 - \alpha_2$ plane. As

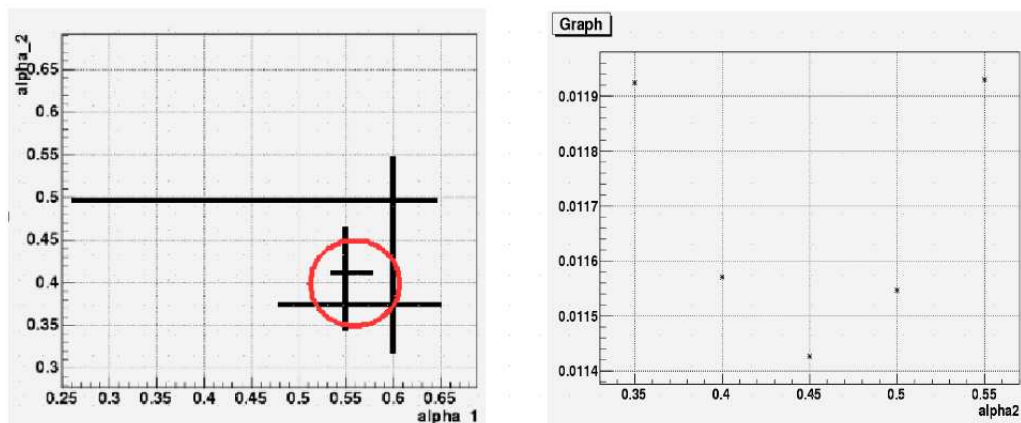


Figure 5.21: *Left*: path followed on the $\alpha_1 - \alpha_2$ plane to find the values that minimize the response range. *Right*: How the σ changes along one of the piece of the path.

we can see in Figure 5.21, the σ of the points distribution is minimized by the couple of values in Table 5.4: Anyway, Figure 5.21 shows clearly that the

α_1	0.55
α_2	0.45

Table 5.4: The couple of α that minimize the points distributions.

minimum is very flat: choosing α values in a 0.1 radius neighbour of α_{best} the response does not change in a significant way the σ . This fact can also be seen in Figure 5.22 and Figure 5.23, where plots obtained with different α values are superimposed.

5.1.3 Cluster level correction

We can perform other corrections at a cluster level. Actually, the cells of our calorimeter have a limited size, so the energy of the events with the barycenter not at the very middle of the central cell is worse contained in such a cluster rather than the energy of an EM shower with the barycenter

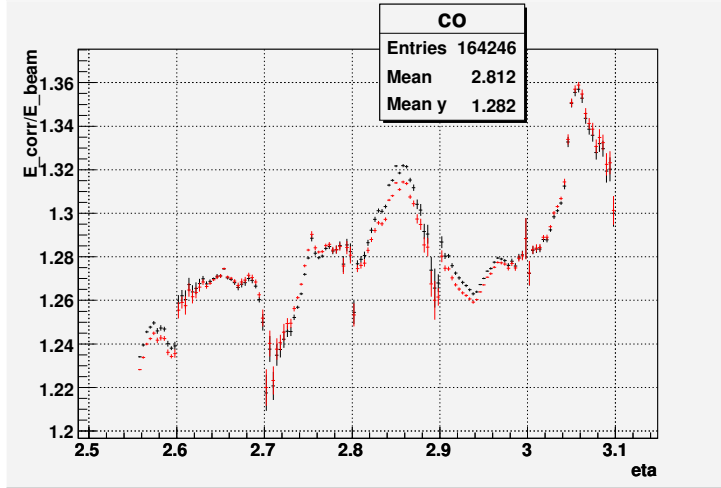


Figure 5.22: *Black*: $\alpha_1=0.55$, $\alpha_2 = 0.4$. *Red*: $\alpha_1=0.5$, $\alpha_2 = 0.35$.

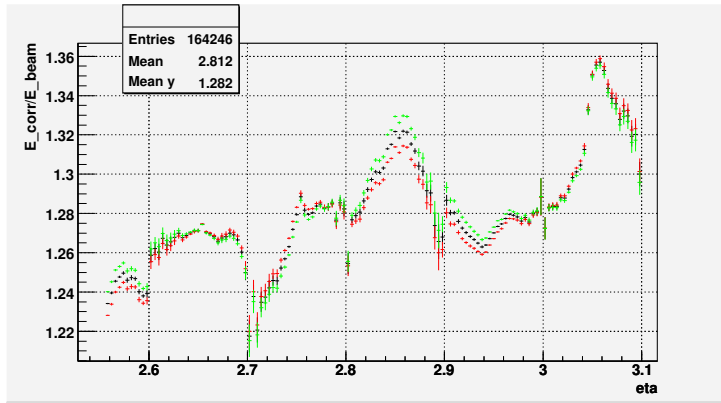


Figure 5.23: *Black*: $\alpha_1=0.55$, $\alpha_2 = 0.4$. *Red*: $\alpha_1=0.5$, $\alpha_2 = 0.35$. *Green*: $\alpha_1=0.6$, $\alpha_2 = 0.45$.

in the middle of the central cell. In principle we should expect a parabolic behaviour [20] within each cell, centered in the middle of the cell.

In Figure 5.24 it was already clear that the cluster level corrections, under the form of parabolic corrections, do not display the same behaviour for all the cells: other effects as the combination of the two α and the impossibility of having a 9 cells cluster (in the $2.5 < \eta < 2.6$), bring variation in the energy response of the same order as the cluster corrections. Correct parabolic corrections can be implemented for the outer wheel of the EMEC [20] (that has finer granularity) while in the inner wheel there are the same problems

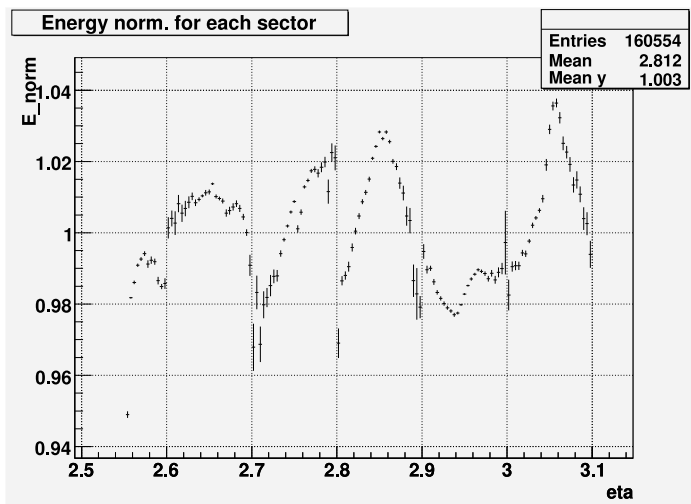


Figure 5.24: Energy response after α and β corrections. The response is inside a $\pm 2\%$ interval over almost all the η -range.

present the TB of 2002.

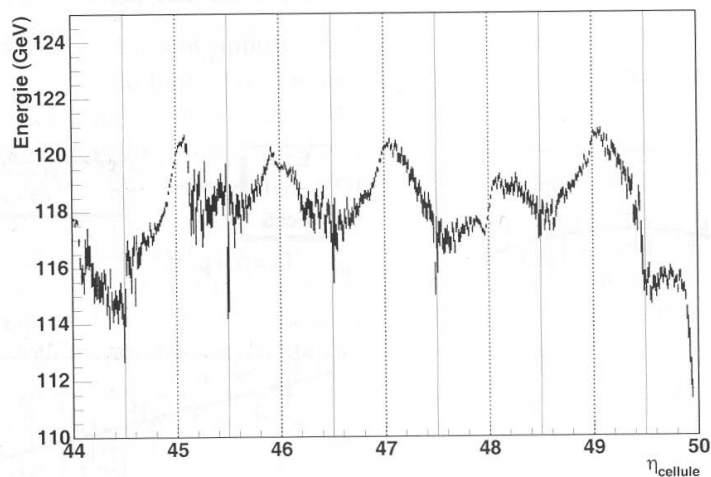


Figure 5.25: Energy response after first order corrections in the TB 2002: the shape is the same as the 2004 one.

Anyway we tried to fit the energy response using the following Formula

$$F(\eta) = C_0(1 + C_1(\eta - \eta_c)^2) \quad (5.13)$$

leaving the center of the parabola as a parameter without fixing it to the cell center. What we get are the fit in Figure 5.26.

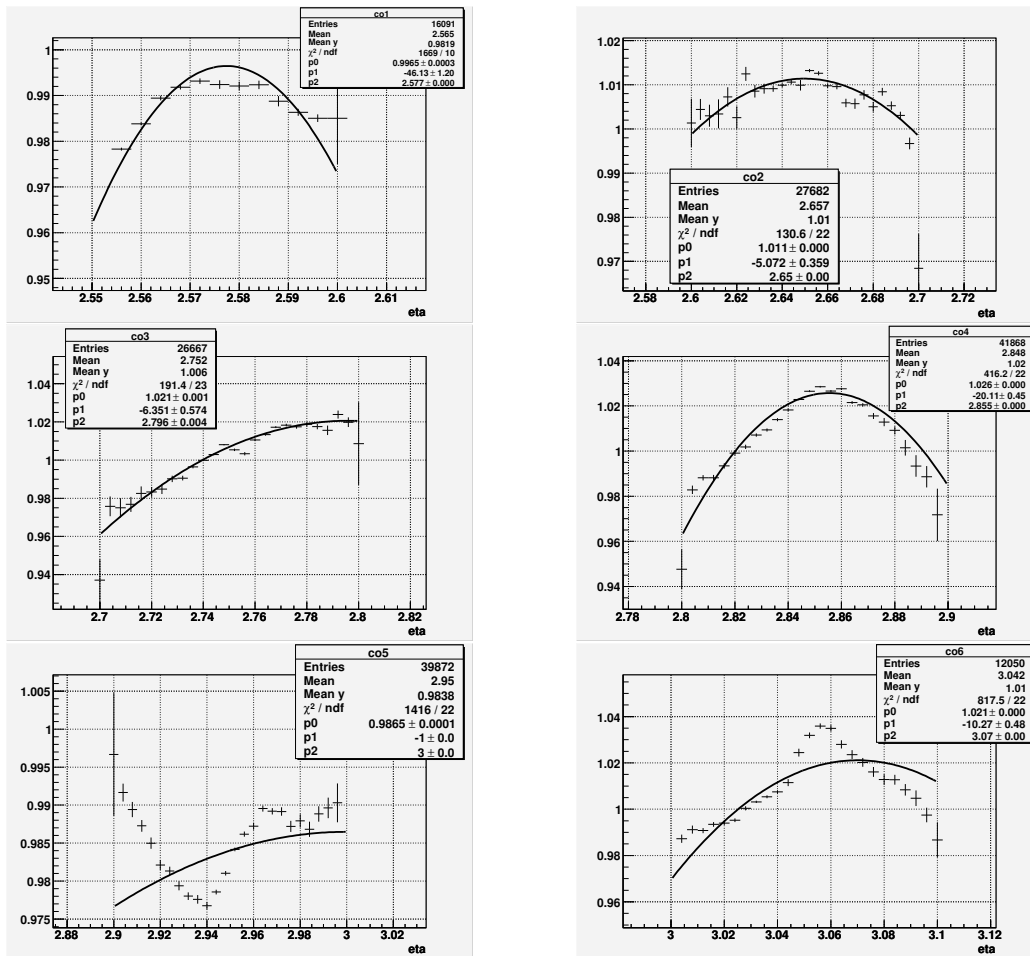


Figure 5.26: Parabolic fit. As in [20], the parabolic fit is pretty good for only two cells.

With the exception of some cells, we are far from the expected parabolic behaviour; in Figure 5.25 we can appreciate that this not-ideal shape of the energy response was common even in the TB of 2002.

The only way to obtain an uniform response is to absorb all the origins of non-uniformity in a polynomial correction, because analyzing them separately will not bring many advantages. Fitting the shape of the energy response with a third degree polynomial we get a satisfactory fit (Figure 5.27).

Using these coefficients we should get the uniform response that we did not find using the parabolic fit. We put them in the calculation of the energy

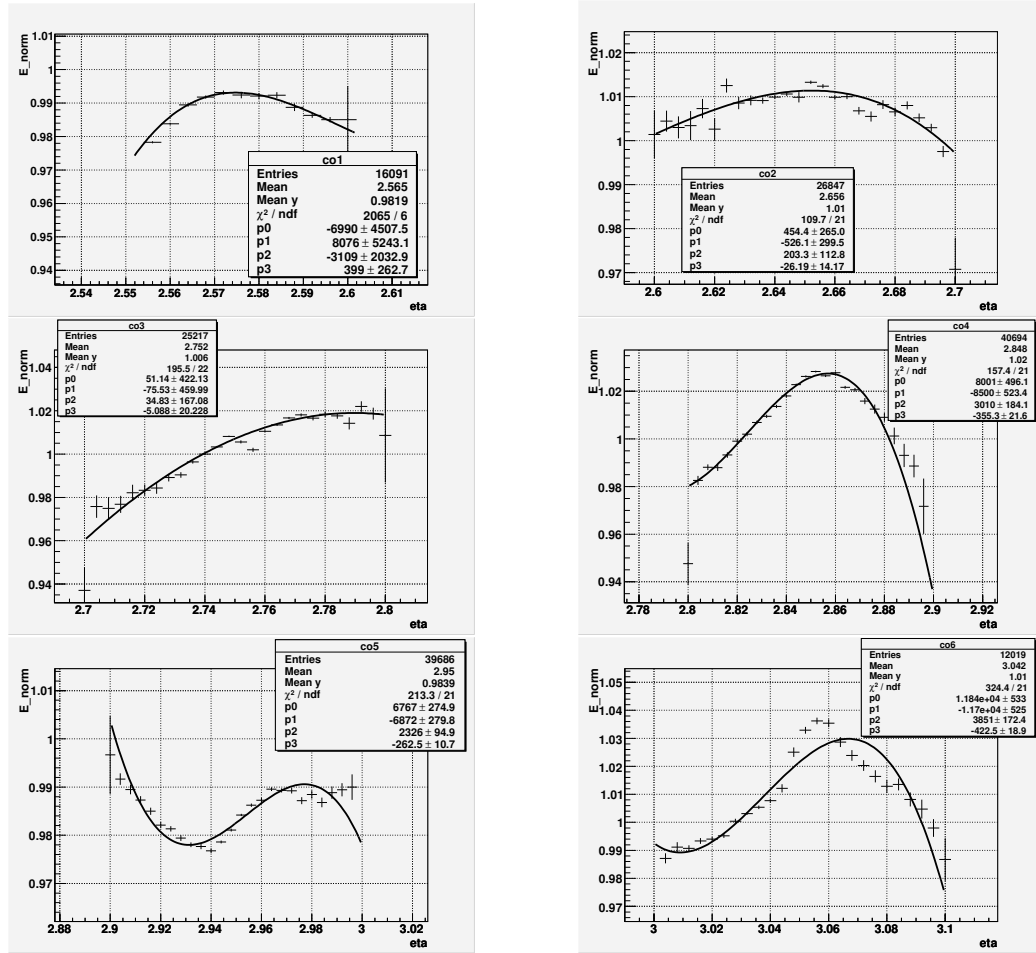


Figure 5.27: Third degree polynomial fit by which we absorb all second order corrections.

of each vertical scan: we have to get almost flat response for all the three scans that made up the TProfile from which we have extracted all the values of the corrections, and even for the vertical scan at $X=120$ of which we have shown the same η -behaviour.

To test it we have calculated the σ of the TProfile points distribution of every analyzed scan: in principle we should obtain a common σ but considering the great number of runs and events of the $X=-60$ vertical scan, the common TProfile used is strongly correlated to that of this scan. So we expect that the distributions of the difference between the corrected energy values and the theoretical flat response will not be centered on zero for the other scans.

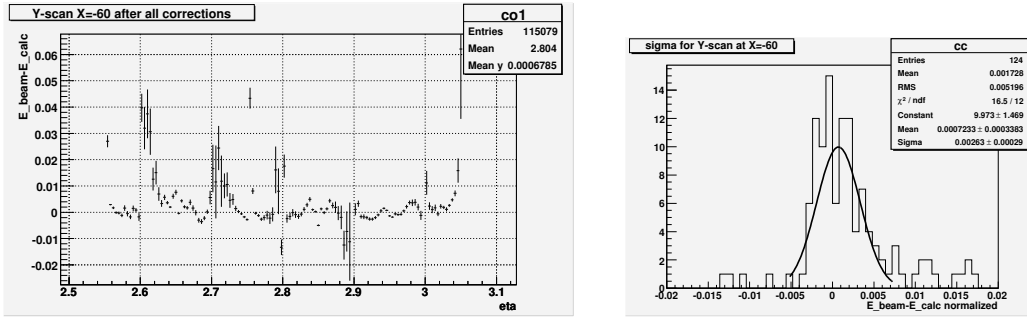


Figure 5.28: *Left*: corrected response for the X=-60 scan. *Right*: distribution of the differences between the theoretical flat response and the calculated one.

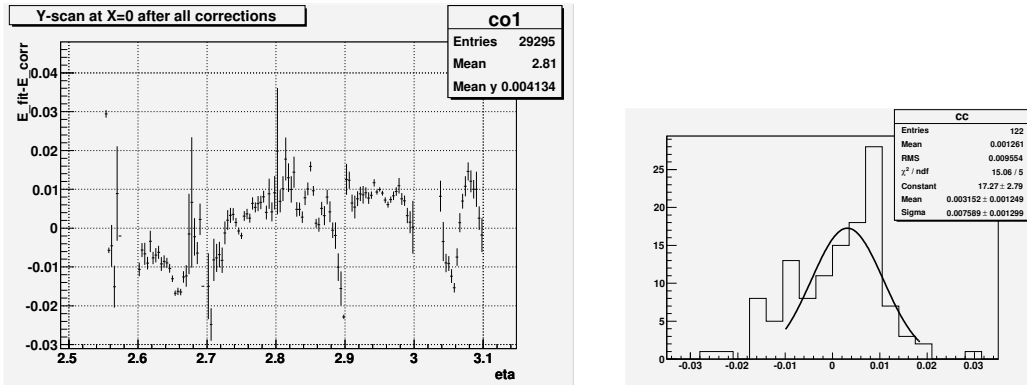


Figure 5.29: *Left*: corrected response for the X=0 scan. *Right*: distribution of the differences between the theoretical flat response and the calculated one.

5.2 Summary and conclusions for Energy- η response.

We briefly summarize the various steps that achieved in this long chapter.

- Using the calibration ramps performed for the test beam of 2004 we obtained an energy range too wide: to have a uniform response in η we were obliged to use unphysical α value.
- With the 2005 calibration things were better but remained one region of the detector where the reconstructed energy was smaller than what expected.
- Waiting for an update for this new calibration we used the well tested calibration ramps of test beam 2002, considering that the test beam

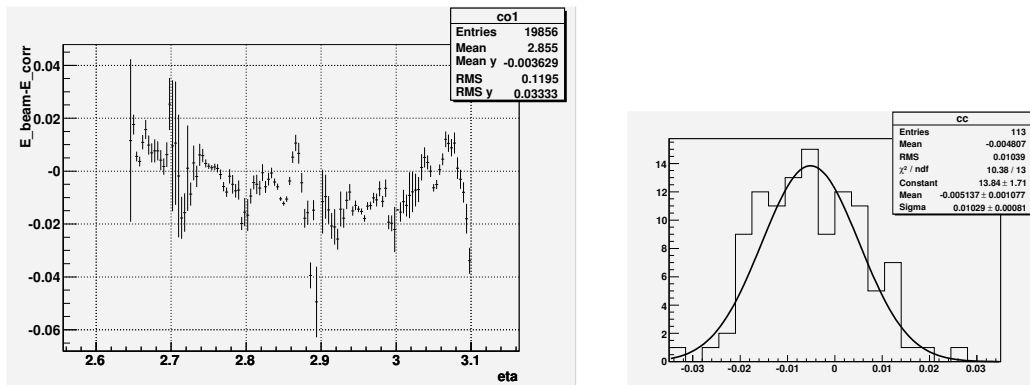


Figure 5.30: *Left*: corrected response for the X=-120 scan. *Right*: distribution of the differences between the theoretical flat response and the calculated one.

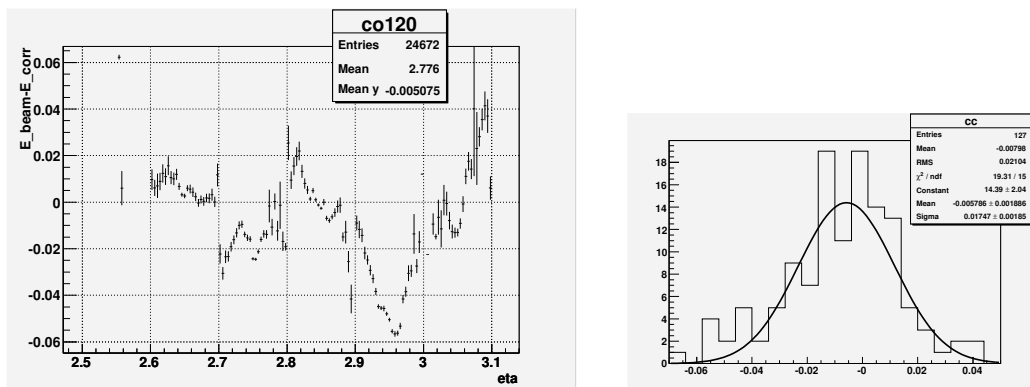


Figure 5.31: *Left*: corrected response for the X=+120 scan. *Right*: distribution of the differences between the theoretical flat response and the calculated one.

setup and the electronics were the same.

- We obtained common energy response for different Y-scans at different X positions and energies: so we created a common TProfile histogram from which extract α values averaged all over the detector X position.
- Using the values of Table 5.4 our energy response is within an interval of $\pm 2\%$.
- About all second order corrections, we have absorbed them in a third degree polynomial fit. The energy response after all corrections is within $\pm 1\%$.

Chapter 6

Spatial Resolution

In this chapter we will focus our attention on the spatial resolution of the Inner Wheel of the EMEC, in order to calculate with which precision our calorimeter can detect the position where the particles hit it. About ϕ -resolution, the results of this chapter will be used by the Cracow ATLAS group for a luminosity study using a pair of low energy electrons produced from an hadronic interaction by the process in Figure 6. The electron pairs

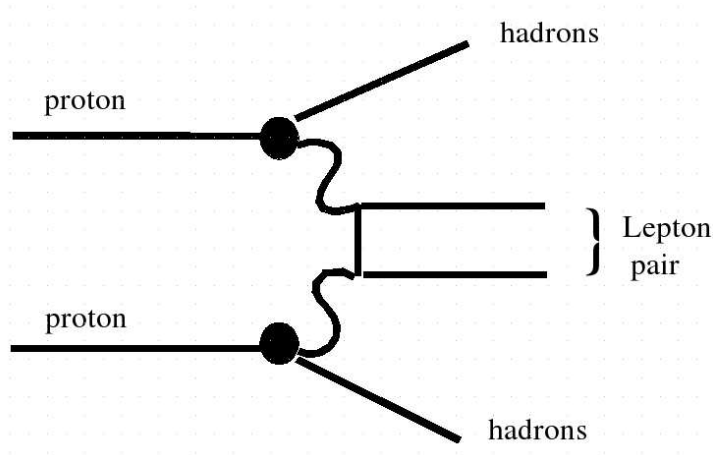


Figure 6.1: Feynman diagram for the calculation of luminosity using an electron-positron pair produced at high η .

will be produced at a ϕ -angle of 180 degrees, so a very good knowledge of ϕ resolution (specially at low energies) is necessary to get the correct value of luminosity.

The use of calorimeter ϕ -position measurement is illustrated in [7].

6.1 Global ϕ -resolution

During the Test Beam of 2004 there were 6 Beam Profile Chambers (BPC) all along the the beam [21], before the cryostat. These chambers give the beam positions in the $X - Y$ plane, event by event. They are high precision

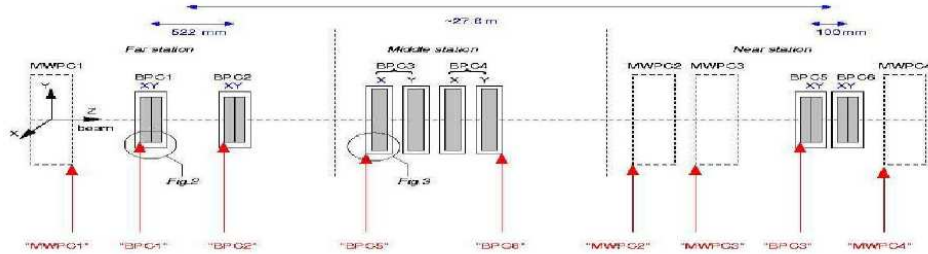


Figure 6.2: BPCs setup during the Combined Test Beam of 2004.

chambers that should have a very good intrinsic resolution better than the detector one, in order to not influence it. During the Test Beam the position of the BPC has not been changed; it was the detector that was moved to test all its cells.

BPC #	<i>position</i>	
0_X	=	0
0_Y	=	31
1_X	=	522
1_Y	=	553
2_X	=	11076
2_Y	=	11154
3_X	=	11219
3_Y	=	11294
4_X	=	27645
4_Y	=	27676
5_X	=	27745
5_Y	=	27776

Table 6.1: Relative position of the BPCs (in mm).

To obtain the detector resolution, we made a 2-dimensional plot with the values of the X coordinate of the BPCs versus the ϕ coordinate of the barycentre of the usual 3×3 cells cluster used to calculate the beam energy. From this plot we see the correlation between these two variables.

We have used runs with a beam pointed in the center of the detector, to have X and ϕ in the same direction: so rtuple from Y-scan at $X=0$ and rtuple with the beam directed toward the standard points B and F. If we chose edge cells, ϕ and X would not have the same direction and the correlation between them would not be simple, complicating the analysis. To resolve this problem one could in principle perform a rotation of the axis using a linear parametrization of the coordinates.

From the 2-dimensional histogram, we have produced a TProfile histogram to get the parameters of the first degree polynomial that fits the points. Then, by these parameter, we filled an histogram with the differences between the measured ϕ value and the relative one given by the fit.

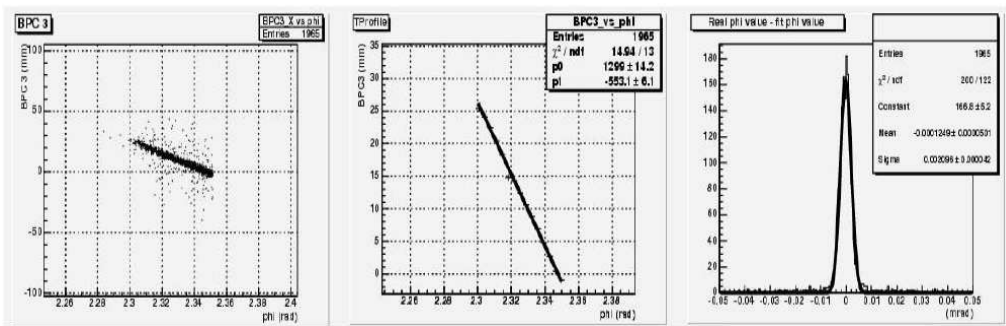


Figure 6.3: Steps to get the ϕ -resolution: *Left*: BPC position versus ϕ -coordinate of the cluster barycenter. *Middle*: correlation parameters extraction. *Right*: Distribution of the difference between the measured ϕ value and the fitted one. Its σ it is the global ϕ -resolution.

In all our analysis we have considered for each run only one cell of the dimension of 0.1×0.1 in η and ϕ

6.1.1 Global ϕ -resolution Vs. η

Before proceeding with our analysis, we have to say that what we measured using the previous method is a *global* σ , that is, the σ of the global resolution and not of the detector one. In fact, we can express the former σ as the square sum of three contributions:

$$\sigma_{global} = \sigma_{BPC} \oplus \sigma_{MS} \oplus \sigma_{CALO} \quad (6.1)$$

- σ_{CALO} : it is the intrinsic σ of the calorimeter that we are looking for.

- σ_{MS} : contribution caused by multiple scattering. The particles of the beam interact with the particle of the air they find between the BPCs and before reaching the cryostat. The interaction with the chambers should not give a significant contribution to the multiple scattering effects: they are composed by two $120\mu m$ sheet of mylar at a distance of 40 mm filled of gas (80% argon and 20% oxygen) that gives a negligible contribution if compared to the air one (see section 6.1.3).
- σ_{BPC} : the intrinsic σ of the chambers.

Our goal is to extract the intrinsic detector resolution, so we have to measure or calculate all the other contributions.

We began by studying the behaviour of the global resolution at different η , how it changes when we approach the beam pipe. For each BPC we have plotted the measured global σ at different η , using some runs of a Y-scan of 120 GeV electrons. From Figure 6.4 we see some common features:

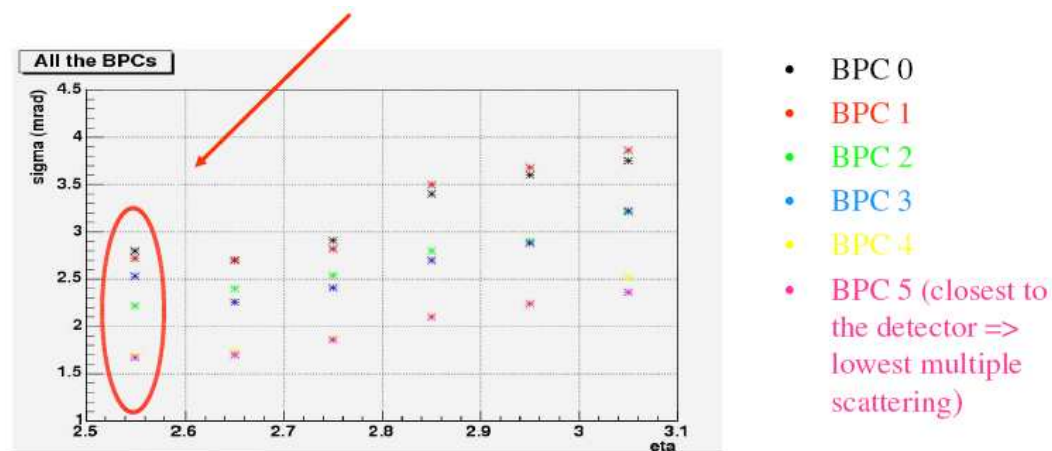


Figure 6.4: How the global ϕ resolution changes with respect to η and to the BPC considered.

- for all the chambers σ_{global} increases with η almost in a linear way. The increment is mainly due to geometrical reasons.
- σ_{glob} is smaller for the BPCs closest to the detector.
- the σ for each couple of BPCs is almost the same.
- The points at $\eta = 2.55$ do not follow the slope given by the other points. One explanation could be that for this cell (with $2.5 < \eta < 2.6$ and

$2.25 < \phi < 2.35$) we cannot create a 9 cells cluster because we are at the very top of the inner wheel; so there is an energy leak that could worsen our resolution.

If the fact that σ is smaller for BPC5 can be explained on account of multiple scattering effects (as the fact that for each couple it is almost the same), there is an argument that made us think that, *a priori*, the resolution should be better in the higher η region: here, as we said in Section 2.3 when we talked about the geometry of the detector, the absorber are closer than in the low η region. So, in principle, we should have obtained more precise measures. We can conclude that the varying ratio between the shower dimension and the cluster dimension ϕ is more important than the fact of having closer absorbers.

6.1.2 Global ϕ -resolution Vs. Beam Energy

The next analysis on the global sigma concerns how it does vary as a function of the Beam Energy, at a fixed η value. We used only the cells with $2.6 < \eta < 2.7$ and $2.25 < \phi < 2.35$. Among the runs of the Period II of the Test Beam we have found for this point seven different energies for the electron beam listed in Table 6.2.

Run Number	Energy
3309	6 GeV
3259	10 GeV
3604	30 GeV
3683	40 GeV
2876	60 GeV
1371	120 GeV
2456	193 GeV

Table 6.2: Runs used.

The energies used are the tabulated ones and not those that we have calculated using the cluster; so the η -Energy corrections are not taken in account. Anyway, this cell is in the middle of the first HV sector, so the α value of Formula 5.1 does not influence the reconstructed energies, only the scale factor β can influence the calculated energies.

The method used to to get the global σ is the same, but here we tried to fit the points using the function

$$\sigma_{global} = \frac{a}{\sqrt{E}} \oplus const. \quad (6.2)$$

We have chosen this function because when we use the energy in the determination of the position, we expect that the spatial resolution had to follow the behaviour of energy resolution, which varies as $1/\sqrt{E}$. To decouple the two contributions we plotted the σ^2 versus the energy. For low energies runs, we

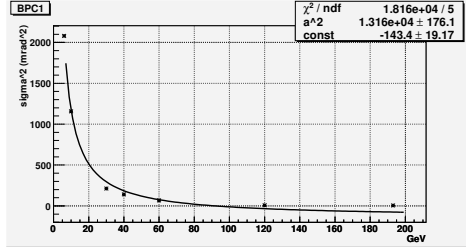


Figure 6.5: σ^2 vs. Energy for BPC1.

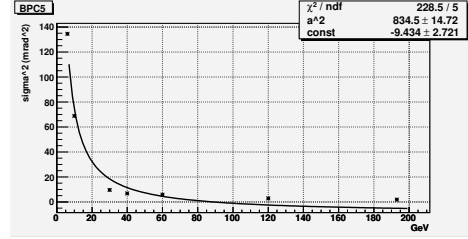


Figure 6.6: σ^2 vs. Energy for BPC5.

can actually see that there is a considerable difference between the resolution measured using the BPC 0 and that using BPC 5: this is not very surprising, because the Multiple Scattering effects depend strongly on the beam energies and they grow when the energy diminishes.

However, we can see that this fit is not as good as what we expected: even for the BPC closest to the detector the points at 30 *GeV* and at 40 *GeV* are not well fitted and the constant term of the fit function is many error bars below the zero. For these reasons we try to fit the curve with an other function:

$$\sigma_{global} = \frac{a}{E} \oplus const \quad (6.3)$$

Using this function the previous problems seem to be solved (Figure 6.7 and 6.8).

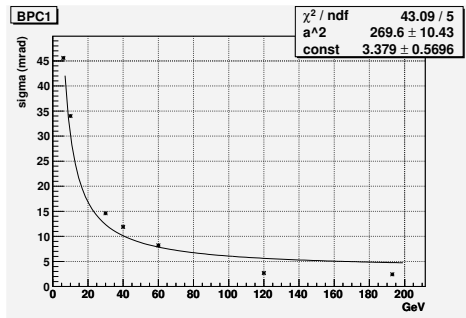


Figure 6.7: σ vs. Energy for BPC0.

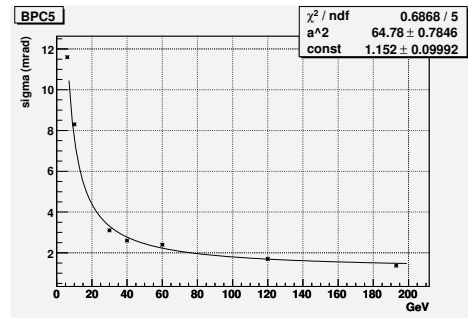


Figure 6.8: σ vs. Energy for BPC5.

6.1.3 Intrinsic BPC resolution

Anyway, we have also to calculate the intrinsic resolution of the BPCs. We use the fact that the BPCs are grouped in couples and that we can state, from the distances in Table 6.1, that multiple scattering effects between them are negligible if compared to the global M.S. contribution. Moreover, from the technical characteristics of the BPCs reported in [21], we can also state that they do not contribute significantly to M.S. effects: in fact they are made up by two $120\mu\text{m}$ layer of a plastic called *Mylar* separated by 30 mm of gas (a mix of argon and oxygen). From the following Formula

$$\theta_0 = \frac{13.6\text{MeV}}{\beta_{cp}} z \sqrt{\frac{x}{X_0}} [1 + 0.038 \ln(x/X_0)] \quad (6.4)$$

that gives the amplitude of the dispersion, in θ , due to the multiple scattering, and from the X_0 values of mylar and argon given in [22] we obtain that

$$\theta_{0, BPC} = \theta_{0, Mylar} + \theta_{0, Arg+Oxy} \simeq \frac{13.6\text{MeV}}{\beta_{cp}} \sqrt{0.001} \quad (6.5)$$

while the contribution of the multiple scattering between the BPC5 and the detector is

$$\theta_{0, BPC-CALO} = \frac{13.6\text{MeV}}{\beta_{cp}} \sqrt{0.07} \quad (6.6)$$

at least 70 times bigger. To know the intrinsic ϕ -resolution of the chambers, we have plotted the x-position of one chamber if function of the x-position of the coupled one; then we have followed the same way: TProfile to get the fit parameters and then the distribution of the differences between the measured and the fitted value. In fact we considered as the coupled BPCs were actually one next to the other. The fact that the intrinsic resolution is not the same for all the BPCs is not too much surprising:

- The couple in the middle are actually different from the others: in [21] we see that while the other couples contain two measurement planes (X and Y), the middle station chambers are pairs of physically separated single plane chambers.
- The intrinsic resolution of the first couple is worse than the last one because the distance between the two chambers is greater.

Anyway, to analyze their influence on the global σ term we have first of all to convert them in *mrad*. We can use as a conversion factor, for each run

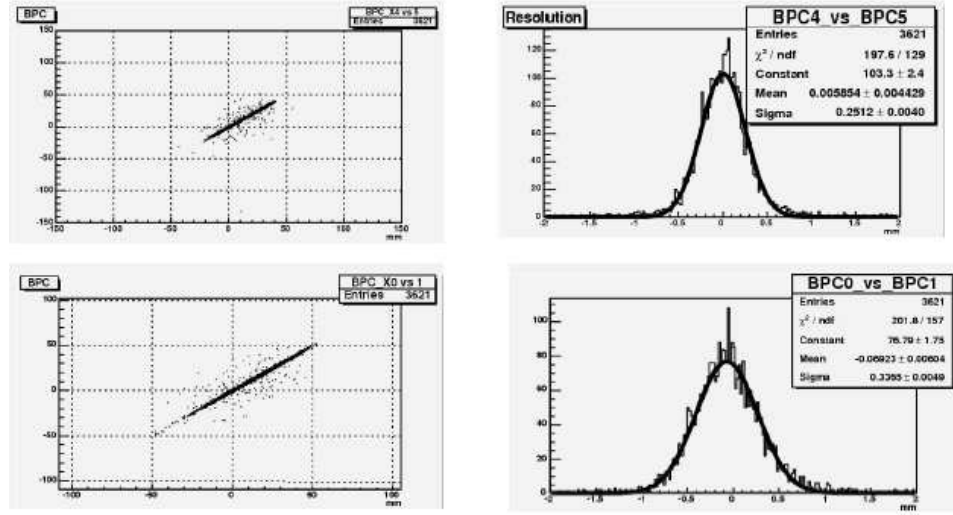


Figure 6.9: *Top*: intrinsic resolution of the BPCs closest to the detector. *Bottom*: intrinsic resolution of the farthest couple of BPCs.

and each BPC, the slope of the fit given by the TProfile histogram in Figure 6.3, where we had mm vs. $mrad$. So,

$$\sigma_{BPC,rad} = \frac{\sigma_{BPC,mm}}{\sqrt{2}} \cdot conv. factor = 0.0003 rad \quad (6.7)$$

we get that the contribution of the intrinsic resolution that in low energy case is completely negligible; in higher energies case, we can estimate its influence calculating $\sigma_{BPC}^2 / \sigma_{glob}^2 = 4\%$ (where for σ_{glob} we have taken the smallest value from the 120 GeV runs displayed in Figure 6.4). For our study we can consider it negligible. As last check, in the plot of Figure 6.10 there is the proof that the intrinsic resolution of the BPCs does not change with energy.

6.1.4 Multiple Scattering contribution

As we have already said, the multiple scattering (MS) contribution has to be evaluated correctly because it could strongly influence the value of the calorimeter resolution we are looking for, especially in low energies cases or when we use the BPCs that are far from the detector. In Figure 6.11 we can clearly see how the correlation between two fixed chambers (and so the measured resolution using those chambers) changes with the energy. We have taken the BPC0 and the BPC5, that are 27,5 m far (see Table 6.1), and we

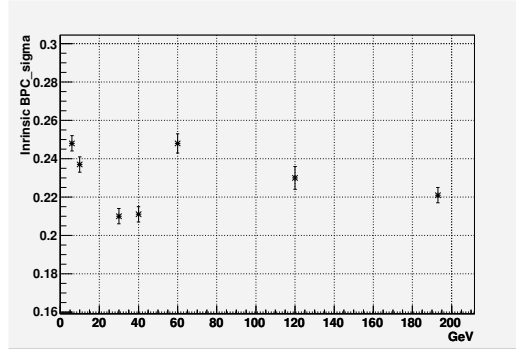


Figure 6.10: The intrinsic BPCs resolution does not depend on energy.

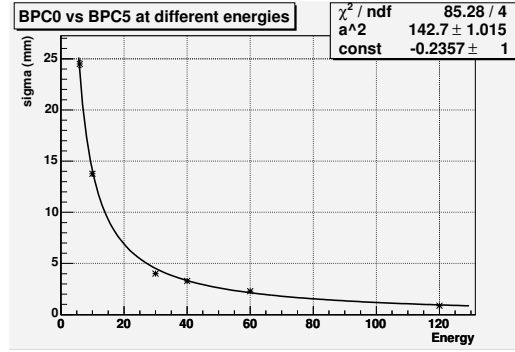
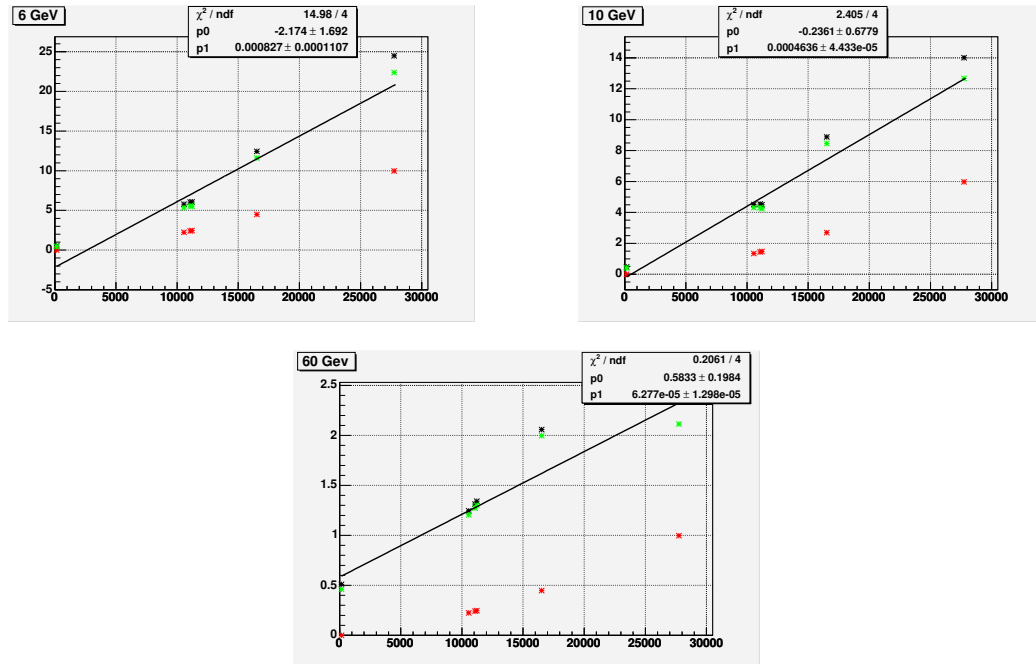
have plotted their combined σ in function of the beam energy; the curve is very well fitted by a function of the form $\sigma = a/E + const.$ and show that for a given distance, the resolution degradation is due to an MS-like effect (the multiple scattering could be only one of these factors). In effect, we should have that $\sigma_{BPC0,BPC5} = \sigma_{BPC0,BPC3} \oplus \sigma_{BPC3,BPC5}$, if the MS were the only origin of the resolution degradation. That is, the squared sum of the multiple scattering contribution given by Formula 6.4 and the intrinsic BPCs resolution, should give us the resolution measured between the BPCs. If we plot the difference between the measured σ and the σ_{MS} given by

$$y_{plane} = \frac{1}{\sqrt{3}}x\theta_0 \quad \theta_0 \text{ given by (6.4)} \quad (6.8)$$

(see [22]), what we obtain is not the negligible contribution of the intrinsic resolution of the BPCs. We can see from the plots in Figure 6.12 that there is an additional term that grows almost linearly with the distance between the chambers and that could be interpreted as a beam divergence term. From the same plots, anyway, we can understand that if we use the BPC5 (that is only 2.2 m far from the cryostat), this contribution will be negligible.

6.2 Global η -resolution

The finite granularity of pad detectors give rise to systematic shift [23] of the center of the shower toward the center of the cell because the η and ϕ values we found in the rtuple for each cells are those of the center of the cell: so, nevermind where the particle will hit the cell, we will get, as its position, the position of the center of the cell. In Figure 6.13 we show how the correlation between Y and η changes when we pass from an infinite to

Figure 6.11: σ from BPC0 vs BPC5 in function of the energy.Figure 6.12: σ_{global} in black and σ_{MS} in red vs the distances between BPCs for 3 different energy beams. The green points come from the squared difference of the previous two term: they can be interpreted as points of a divergence term.

a finite granularity. Our case is slightly different because we are using a 9 cells cluster, so the effects of the finite granularity are smoother. In principle we should have found the same effect in the ϕ case, but there the accordion geometry induces a better energy sharing between neighbouring cells, making this S-shape effect negligible. These S-shape found for η can be fitted and

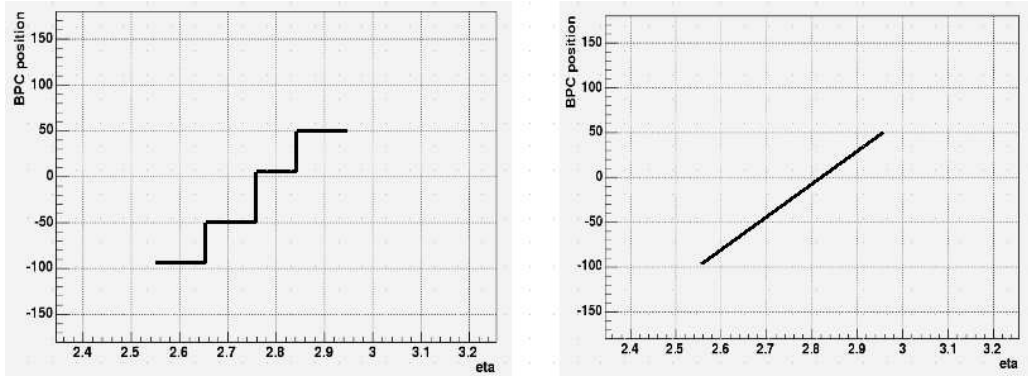


Figure 6.13: Difference between finite (Left) and infinite granularity (Right).

used to correct the barycenter position in order to calculate the η -direction resolution, as we have already done in the ϕ -case using a linear fit. We tried to fit our two histograms using the following function:

$$Y = par[0] \cdot atan(par[1] \cdot \eta - par[2]) - par[3] \quad (6.9)$$

with the following parameters meanings:

- $par[0]$ =scale factor
- $par[1]$ =factor that multiply the argument
- $par[2]$ =it parametrises the center of the cell
- $par[3]$ =shift factor

As we can see in Figure 6.14, the fit does not work equally well for all the BPCs, with the consequence that sometimes the distribution that we get is not perfectly gaussian.

6.2.1 η -resolution vs η

We follow the guidelines of the ϕ resolution, that is, using the same runs of an Y-scan, we plotted the σ for all the BPCs at different values of η . This time the result is worse and no clear behaviour or trend can be easily observed (Figure 6.15): the reason is the not so perfect *atan* fit for the S-shape histograms, so our value are a little range-dependent because of the not perfectly gaussian distribution. Anyway, a small rise of the σ is present as it was also on the equivalent ϕ plot and we are able to give an order of magnitude to this resolution.

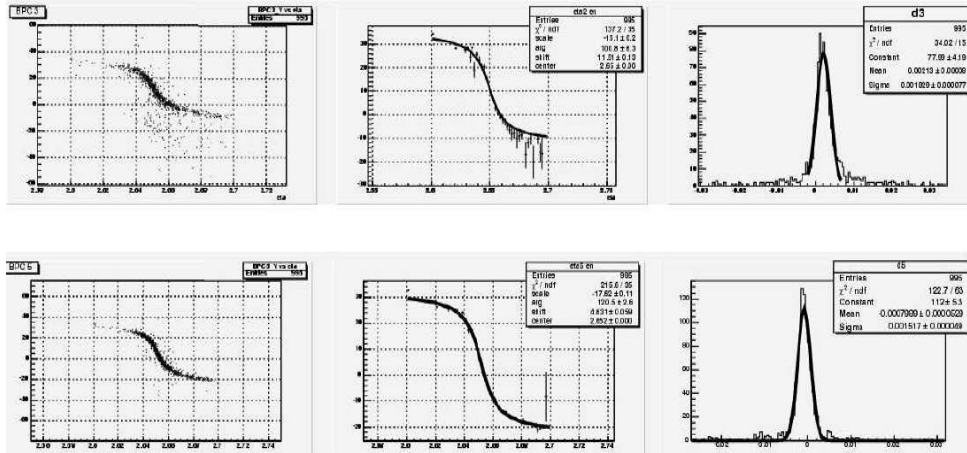


Figure 6.14: *Left:* S-shape correlation between BPC position and ϕ coordinate of the barycenter. *Middle:* the fit of these plot, using Formula 6.9 is not always perfect. *Right:* distribution of differences between measured values and fit values.

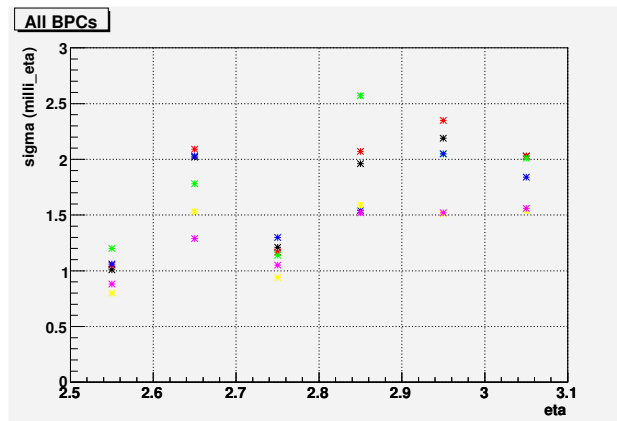


Figure 6.15: σ vs. η for all the BPCs. The linear rise with η is less clear than in the ϕ case. The BPC-colour relation is the same as in Figure 6.4

6.2.2 η -resolution at different energies

We go on following the analysis already done for the ϕ resolution; we performed the η resolution at different energies for a fixed cell, the same used in the previous section with exactly the same runs. Even in this case we compare two different fits: $\sigma = a/\sqrt{E} + \text{const}$ and $\sigma = a/E + \text{const}$. Even for the η -resolution we actually see that the latter fit works better (Figure

6.3. SUMMARY AND CONCLUSIONS FOR SPATIAL RESOLUTION.95

6.16 to Figure 6.19), especially for the BPC5 for which multiple scattering effects are negligible.

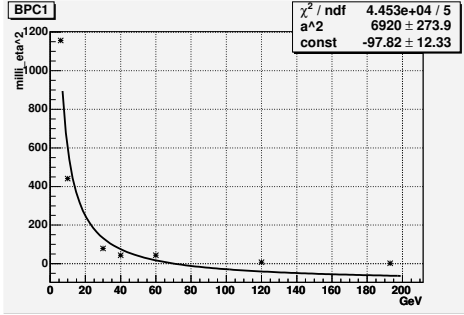


Figure 6.16: σ_{global}^2 for BPC1 in function of the energy.

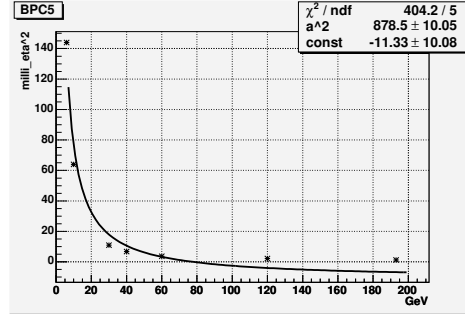


Figure 6.17: σ_{global}^2 for BPC5 in function of the energy.

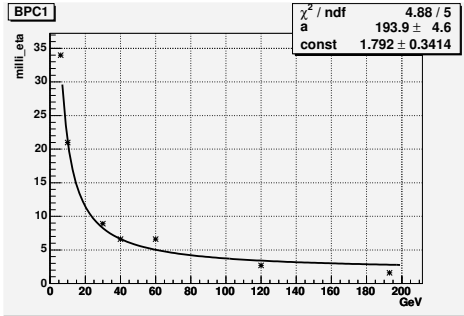


Figure 6.18: σ_{global} for BPC5 in function of the energy.

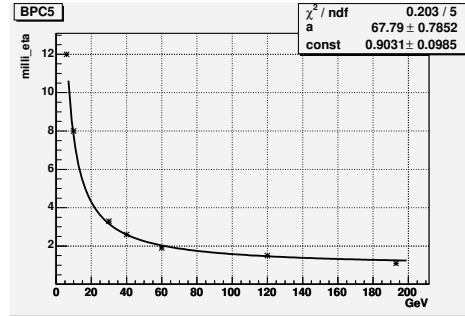


Figure 6.19: σ_{global} for BPC1 in function of the energy.

6.3 Summary and conclusions for spatial resolution.

We now summarize the most important results obtained in this chapter.

- ϕ -resolution: at a fixed energy (120 GeV) and varying η we have found a global resolution comprised between 1.5 *mrad* and 2.5 *mrad* for the BPC closest to the detector. The resolution get worse linearly with η . Instead the resolution varies with the energy following a $1/E$ curve.
- Intrinsic BPC resolution. The BPCs give a constant contribution to the resolution no matter the beam energy used. It is generally negligible

for energies smaller than 120 GeV. At this energy its contribution in Formula 6.1 is 4%.

- Contribution of Multiple Scattering. It strongly influences the measures taken using low energy beams and BPCs far from the detector. At 120 GeV and using BPC5 its contribution is negligible.
- η -resolution: using 120 GeV runs we obtained for BPC5 resolution values between $1 m\eta$ and $1.5 m\eta$.

Conclusions

This Diploma Thesis has been developed inside the ATLAS experiment: ATLAS is a detector that from the 2007 will take data in the proton-proton collider LHC at CERN. The goal of this thesis is a study of the performance in energy and position reconstruction, using electron beams, of the inner wheel of the electromagnetic end-cap calorimeter. Data of the Test Beam of autumn 2004 have been used, in order to be able to rapidly implement efficient and good quality reconstruction algorithms when the experiment will begin.

The first original part is dedicated to the study of the HV-Energy curve, that is, to the measured energy changes when we vary the potential applied to the calorimeter electrodes. These corrections will be important when it will not be possible to apply the nominal HV value. We found that we can fit our data using a power function $E = a \cdot HV^b$, obtaining a value for the b exponent of $b = 0.366 \pm 0.07$; this value is very close to the one obtained for the barrel and it shows that it depends only on the Liquid Argon properties.

We have then briefly analyzed the shape of the signal after the $RC - CR^2$ shaper and we found that the physical signal differs considerably from the theoretical one, probably because the theoretical signal come from barrel studies, where the liquid argon gap is constant. In the end cap the liquid argon gap is not constant and the effects of the accordion geometry have not been considered.

The study on the noise concerned especially the influence that it could have on the calorimeter response, comparing it with what has been obtained in Test Beam 2002. The noise of Test Beam 2004 has an amplitude slightly bigger than the previous one. Moreover we found a weak effect common to all the inner wheel, as the whole calorimeter undergo a common fluctuation.

The central part of this thesis concerns the HV corrections that has to be applied to get the most uniform response. In fact, to compensate the varying gap of liquid argon (and so the varying electric field experienced by the ionizing particles), a step varying potential has been applied. So, within each each HV sector, there is still a η -dependence to take in account and

that has to be corrected using formula 5.1. The α factors that minimize, for each HV sector, the range of the energy response are $\alpha = 0.55$ for the sector $2.5 < \eta < 2.8$ and $\alpha = 0.45$ for the $2.8 < \eta < 3.2$ one. After these corrections, that have to be applied cell by cell, we have an energy response constant to within the $\pm 2\%$ over the whole η range of the inner wheel.

All second order corrections (cluster corrections and other effects) have been absorbed using a third degree polynomial: after that our response has distribution with a σ of the order of 1%.

These results could be improved using the calibration ramp (that is, the coefficients that allow us to convert the ADC counts to nA) of 2004, but up to January 2006 there were some not well understood problem when we used it. For these reasons, and using the fact that setups and electronics of the two Test Beams are exactly the same, we performed our calculations with the calibration ramps of 2002.

Finally we analyzed the spatial resolution of the Inner-Wheel. Although having a good resolution was not a guideline in the construction of the inner wheel (its main goal is to measure the missing energy), a good evaluation of its spatial resolution will allow the Cracow ATLAS group to study the luminosity using a channel in which a pair of electrons is produced at a ϕ -angle of 180 in the high- η region.

For ϕ -resolution we found a value of 1.5 *mrاد* for the lowest η and 2.5 *mrاد* for $\eta=3.1$. Within this interval, the resolution grows almost linearly.

For the η -resolution the behaviour is less clear but the values obtained are between 1 and 1.5 *mη*.

Appendix A

Two methods for the signal reconstruction.

In this Appendix we will briefly describe two frequently used methods for the signal reconstruction [25].

A.1 Parabola Method

This signal reconstruction algorithm uses only 3 of the 5 samples stored in order to calculate the amplitude and the peak time of the signal. The strategy of this algorithm is to get some crude informations from the interpolations of these 3 samples and then to improve the results using *ad hoc* corrections.

Briefly, the Parabola method works as follow:

- the greatest samples and the two neighbours are interpolated using a parabolic function. The time of the maximum of the parabola is a first estimation of that parameter.
- To perform the corrections we use a signal shape that comes from a precise calibration signal. First of all we define the correlation between the peak value of the measured signal and the first crude time estimation. Then we calculate the ratio between the real amplitude of the reference signal and the maximum of the sampled signal at the same crude time value.
- The two previous corrections are performed only for a cell and extended to the whole calorimeter. The true value of the peak time is obtained by applying the first correction to the sampled signal, the maximal amplitude is calculated applying the second correction to the greatest sample stored.

This method is affected by some errors that will influence the analysis.

- all the corrections are performed for only one cell, so eventual ununiformities among the various cells
- the signals used as reference are calibration ones, so they differ significantly from the physical one.
- the maximal amplitude is obtained only from the sampling of the maximum, so it is very sensitive to fluctuations.

There is another reconstruction method based on a cubic interpolation of the samples stored. Essentially it works as the parabola one, with the only difference that the samples are interpolated using a third degree polynomial.

A.2 Optimal Filtering

The Optimal Filtering [24] is a way to determine the peak amplitude and the time of the sampled signals. Its fundamental characteristic is that it minimises the noise.

If we consider a signal of the generic shape:

$$f(t) = Ag(t - \tau) + n(t) \quad (\text{A.1})$$

where A is the signal amplitude, $g(t)$ the shape of the unitary signal and τ the delay with which the signal starts with respect to the sampling time. The function $n(t)$ represents the noise that is superposed to the signal during the data acquisition. If τ is small with respect to t , we can expand the previous expression and get

$$f(t) \equiv A[g(t) - \tau g'(t)] + n(t) \quad (\text{A.2})$$

where $g'(t)$ is the first derivative of the signal shape $g(t)$. Therefore the signal becomes

$$S_k = A(g_k - \tau g'_k) + n_k \quad (\text{A.3})$$

with the index k that represents the value of the functions at the sampling time t_k .

The noise is supposed to be a zero mean value function and its autocorrelation function is supposed to be known

$$\begin{aligned} \langle n(t) \rangle &= 0 \\ \langle n_i n_j \rangle &= R_{ij} \end{aligned} \quad (\text{A.4})$$

The informations on the peak amplitude and the start time of the signal are obtained from linear combinations of the N samples $\{S_1 \dots S_N\}$. The coefficients a_k and b_k are chosen for the following equations

$$\begin{aligned} U &= \sum_{k=1}^N a_k S_k \\ V &= \sum_{k=1}^N b_k S_k \end{aligned} \quad (\text{A.5})$$

in order to minimise σ_U and σ_V with the conditions

$$\langle U \rangle = A \Rightarrow \sum_{k=1}^N a_k g_k = 1, \quad \sum_{k=1}^N a_k g'_k = 0 \quad (\text{A.6})$$

$$\langle V \rangle = A\tau \Rightarrow \sum_{k=1}^N b_k g_k = 0, \quad \sum_{k=1}^N b_k g'_k = -1 \quad (\text{A.7})$$

From eq.(A.4) we get that

$$\sigma_U^2 = \text{Var}[U] = \sum_{ij} a_i a_j R_{ij} \quad (\text{A.8})$$

$$\sigma_V^2 = \text{Var}[V] = \sum_{ij} b_i b_j R_{ij} \quad (\text{A.9})$$

We can minimise the σ_U^2 and σ_V^2 using the technique of the lagrangian multipliers. We find two set of equations; the first for the peak amplitude:

$$\begin{aligned} 0 &= \frac{\partial}{\partial a_k} \left[\frac{1}{2} \sum_{ij} a_i a_j R_{ij} - \lambda \sum_i a_i g_i - \mu \sum_i a_i g'_i \right] \\ &= \sum_i a_k R_{ij} - (\lambda g_k - \mu g'_k) \end{aligned} \quad (\text{A.10})$$

$$a_i = \lambda \sum_k R_{ik}^{-1} g_k - \mu \sum_k R_{ik}^{-1} g'_k \quad (\text{A.11})$$

$$\lambda = \frac{Q_2}{\Delta} \quad \mu = -\frac{Q_3}{\Delta} \quad (\text{A.12})$$

the second for timing informations:

$$\begin{aligned} 0 &= \frac{\partial}{\partial b_k} \left[\frac{1}{2} \sum_{ij} b_i b_j R_{ij} - \rho \sum_i b_i g_i - \sigma \sum_i b_i g'_i \right] \\ &= \sum_i b_k R_{ij} - (\rho g_k - \sigma g'_k) \end{aligned} \quad (\text{A.13})$$

$$b_i = \rho \sum_k R_{ik}^{-1} g_k - \sigma \sum_k R_{ik}^{-1} g'_k \quad (\text{A.14})$$

$$\rho = \frac{Q_3}{\Delta} \quad \sigma = -\frac{Q_1}{\Delta} \quad (\text{A.15})$$

using

$$Q_1 = \sum_{ij} g_i g_j R_{ik}^{-1} \quad Q_3 = \sum_{ij} g_i g'_j R_{ik}^{-1} \quad (\text{A.16})$$

$$Q_2 = \sum_{ij} g_i^j g'_j R_{ik}^{-1} \quad \Delta = Q_1 Q_2 - Q_3^2 \quad (\text{A.17})$$

Appendix B

Riassunto

B.1 Il Modello Standard

La fisica subnucleare moderna descrive il mondo in termini di particelle: la materia è composta da particelle elementari e anche le loro interazioni sono interpretate in termini di scambio di altre particelle elementari. La teoria che descrive queste interazioni e i cui risultati sono confermati dagli esperimenti ad un livello di precisione che nessun'altra teoria aveva dato è chiamata Modello Standard.

Le interazioni mediate dalle particelle di campo sono le seguenti:

- **elettromagnetica**: la particella di campo che media questo tipo di interazioni è il fotone, particella di spin 1 e priva di massa. Tali interazioni riguardano tutte le particelle dotate di carica elettrica.
- **debole**: è la forza all'origine dei decadimenti β , mediata da bosoni vettori massivi W^+ , W^- and Z^0 .
- **forte**: è la forza che mantiene uniti i costituenti dei nuclei ed è mediata da 8 bosoni privi di massa chiamati *gluoni*.
- **gravitazionale**: agisce tra tutte le particelle dotate di massa. La particella responsabile di tale interazione, il *gravitone*, non è ancora stata scoperta, ma dovrebbe avere spin 2.

In realtà il Modello Standard ha unificato solo le prime tre interazioni ma non descrive la gravitazione; l'unificazione del Modello Standard con una teoria quantistica della gravitazione rappresenta una delle sfide più affascinanti nel campo della fisica teorica.

Daremo ora una breve descrizione degli elementi del Modello Standard. Le particelle fondamentali che compongono la materia (*matter particles*) sono

chiamate fermioni poiché seguono la statistica di Fermi-Dirac. Hanno spin $1/2$ e possono essere suddivisi in *leptoni* e *quark*. Ciascuna di esse possiede un'antiparticella, cioè una particella della stessa massa e spin ma con carica elettrica opposta.

Le particelle di campo (*field particles*) hanno invece spin intero e seguono la statistica di Bose-Einstein. Quando mediano le interazioni esse sono particelle *virtuali*: processi come quello di Figura 1.1 possono aver luogo anche ad energie minori di quelle necessarie alla creazione del bosone Z^0 , dal momento che la particella viene creata e annichilita in un intervallo di tempo minore di $\Delta E/\hbar$, preservando così la conservazione della massa.

Il Modello Standard è una Teoria Quantistica di Campo basata sull'invarianza di *gauge* rispetto al gruppo $SU(2)_L \times U(1)_Y$ per quanto riguarda il settore elettrodebole e rispetto al gruppo $SU(3)_C$ per il settore delle interazioni forti.

L'approccio moderno alle teorie quantistiche di campo è quello di prendere come requisito iniziale l'invarianza rispetto a trasformazioni di fase locale; così facendo, si deve introdurre necessariamente un campo di gauge accoppiato al campo di materia, sostituendo la derivata ordinaria con una covariante (formule 1.5 e 1.6).

Il Modello Standard ha avuto numerosi successi:

- È una teoria quantistica di campo rinormalizzabile che permette l'unificazione delle interazioni elettromagnetiche, deboli e forti.
- Mediante il *meccanismo di Higgs* risolve il problema dell'assegnazione delle masse ai bosoni vettori e ai fermioni.
- Nel settore elettrodebole tutte le sue predizioni differiscono dai dati sperimentali per meno dello 0.1%.

Tuttavia presenta alcuni problemi non ancora risolti:

- Il bosone di Higgs non è stato ancora osservato. La sua scoperta è uno degli obiettivi principali dell'LHC.
- In una Teoria della Grande Unificazione le costanti di accoppiamento *running* delle interazioni elettromagnetiche, deboli e forti non convergono.
- Il Modello Standard si basa su 19 parametri e non c'è nessuna spiegazione per il fatto che effettivamente siano 19.
- Il Modello Standard non spiega la massa del neutrino.

Questi problemi ancora irrisolti conducono a pensare che il Modello Standard sia solo un'approssimazione di una teoria ancora più fondamentale.

B.2 L'esperienza ATLAS all'LHC

Il collisionatore adronico LHC sarà l'acceleratore per la fisica delle alte energie in cui pacchetti di protoni subiranno collisioni ad energie del centro di massa mai raggiunte prima, pari a 14 TeV , con una luminosità di $10^{34} \text{ cm}^{-2} \text{ sec}^{-1}$.

Uno degli obiettivi primari di questo acceleratore è la scoperta del bosone di Higgs, l'unica particella del Modello Standard non ancora osservata. Si cercherà inoltre di osservare le particelle supersimmetriche e si effettueranno misure di precisione sulla violazione di CP e sul Modello Standard in generale.

È stato scelto un collisionatore adronico, contrariamente a LEP, a causa della radiazione di sincrotrone. Infatti le particelle cariche, quando sono accelerate, emettono radiazione. Osservando le formule 2.1 e 2.2, si comprende che, a parità di energia, particelle più pesanti hanno una minore perdita di energia.

Le interazioni tra pacchetti di protoni sono più complicate di quelle studiate a LEP (elettroni-positroni) poiché i protoni non sono particelle elementari, bensì sono formati da quarks e gluoni che si muovono liberamente all'interno di essi (fenomeno della *libertà asintotica*) ma che non esistono come particelle isolate.

Il fenomeno della libertà asintotica ci impedisce di conoscere esattamente la frazione di momento dell'adrone portato dal singolo quark. Per processi inclusivi, l'energia e il momento possono essere scritti come nelle formule 2.3 e 2.4. Nella 2.4 si osserva che la *rapidità* è invariante sotto trasformazioni di Lorentz: è quindi vantaggioso usare la rapidità (o la pseudo-rapidità nel caso di particelle ultra-relativistiche) perché ci permette di ottenere sezioni d'urto Lorentz-invarianti. Inoltre è una quantità che può essere sempre misurata, anche quando la massa e il momento delle particelle non sono noti.

B.2.1 Il rivelatore ATLAS

Il rivelatore ATLAS è composto da numerosi sotto-rivelatori con obiettivi differenti. ATLAS ha simmetria cilindrica con l'asse parallelo al fascio di particelle.

Partendo dall'asse di simmetria e seguendo la coordinata radiale troviamo le seguenti componenti:

- *Rivelatore interno*. Il suo compito è quello di ricostruire le traiettorie delle particelle cariche nella regione più vicina al punto di interazione. È composto da rivelatori di vertice a pixel, rivelatori a semiconduttore e da *transition radiation trackers*, questi ultimi per la misura del tempo di deriva.

- *Solenoid centrale.* Produce il campo magnetico necessario per curvare le traiettorie delle particelle cariche e determinare quindi la loro carica elettrica e il loro momento trasverso. Tale campo magnetico avrà un'intensità di 2 Tesla.
- *Calorimetri.* I calorimetri avranno un ruolo cruciale all'LHC dal momento che la loro risoluzione migliora con l'energia mentre quella degli altri sotto-rivelatori peggiora. In Figura 2.7 vediamo i tre tipi di calorimetri presenti: quello elettromagnetico (composto da una corpo centrale e due calorimetri tappo), quello adronico e il calorimetro in avanti. Il calorimetro elettromagnetico verrà analizzato più in dettaglio nella sezione B.2.2.
- *Spettrometro a muoni.* È situato nella parte più esterna di ATLAS e ha il compito di identificare i muoni prodotti nelle interazioni e di misurare la loro energia e le loro traiettorie. È composto da *camere di precisione* e da *camere di trigger*: le prime hanno un'ottima risoluzione spaziale ma una risoluzione temporale più grande dell'intervallo di tempo a cui avvengono le interazioni. Per questo motivo sono accoppiate alle camere di trigger che selezionano gli eventi in cui sono presenti dei muoni.

B.2.2 Calorimetro Elettromagnetico

Il calorimetro elettromagnetico deve avere i seguenti requisiti:

- La maggior copertura possibile in pseudorapidità, necessaria per l'osservazione di processi quali $H \rightarrow \gamma\gamma$ e $H \rightarrow 4e$.
- Un'eccellente risoluzione energetica tra 10 e 3000 GeV. Per i due canali fondamentali per l'osservazione dell'Higgs (elencati al punto precedente) la risoluzione deve essere al massimo dell'1%. Per un calorimetro la risoluzione è generalmente espressa dalla relazione

$$\Delta E = b \oplus a\sqrt{E} \oplus cE \quad (\text{B.1})$$

in cui b è il termine relativo al rumore, a il termine di campionamento dovuto alle fluttuazioni dell'energia depositata dallo sciame elettromagnetico nel calorimetro. Infine, c è il termine costante dovuto a non-uniformità nella costruzione. Ad alte energie c diventa il contributo dominante alla risoluzione e per questo motivo deve essere dell'ordine dello 0.7%.

- Uno spessore di almeno $24 X_0$ (lunghezze di radiazione) per contenere l'energia degli sciame elettromagnetici.
- Ottima risoluzione spaziale e capacità di distinzione tra *jet* dovuti ad elettroni e *jet* dovuti a fotoni.

I calorimetri si possono suddividere in calorimetri *a campionamento* e in calorimetri *omogenei*. Nei primi vi è un'alternanza di strati di materiale assorbente e di materiale attivo, nel quale le cariche elettriche generate dalla ionizzazione dell'argon liquido sono raccolte dagli elettrodi; quelli omogenei sono composti da un solo materiale che funge allo stesso tempo da assorbitore e da materiale attivo. Questi ultimi hanno migliore risoluzione energetica ma bassa risoluzione spaziale.

Il calorimetro elettromagnetico di ATLAS è un calorimetro a campionamento. Le ragioni di tale scelta sono principalmente economiche: con energie dell'ordine del TeV , un calorimetro omogeneo sarebbe stato troppo grande. Tuttavia con un calorimetro a campionamento misuriamo solo una frazione dell'energia, chiamata *frazione di campionamento* (Formula 2.11).

Il calorimetro elettromagnetico di ATLAS è composto da un corpo centrale (*barrel*) che copre la regione di pseudo-rapidità $|\eta| < 1.45$ e da due tappi (*end caps*) composti da due ruote coassiali che coprono rispettivamente la regione ad $1.35 < |\eta| < 2.5$ e quella a $2.5 < |\eta| < 3.2$.

Calorimetro *barrel* Il calorimetro barrel è un rivelatore in cui gli assorbitori di piombo e il materiale attivo (argon liquido) sono disposti con una geometria a fisarmonica (Figura 2.9 e Figura 2.18) che permette una simmetria in ϕ senza interruzioni. In Tabella 2.10 osserviamo che sia nel barrel che nell'end cap lo spessore degli assorbitori varia in funzione della pseudo-rapidità per ottimizzare le performance del calorimetro in risoluzione energetica.

Il barrel è suddiviso in tre strati (*samplings*) longitudinali:

- Il primo ha uno spessore di $6 X_0$ ed è formato da strisce sottili nella direzione η . Ha il ruolo di identificare la direzione dello sciame elettromagnetico con grande precisione e di determinarne la sua struttura tridimensionale. Ha una granularità pari a $\Delta\eta 0.0031 \times \Delta\phi 0.025$.
- Il secondo strato ha uno spessore di $18 X_0$ e raccoglie la maggior parte dell'energia dello sciame elettromagnetico. Ha granularità pari a 0.025×0.025 che permette di distinguere gli sciame elettromagnetici da quelli prodotti da ioni.

- Il terzo sampling ha spessore pari a $12 X_0$ ed è dotato di una granularità meno fine, dal momento che non vi è più la necessità di determinare la direzione dello sciame ma solo quella di raccogliere l'energia rimasta.

Calorimetro EM End-Cap ad ATLAS

Esattamente come il calorimetro barrel, il calorimetro end cap consiste in strati di assorbitore di piombo intervallati da argon liquido, utilizzando sempre una geometria a fisarmonica. L'end cap ha un raggio esterno di 2077 mm ed è situato nell'apposito criostato ad una distanza di 3641 mm dal punto di interazione.

Come già detto in precedenza, l'end cap è costituito da due ruote coassiali e concentriche: l'esterna copre la regione $1.35 < |\eta| < 2.5$ mentre quella interna (di cui lo studio delle performance sarà l'argomento principale di questa tesi) copre la regione $2.5 < |\eta| < 3.2$. La ruota esterna dispone di 768 assorbitori e 768 elettrodi mentre quella interna solamente 256; ogni assorbitore della ruota interna è allineato con uno della ruota esterna.

Per mantenere la geometria a fisarmonica in questa regione, gli assorbitori sono stati disposti a raggiera con le pieghe della fisarmonica lungo la direzione del fascio di particelle. Per assicurare una buona risposta azimutale, lo spessore combinato dell'argon liquido e degli assorbitori che viene attraversato dalle particelle deve essere indipendente da ϕ ; dal momento che lo spessore dell'argon liquido varia col raggio, è necessario variare l'ampiezza delle pieghe dell'assorbitore e anche l'angolo che formano tra di loro. Per ragioni tecniche tale angolo deve essere compreso tra 60 e 120 gradi: ciò limita a 3 il rapporto tra raggio esterno e interno di ciascuna ruota. Questa è la ragione principale per l'utilizzo di due ruote concentriche, non essendo possibile coprire l'intervallo in η con una sola struttura a fisarmonica.

Il picco della corrente generata dalle cariche raccolte può essere espresso come in Formula 2.13. Per un campo elettrico costante e quindi per una velocità di deriva degli elettroni costante, la dipendenza da η di f_{samp} e quella di g tendono ad annullarsi reciprocamente. Tuttavia per una migliore compensazione di queste due variabili, e quindi per una risposta più uniforme, si dovrebbe variare in maniera continua il campo elettrico in funzione di η , poiché la velocità di deriva è una funzione del campo elettrico ($v_d \propto E^b$, con $b \sim 0.3$). Dal momento che E dipende dal potenziale applicato agli elettrodi, si arriva alla Formula 2.14.

Per avere un fattore di conversione tra corrente ed energia che sia indipendente da η , il potenziale dovrebbe variare in maniera continua, come detto in precedenza; tuttavia, per ragioni tecniche ed economiche viene usato un potenziale costante su piccoli intervalli di η (Figura 2.17). In seguito

l'energia ricostruita dovrà essere corretta per ogni settore di alta tensione: tali correzioni sono la parte centrale di questa tesi.

Per ciò che concerne granularità e campionamento, la ruota esterna ha caratteristiche molto simili a quelle del barrel. La ruota interna invece è costituita da solo due sampling aventi una granularità molto meno fine poiché il suo obiettivo primario non è l'averne una buona risoluzione spaziale bensì la misura dell'energia mancante dei vari eventi.

B.3 Test Beam

Nel Test Beam del 2004 è stato posizionato in uno dei criostato un ottavo della ruota completa dell'end cap elettromagnetico (EMEC) assieme a due moduli di quello adronico (HEC), successivamente riempito di argon liquido alla temperatura di 89.9 K. Nelle Figure 2.20 e 2.22 possiamo vedere il *setup* completo del Test Beam con i vari sotto rivelatori usati per fornire un segnale di trigger e per ottenere la traiettoria delle particelle del fascio.

Per ridurre il materiale di fronte al calorimetro, il criostato ha una finestra circolare in cui lo spessore della parete è notevolmente ridotto e tramite una schiuma a bassa densità particolare è stato possibile togliere l'argon liquido da tale regione.

B.3.1 Elettronica di lettura e calibrazione

La carica generata da una particella ionizzante che attraversa la regione attiva del calorimetro viene raccolta grazie al potenziale applicato tra elettrodo e assorbitore. Il segnale che si ottiene ha una forma triangolare.

Il calorimetro di ATLAS non ha un guadagno interno, quindi il segnale misurato è direttamente proporzionale alla carica raccolta. Il segnale generato nel gap di argon liquido viene letto dagli elettrodi e inviato alle carte sommatrici (*summing board*) dove vengono sommati i segnali degli elettrodi appartenenti allo stesso canale di lettura.

Le carte sommatrici sono raggruppate dalle carte madri secondo uno schema 2×2 . Il segnale viene poi inviato all'elettronica di lettura situata all'esterno del criostato: qui un pre-amplificatore, per ridurre l'influenza del rumore, amplifica il segnale che viene successivamente elaborato da un formatore $CR - RC^2$ (Figura 2.23). Il segnale dopo la formatura viene campionato ogni 25 *nsec*, alla frequenza a cui si hanno le interazioni fra pacchetti di protoni, e viene memorizzato temporaneamente in memorie analogiche in attesa della decisione presa dal trigger di livello 1. Se tale segnale supererà

le selezioni del *trigger*, sarà amplificato e cinque punti della parte positiva saranno digitalizzati e memorizzati.

Poiché solo 5 punti della curva del segnale vengono memorizzati, diventa fondamentale disporre di metodi molto precisi per la ricostruzione dell'energia: i più importanti sono il *metodo della parabola* e quello dell'*optimal filterings*. In generale, la tipica procedura per la ricostruzione dell'energia è la seguente:

- Calcolo del piedistallo, ossia il valore in conteggi ADCs quando non vi è alcun input.
- Sottrazione del piedistallo da tutti i campionamenti
- Calcolo dell'ampiezza e della posizione nel tempo per ogni evento usando o un'interpolazione cubica, o il metodo della parabola o quello dell'optimal filtering.
- Conversione in nA dei valori in uscita espressi in conteggi ADC .

B.4 Curva HV-Energia e forma del segnale

La prima parte originale di questo lavoro concerne lo studio della curva dell'energia ricostruita in funzione del valore della tensione applicata agli elettrodi per verificare che abbia lo stesso comportamento in tutto il calorimetro elettromagnetico (per questo motivo abbiamo paragonato i nostri risultati a quelli in [10]).

Il primo passo è stato trovare l'andamento dell'energia ricostruita a seconda del valore del potenziale applicato. Usando il valore nominale di alta tensione, l'energia ricostruita del fascio di elettroni sarà l'energia effettiva del fascio.

L'energia di ogni evento è stata calcolata usando un *cluster* di 9 celle per minimizzare l'influenza del rumore elettronico che domina l'output delle celle lontane dal punto in cui il fascio colpisce il rivelatore; per ogni evento si è trovata la cellula baricentro usando le formule in 3.1 e in seguito sono state prese le 8 celle che la circondano. È ragionevole prendere un cluster di solo 9 celle perché la granularità dell'end cap è di 0.1 in η e 0.1 in ϕ .

Tuttavia ciò non è sufficiente per ottenere misure precise dell'energia degli elettroni nel fascio: senza selezioni (*cuts*) appropriate sul valore minimo di energia che le celle devono registrare. Senza tali imposizioni verrebbe considerata l'energia di tutti gli eventi riconducibili a pioni e muoni, che depositano nell'EMEC solo una piccola quantità della loro energia (Figure 3.2 e 3.3).

Per svolgere ogni tipo di analisi diventa indispensabile un'accurata "pulizia" del fascio di particelle per evitare che la nostra analisi sia influenzata da eventi relativi a muoni e pioni: per questo motivo sono stati applicati cut su rivelatori che fanno da trigger sul segnale e infine un cut per far sì che ogni particella analizzata rilasci nell'EMEC un'energia maggiore di quella rilasciata nell'HEC (Figure 3.5, 3.6 e Tabella 3.1).

B.4.1 Fit della curva HV-Energia

Le prese dati (*run*) analizzate riguardavano fasci di elettroni che colpivano il rivelatore in due punti appartenenti a due settori di alta tensione differenti. Applicati i vari tagli a tutte le run, abbiamo cercato di fittare le energie trovate utilizzando la funzione $E = a \cdot HV^b$.

In principio abbiamo tenuto le run incidenti nella parte inferiore del rivelatore separate dalle altre; fittando la curva data dai valori di tali run abbiamo ottenuto il grafico in Figura 3.7. Se la curva ottenuta dipendesse solo dalle proprietà dell'argon liquido, come ipotizziamo, dovremmo ottenere un fit ragionevole anche per le run della parte superiore del rivelatore mantenendo lo stesso esponente b e fittando solo a . Il risultato ottenuto è piuttosto soddisfacente ma può essere notevolmente migliorato escludendo dal fit le run effettuate con un potenziale minore di 400 V: a potenziali più bassi il numero di eventi che passa i tagli applicati è molto basso e ciò impedisce di avere statistiche soddisfacenti.

Nella Tabella 3.2 abbiamo confrontato i valori dell'esponente b da noi ottenuti e quelli trovati per il barrel trovando un accordo più che soddisfacente.

B.4.2 Forma del Segnale

Successivamente abbiamo studiato la forma del segnale dopo la formatura $CR-RC^2$, confrontandola con quella teorica. In Figura 3.16 possiamo vedere a destra come la forma del segnale cambi al variare del tempo di deriva, mentre Formula 3.3 dimostra come il tempo di deriva sia legato alla tensione applicata agli elettrodi. Osservando i segnali fisici misurati, vediamo che differiscono da quelli teorici:

- L'*undershoot* (ovvero la parte del segnale che segue quella esponenziale) non è piatto e la risalita del segnale non è ripida ma tende a confondersi con l'*undershoot*.
- La relazione tra tempo di deriva e potenziale non è esattamente corrispondente a quella attesa.

Abbiamo formulato varie ipotesi per spiegare questo comportamento anomalo; la più probabile riguarda la struttura a fisarmonica dell'EMEC. Infatti nelle regioni dove sono situate le pieghe degli assorbitori, la distanza tra gli elettrodi è maggiore e quindi le cariche create dalla ionizzazione sono esposte ad un campo elettrico più debole; la curva di ionizzazione che teoricamente dovrebbe essere triangolare, diventa un'interpolazione di curve triangolari con tempi di deriva e ampiezze differenti. La curva risultante ha andamento esponenziale e dopo la formatura ciò comporta un undershoot non piatto (Figura 3.20).

B.5 Rumore

È stata effettuata in seguito un'analisi sul rumore per osservare quanto possa influenzare le misure di eventi fisici.

Il primo test effettuato riguardava la natura gaussiana del rumore, per verificare che effettivamente fosse caratterizzato solo da fluttuazioni statistiche. Per un rumore puramente gaussiano dovremmo ottenere che lo scarto quadratico medio (RMS) della distribuzione della media dei 32 campionamenti di ogni evento sia uguale al valor medio della distribuzione degli RMS di ogni evento diviso la radice quadrata di 32 (vedi Formula 4.1) [22]. Invece, come si può osservare in figura 4.1, ci sono celle che presentano una marcata differenza tra questi due valori.

In principio abbiamo ipotizzato un'origine *hardware* per questo strano comportamento, ma le celle che mostrano questa deviazione dal comportamento gaussiano appartengono a carte sommatrici e a carte di alta tensione differenti.

Un'altra sua possibile origine potrebbe essere la presenza di un rumore a bassa frequenza che influenza la distribuzione della media dei 32 campionamenti lasciando invariata quella degli RMS. Effettivamente si può osservare nelle figure 4.4 e 4.5 un aumento, comune a tutto il rivelatore, di tale differenza .

Un modo per evidenziare questo rumore a bassa frequenza è quello di mettere la media dei 32 campionamenti in funzione della pendenza della regressione lineare del segnale [15]: la presenza di tale rumore disporrebbe i punti su una circonferenza. Tuttavia, la figura 4.6 di destra mostra una distribuzione uniforme per tutte le celle della ruota interna dell'EMEC.

Un'ulteriore analisi svolta riguarda la ricerca di eventuali fenomeni di *cross talk*: mettendo in relazione la media dei campionamenti di una cella con lo stesso valore di un'altra cella. Si osserva una forte correlazione tra tutte le celle, come se l'intero calorimetro subisca le stesse fluttuazioni.

Infine abbiamo confrontato i nostri risultati con quelli ottenuti per il test beam del 2002, osservando che quest'ultimo ha un rumore piú uniforme al variare di η e ϕ ma una differenza di 2 conteggi ADC tra il primo *sampling* e il secondo. Il test beam del 2004 presenta un rumore molto simile su entrambi i *sampling* ma molto meno uniforme.

B.6 Correzioni di Alta Tensione

La correzione piú importante riguarda la risposta del calorimetro al variare di η , dal momento che nell'EMEC il gap di argon liquido diminuisce all'aumentare della pseudorapidità e quindi si dovrebbe applicare un potenziale che vari in maniera continua per bilanciare tale effetto. Come già detto in precedenza, il potenziale varia su intervalli finiti: sette settori di alta tensione per la ruota esterna dell'EMEC e solo due per quella interna.

Questa divisione lascia una dipendenza da η che dovrà essere corretta usando la Formula 5.1. Spieghiamo brevemente il significato dei vari parametri:

- β è un fattore di scala in teoria prossimo a 1.
- Si può dimostrare che il fattore α è uguale, al prim'ordine, alla somma della frazione di campionamento e dell'esponente b della curva HV-Energia (formule da 5.2 a 5.11).

Per il calcolo di tali correzioni sono stati utilizzati run corrispondenti ad uno scan verticale nel centro del rivelatore con un fascio di elettroni di 120 *GeV*. L'energia di queste run è stata ricostruita usando un'interpolazione cubica ed il suo valore calcolato ricorrendo al cluster di 9 celle già usato in precedenza.

Osservando il grafico in Figura 5.3 in cui abbiamo posto l'energia in funzione della pseudorapidità, possiamo immediatamente notare due caratteristiche inattese: l'intervallo in energia è estremamente ampio (l'energia varia del 40%), soprattutto se paragonato al Test Beam del 2002. Inoltre, se consideriamo Formula 5.1, i punti a $\eta = 2.65$ non dovrebbero subire correzioni (visto che, a priori, il fattore β vale circa 1) ma la loro energia non è affatto vicina ai 120 *GeV*.

Per verificare che questo comportamento non sia dovuto a celle mal funzionanti, abbiamo ripetuto la stessa analisi per uno scan verticale a $X=-60$ e per run in cui il fascio colpisce il rivelatori in celle differenti. Sovrappo- nendo i vari risultati ci si rende conto di come all'origine dell'ampiezza del range di energia non ci siano celle non funzionanti ma piuttosto ricostruzioni o calibrazioni non corrette (5.6).

B.6.1 Correzioni a livello di celle

Se proviamo a correggere i grafici 5.3 e 5.6 con valori dei ragionevoli per α e β ($\alpha = 0.5$, $\beta = 1$), vediamo che la pendenza della retta lungo la quale si trovano i punti, nei rispettivi settori di alta tensione, diminuisce ma non a sufficienza: siamo lontani dall'aver una risposta uniforme, soprattutto nel settore di alta tensione $2.5 < \eta < 2.8$. Per ottenerla dovremmo utilizzare valori di α privi di significato fisico dal momento che α dovrebbe essere compreso tra 0.4 e 0.7.

Per capire se l'origine del problema sia nella ricostruzione dell'energia, al posto dell'interpolazione cubica abbiamo utilizzato versioni semplificate di optimal filterings: con questi la situazione migliora leggermente, le pendenze delle rette diminuiscono, soprattutto nel settore $2.8 < \eta < 3.2$ per il quale in alcuni casi troviamo valori di α compatibili con quelli attesi. Tuttavia per l'altro settore di alta tensione i valori ottenuti non hanno significato fisico.

Nemmeno con la nuova versione degli optimal filterings (portata a termine nel settembre 2005) la situazione è migliorata. La spiegazione rimanente per un intervallo di energia così ampio sembrerebbe risiedere quindi in un errore nella calibrazione. Tale ipotesi è supportata dal fatto che anche nel TB 2002, prima di implementare la corretta calibrazione, c'era una situazione simile alla nostra (Figura 5.10).

Infatti, con la nuova calibrazione [19] la situazione migliora immediatamente: l'intervallo di energia per i vari *scan* analizzati è minore del 20% già prima di qualsiasi correzione (Figura 5.11 e 5.12). Bisogna tuttavia osservare che:

- Prese dati con baricentro nella cella $2.5 < \eta < 2.6$ hanno energie più basse di quanto atteso, ma ciò può essere spiegato col fatto che, essendo celle all'estremità del rivelatore, non è possibile ricostruire un cluster di 9 celle, con conseguente perdita di energia.
- I punti in $2.9 < \eta < 3.0$ non seguono la retta data dalle altre run dello stesso settore di alta tensione.
- in Figura 5.14 si può osservare che l'energia delle run con fascio puntato sugli *standard points* I e J è molto più bassa: la differenza diventa ancora più evidente sovrapponendo i risultati dei vari scan.

In principio si è supposto che quest'ultimo problema fosse dovuto a questioni di guadagno. Infatti, in [19] notiamo che in caso di guadagno MEDIO alcuni canali non sono perfettamente calibrati, e avendo le run utilizzate un fascio ad alta energia, era possibile che il segnale fosse stato amplificato con guadagno MEDIO. Tuttavia analizzando uno scan a X-120 (zona in cui si

trova il punto I) a 60 GeV si riscontra lo stesso problema ad ogni η . Questo esclude che il problema sia causato dal guadagno.

Abbiamo quindi provato ad usare la calibrazione del TB del 2002: avendo i due TB la stessa elettronica e lo stesso set-up dovremmo ottenere gli stessi valori. Invece, con la calibrazione del 2002, questo problema scompare (Figura 5.16) dandoci una risposta molto simile in tutto il calorimetro (Figure 5.18 e 5.19).

B.6.2 Calcolo di α e β

I migliori valori di α per i due settori di alta tensione, che danno la risposta più uniforme possibile, sono quelli che minimizzano la σ della distribuzione di punti dell'istogramma in Figura 5.18. Bisogna ricordare che i due valori di α non sono completamente indipendenti dal momento che i cluster contenenti le celle centrali del calorimetro subiscono le correzioni di entrambi i valori. Ciò contribuisce ad alterare l'uniformità della risposta e si dovrà tenerne conto nelle correzioni del second'ordine.

La strategia seguita per ottenere tali valori è stata quella di fissare α_1 e variare α_2 fino a trovare un minimo nella σ della distribuzione di punti. Successivamente si è fissato tale valore di α_2 facendo variare α_1 trovando un nuovo minimo. Iterando questo processo i valori di α convergevano verso quelli indicati nella Tabella 5.4. Tuttavia cambiando del 10-15% questi valori non si hanno variazioni drammatiche nella risposta in energia.

Il termine β è stato invece calcolato facendo semplicemente la media, per ogni settore di alta tensione, del contenuto dei vari *bin* dell'istogramma in Figura 5.18

B.6.3 Correzioni a livello di cluster

Abbiamo in seguito considerato correzioni del secondo ordine, al livello del cluster. Infatti, considerando la misura finita delle celle dell'EMEC, sciami il cui baricentro non è ben al centro della cellula centrale del cluster saranno contenuti in maniera meno efficace, con conseguente perdita di energia. Dopo aver applicato le correzioni a livello di celle ci aspettiamo un andamento parabolico della risposta energetica, con un massimo nel centro della cella.

Già in Figura 5.24 è evidente come l'andamento parabolico sopra citato valga solo per alcune celle. Altri effetti, come la combinazione dei due α o come il fatto di non poter creare cluster di 9 celle, alterano l'uniformità della risposta allo stesso ordine di grandezza. L'impossibilità di trovare un'andamento parabolico centrato nel mezzo di ogni cella è evidenziata in Figura 5.26.

Correzioni paraboliche possono essere implementate nella ruota esterna, dotata di granularità più fine; per quanto riguarda la ruota interna, abbiamo riscontrato lo stesso comportamento anche nel TB del 2002 (Figura 5.25).

Cercare di separare tutti i vari contributi del secondo ordine non avrebbe portato grandi vantaggi, perciò abbiamo optato per assorbire i vari contributi correggendo la risposta in energia con un fit dato da un polinomio di terzo grado (Figura 5.27).

Usando i parametri di questo fit, abbiamo costruito un istogramma monodimensionale per ogni scan analizzato, con la differenza tra il valore di energia calcolato e quello dato dal fit. Per tutti gli scan si trova una distribuzione di punti con *RMS* dell'ordine al massimo dell'1% (da Figura 5.28 a Figura 5.31).

B.7 Risoluzione Spaziale

L'ultimo capitolo di questa tesi è stato dedicato alla risoluzione spaziale della ruota interna dell'EMEC con l'obiettivo di capire con che precisione il nostro calorimetro possa rivelare la posizione in cui le particelle lo colpiscono.

I risultati riguardanti la risoluzione in ϕ saranno inoltre usati dal gruppo ATLAS di Cracovia per uno studio sulla luminosità usando una coppia elettrone-positrone prodotta ad un angolo $\phi = 180$ nell'end cap: per questo motivo è necessaria una buona conoscenza della risoluzione spaziale.

Durante il TB del 2004 sono state utilizzate 6 *Beam Profile Chambers* (BPC) lungo il fascio di particelle per avere, evento per evento, la posizione della particella nel piano *XY*.

B.7.1 Risoluzione in ϕ

Sono state utilizzate run in cui il fascio colpisce il modulo del rivelatore nel suo asse di simmetria *Y* per poter avere la coordinata ϕ e la coordinata *X* delle BPC nella stessa direzione. Per ottenere la risoluzione in ϕ abbiamo inserito in un istogramma bidimensionale la posizione *X* delle BPC in funzione del valore ϕ del baricentro del cluster di 9 celle per vedere il loro grado di correlazione. Quindi si è proceduto al fitting ed in seguito si è costruito un istogramma unidimensionale con la differenza tra il valore di ϕ dato dal fit e quello calcolato (Figura 6.3).

Ciò che si ottiene è la risoluzione *globale*, non quella intrinseca del calorimetro. Infatti, come mostrato in Formula 6.1 il nostro risultato è la somma di tre termini

- Risoluzione intrinseca del calorimetro

- Contributo dovuto a effetti di *multiple scattering*: le particelle del fascio interagiscono con le particelle dell'aria che si trova tra le BPC e il criostato.
- Risoluzione intrinseca delle BPC.

Il nostro obiettivo è quello di estrarre la risoluzione intrinseca del rivelatore: bisogna dunque misurare o calcolare gli altri contributi.

La prima analisi riguarda il comportamento della risoluzione globale in ϕ al variare della coordinata η , usando run di elettroni a 120 GeV. Si notano immediatamente (Figura 6.4) le seguenti caratteristiche:

- Per tutte le BPC la $\sigma_{globale}$ aumenta con η in maniera pressoché lineare, con l'eccezione della cella $2.5 < \eta < 2.6$. Quest'ultimo fatto può essere spiegato ricordando che per un fascio incidente in questa cella non è possibile creare un cluster di 9 celle, con conseguente perdita di energia e peggioramento della risoluzione.
- La $\sigma_{globale}$ è minore per la BPC più vicina al calorimetro, a causa di minori effetti di multiple scattering. Con lo stesso ragionamento si può spiegare il fatto che la $\sigma_{globale}$ sia identica per ogni coppia di BPC: in Tabella 6.1 osserviamo come tra le BPC di ciascuna coppia ci siano pochi centimetri.

In seguito si è analizzato l'andamento della risoluzione in ϕ in funzione dell'energia, a η fissato, utilizzando le run in Tabella 6.2. Il metodo usato per calcolare la $\sigma_{globale}$ è lo stesso di quello usato precedentemente, ma i valori ottenuti sono stati fittati usando la funzione 6.2: quando usiamo l'energia nella determinazione della posizione, ci si attende che la risoluzione spaziale vari come quella in energia (Figure 6.5 e 6.6). Tuttavia si osserva che, anche per la BPC più vicina al rivelatore, il fit ottenuto non è perfetto, avendo un termine costante negativo. La situazione migliora decisamente se fittiamo il grafico con una funzione del tipo $1/E$ (Figure 6.7 e 6.8).

B.7.2 Risoluzione intrinseca delle BPC e contributi di Multiple Scattering.

Per calcolare la risoluzione intrinseca delle BPC abbiamo sfruttato il fatto che esse sono raggruppate in coppie (vedi Tabella 6.1) e che, su tali distanze, gli effetti di multiple scattering sono trascurabili. Inoltre, come si evince dalle loro caratteristiche tecniche riportate in [21], le stesse BPC non contribuiscono significativamente al multiple scattering.

La risoluzione intrinseca delle BPC è totalmente trascurabile nel caso di fasci di elettroni a bassa energia mentre il suo contributo nella somma in quadratura 6.1 per alte energie (120 GeV) raggiunge il 4%.

Per vedere come gli effetti di multiple scattering influenzino effettivamente la misura della risoluzione, si è considerato come la correlazione, e di conseguenza la risoluzione, tra la BPC più vicina al rivelatore e quella più lontana cambi al variare dell'energia del fascio incidente: in Figura 6.11 si può osservare che, a distanza fissata, la risoluzione ha l'andamento $1/E$ tipico del multiple scattering.

Tuttavia vi è un altro effetto, non preso in considerazione nella Formula 6.1, che tende a inficiare la risoluzione; infatti, se il multiple scattering fosse l'unica causa della degradazione della risoluzione, avremmo dovuto ottenere $\sigma_{BPC0,BPC5} = \sigma_{BPC0,BPC3} \oplus \sigma_{BPC3,BPC5}$. Invece sottraendo i contributi di multiple scattering alla $\sigma_{globale}$ non si ottiene la σ della risoluzione intrinseca delle BPC ma un termine aggiuntivo che cresce linearmente con la distanza e che può essere interpretato come un termine di divergenza del fascio (Figura 6.12). In ogni caso, usando la BPC5 (che dista solo 2.2 metri dal calorimetro) in tutte le analisi, si può considerare questo termine trascurabile.

La risoluzione intrinseca nella coordinata ϕ della ruota interna dell'EMEC risulta quindi essere il termine dominante della $\sigma_{globale}$ ed ha un valore dell'ordine di 1 *mrad*.

B.7.3 Risoluzione in η

La granularità finita del rivelatore dà origine a uno spostamento sistematico della misura del centro dello sciame elettromagnetico poiché i valori di η e ϕ di ogni singola cella sono quelli del suo centro. Dal momento che abbiamo lavorato sempre con un cluster di 9 celle, gli effetti della granularità finita sono attenuati (Figure 6.13 e 6.14).

In linea di principio si sarebbe dovuto ottenere lo stesso effetto anche in precedenza, nello studio della risoluzione in ϕ , ma la geometria a fisarmonica dell'EMEC permette una migliore condivisione dell'energia tra cellule confinanti in ϕ , rendendo trascurabile tale effetto.

La risoluzione in η che otteniamo è dell'ordine di 1 *m η* , anche se l'andamento al variare della pseudorapidità è meno evidente rispetto al caso ϕ .

Bibliography

- [1] F. Mandl, G. Shaw: *Introduction to quantum field theory*, John Wiley ed.
- [2] L. Wolfenstein: *Phys. Rev. Lett.* 51, (1983), 1945.
- [3] M. Peskin, D. Schroeder: *Introduction to Quantum Field Theory*. Addison Wesley Book.
- [4] M. Drees, *An Introduction to Supersymmetry*, hep-ph/9611409.
- [5] T. Wellman, *An Introduction to Supersymmetry in Quantum Mechanic Systems*, Senior Thesis, 2003.
- [6] The ATLAS collaboration: *Inner Detector Technical Design Report*, January 1997.
- [7] The ATLAS collaboration: *ATLAS calorimeter performance, Technical Design Report*, January 1997.
- [8] The ATLAS collaboration: *Muon spectrometer, Technical Design Report*, January 1997.
- [9] H. Bartko: *Performance of the Combined ATLAS Liquid Argon End-Cap Calorimeters in Beam Test at CERN SPS*, Diploma Thesis 2003.
- [10] L. di Ciaccio: *HV-Scan*, Presentation at the LAr week of February 2005, CERN, Geneve.
- [11] P. Barillon, F. Djama et al.: Uniformity scan in the Inner Wheel and the crack between the two wheels of the EMEC. ATL-LARG-2001-014.
- [12] ATLAS collaboration: *ATLAS Detector and Physics Performance. Technical Design Report*
- [13] L. Kurchaninov: *Results of August-2000 High Voltage Scan*, Presentation at the LARG. week of December 2000.

- [14] J. F. Laporte: *Diffusion Profondement Inélastique à HERA et Calibration Absolue de la Méasure en Énergie d'un Électron dans le Calorimetre à Argon Liquide de l'Expérience H1*
- [15] A. Savine: *Status of CBT-2 noise studies*, Presentation at the phone meeting of CBT-2 of January.
- [16] L. di Ciaccio, D. Fournier, F. Hubaut: *High Voltage corrections for electromagnetic calorimeters* ATL-LARG-2005-003.
- [17] C de la Taille, L. Serin: *Temperature dependence of the ATLAS electromagnetic signal. Preliminary drift time measurement.* ATL-LARG-95-029.
- [18] P. Schwemling: *EMEC: η dependence of the response.* Presentation at the LAr week of September 2005.
- [19] W. Shaw: *Update on EMEC ramp studies:* Presentation at the LAr week of November 2005, CERN, Geneve.
- [20] C. Serfon: *Response uniformity of the ATLAS electromagnetic end-cap calorimeter*, Ph.D. Thesis.
- [21] P. Gorbunov, P.Krieger: *The longitudinal positions of the Beam Chambers in the 2004 CBT-EC2.*
- [22] Particle Data Group: *The particle physics review.*
- [23] R.Sacco: *Position Resolution of an ATLAS electromagnetic calorimeter module*, ATL-LARG-2003-008.
- [24] W.E. Cleland and E.G.Stern: *Signal Processing consideration for liquid argon calorimeter in high rate environment* NIM A,338,1984
- [25] D. Banfi: *Studio del segnale generato nel calorimetro elettromagnetico ad argon liquido dell'esperimento ATLAS*, Tesi di Laurea A.A 2001-2002.